Synthesis of near-infrared absorbing mercury chalcogenide quantum dots

Mirzai, Hassan

Awarding institution:
King's College London

KING'S COLLEGE LONDON
University of London

Synthesis of near-infrared absorbing mercury chalcogenide quantum dots

by

Hassan Mirzai

A thesis submitted in partial fulfilment for the degree of

Doctor of Philosophy

School of Physical Sciences and Engineering

Department of Physics

2020

Abstract

The popularity of quantum dots (QDs) in the field of fluorescence has given rise to new methods for generating a diverse selection of nanoscale electromagnetic radiation sources. These emissions range from ultraviolet, crossing the visible light spectrum towards IR and NIR.

In this project, various near-infrared mercury chalcogenide (HgTe and HgSe) nanocrystals have been synthesised and analysed, describing new experimental strategies for the formation of these QDs. The newly developed methods seek to improve the fluorescent efficiency and characteristics of the QDs as well as reducing toxicity and increasing their stability. The absorption and emission spectra combined with the transmission electron microscope (TEM) images and X-ray diffraction (XRD) data determine the structure of the nanoparticles and allow understanding of their nature. By using an integrating sphere technique, quantum yields (QY) can be measured as a means to determine the fluorescent efficiency of these QDs and devise methods of improving this feature. These areas of analysis are the fundamental factors that define the characteristics of these QDs.

Luminescent mercury selenide (HgSe) quantum dots have been synthesised at room temperature by a phosphine-free method using oleic acid as a capping agent. The modification of experimental conditions such as temperature resulted in particles of various sizes (15–100 nm) and morphologies not previously seen in HgSe, with emission tunable between 1000 nm and 1350 nm.

A similar technique was used to synthesis mercury telluride (HgTe) quantum dots without the use of trioctylphosphine or trioctylphosphine oxide as a means to encourage a phosphine-free methodology. Using liquid nitrogen, the sudden temperature reduction

during synthesis resulted in highly monodispersed nanoparticles with NIR absorption and emission properties.

Finally, mercury telluride HgTe nanoparticles were biosynthesised in *Allium Fistulosum* (common spring onion) through a mutual antagonistic reaction. Exposure of common *Allium Fistulosum* to mercury and tellurium salts under ambient conditions resulted in the expulsion of crystalline, non-passivated HgTe quantum dots that exhibited emissive characteristics in the near-infrared spectral region, a wavelength range that is important in telecommunications and solar energy conversion.

Table of Contents

List of Figures

Chapter 1

Chapter 2

Chapter 3

Chapter 4

List of Equation

$$\boldsymbol{E_e} = \frac{h^2\, n^2}{8\pi^2 m_e\, d^2}$$

(1. 1) 26

$$\boldsymbol{E_h} = \frac{h^2\, n'^2}{8\pi^2 m_h\, d^2}$$

(1. 2) 26

$$E = \frac{hc}{\lambda}$$

(1. 3) 28

$$\boldsymbol{E = E_g + E_{confinement} + E_{exciton}}$$

(1. 4) 33

$$\boldsymbol{E_{confinement}} = \frac{\hbar^2\pi^2}{2r^2}\left[\frac{1}{m_e} + \frac{1}{m_h}\right]$$

(1. 5) 33

$$\boldsymbol{E_{exciton}} = -R_y\left[\frac{1}{\varepsilon_r{}^2}\ \frac{\mu}{m_e}\right] = -R_y{}^*$$

(1. 6) 33

$$\frac{\mathbf{1}}{\boldsymbol{\mu}} = \left[\frac{1}{m_e} + \frac{1}{m_h}\right]$$

(1. 7) 34

$$\boldsymbol{E_g} = \boldsymbol{E} - \frac{\hbar^2\pi^2}{2\mu r^2} + R_y{}^*$$

(1. 8) 34

$$Te + 2NaBH_4 \rightarrow Na^+{}_2Te^{2-} + 2BH_3 + H_2$$

(3. 1) 95

$$Na_2Te + 2[P(R)_3(R')][P(R'')] \rightarrow 2Na[P(R'')] + Te[P(R)_3(R')]_2$$

$$R = C_6H_{13} \qquad R' = C_{14}H_{29} \qquad R'' = C_{16}H_{34}O_2$$

(3. 2) 95

$$Hg(O_2CCH_3)_2 + C_{18}H_{33}O(OH) \rightarrow Hg^{2+}[C_{18}H_{33}O_2]^{2-}{}_2 + [CH_3CO(OH)]_2$$

(3. 3) 96

$$Te[P(R)_3(R')]_2 + HgX_2 \rightarrow HgTe + 2X + 2[P(R)_3(R')]$$

$$R = C_6H_{13} \qquad R' = C_{14}H_{29} \qquad X = C_{18}H_{33}O_2$$

(3. 4) 96

$$\mathbf{n} = \frac{\text{number of photons emitted}}{\text{number of photons absorbed}}$$

(5. 1) 136

$$\mathbf{n} = \frac{k_r}{(k_{nr} + k_r)}$$

(5. 2) 136

$$\mathbf{Lb} = \mathbf{La}\,(\mathbf{1} - \mu)$$

(5. 3) 136

Acknowledgements

Firstly, I would like to thank my supervisor, Professor Mark Green for his unparallel support through my studies. His positivity, kindness and most importantly patience has motivated me to be able to complete my Ph.D. As a part-time student, it has been a long journey since the start of my studies, with a lot that has happened and changed during the years and many challenges taking place, however, Mark has always kept supporting me till the end. It has been a fantastic journey working under his supervision. Additionally, I would also like to acknowledge my second supervisor, Professor Anatoly Zayats. Even though we didn't have many face-to-face meetings, he has been there since the beginning and has provided his support whenever needed.

I would like to thank, Professor Richard Curry from the School of Electrical and Electronic Engineering at the University of Manchester. His assistance during the time he was working at the University of Surrey's Advanced Technology Institute helped me greatly with my optical analysis. Many thanks for your patience and time in the laser labs.

I would like to acknowledge Dr. Gema Vizcay-Barrena who started working at King's College London Centre for Ultrastructural Imaging in the same year I began my Ph.D. and unfortunately left the department this January to peruse other challenges. Throughout my studies, she helped me with TEM, STEM and EDX analysis and trained me on some of the equipment. In addition, I would like to acknowledge Professor Roland Fleck and Leanne Allison from the same department for their help.

I would like to acknowledge Bill Luckhurst from the Department of Physics for giving me access to the lab chemicals and liquid nitrogen. Many thanks to Professor Sarah Haigh from the University of Manchester, Material Science Centre, with HRTEM and STEM analysis. Many thanks to Dr Arunkumar Panneerselvam who during the time he was a postdoc in our team at KCL, helped me with XRD analysis and HRTEM images from

University of Leeds EPSRC Nanoscience and Nanotechnology Research Equipment Facility, who I also would like to acknowledge for their support**.**

A special thanks goes to Dr Shohei Taniguchi, who during the time of his Ph.D. studies at King's College London, significantly helped me in the lab and taught me everything I know in lab techniques. His help and advice have always stayed with me and if it wasn't for him, I would not have known how to handle lab equipment.

No acknowledgement would be complete without a deep respect to the team, a.k.a. "Green Group". Being a part-time student, I have seen many come and go from the team however I would like to send a special thanks to Simon, Zeina, Basma, Mary, Lydia, Evren, Patrick, Marianna and Laura. I wish you all the best in your futures.

Finally, my deepest thanks and love goes to Mum and Dad who have given me their unconditional love, support, time and money without asking for anything in return. They have been by my side since the beginning and never lost faith in me. Thank you for your incredible patience and understanding.

Dedicated to my dearest wife, Shaghayegh, for her love, patience, encouragement and support.

Abbreviations and Symbols

Arb	arbitrary
a.u	arbitrary unit
EM	electromagnetic
EQE	external quantum efficiency
II-VI	group 12-16
IR	infrared
NIR	near-infrared
NPs	nanoparticles
PL	photoluminescence
QDs	quantum dots
QD-LEDs	quantum dot light emitting diodes
QY	quantum yield
RT	room temperature

Chemicals

Cd	cadmium
Hg	mercury
HgSe	mercury selenide
HgTe	mercury telluride
IL	ionic liquid
OA	oleic acid
ODE	octadecene
Se	selenium
Te	tellurium
TOP	tri-n-octylphosphine
TOPO	tri-n-octylphosphine oxide

TOPSe	tri-n-octylphosphine selenide
TOPTe	tri-n-octylphosphine telluride

Techniques

ADF	annular dark-field
BF	bright-field
EDX	energy dispersive X-ray
EDXS	energy-dispersive X-ray spectroscopy
HAADF	high-angle annular dark-field
HRTEM	high resolution transmission electron microscopy
STEM	scanning transmission electron microscopy
TEM	transmission electron microscopy
XRD	X-ray powder diffraction spectroscopy

Integrated Sphere

n	quantum yield
μ	fraction of reflected light absorption
A	fraction of incident light absorption
L	unabsorbed light
P	emitted light from sample
K_r	radiative recombination energy
K_{nr}	non-radiative recombination energy

Symbols and constants

c	speed of light
eV	electron volts
h	Planck constant
ħ	reduced Planck constant

E	total energy
E_g	bandgap energy
E_e	electron energy
E_h	hole energy
λ	wavelength
λ_{exe}	excitation wavelength
μ	reduced mass of the electron/hole
m_e	effective mass of electron
m_h	effective mass of hole
R_y	Rydberg's energy
r	radius
ε_r	dielectric constant

Chapter 1:

Introduction

1.1 Thesis overview

This thesis aims to explore various procedures for synthesising mercury chalcogenide quantum dots with near-infrared (NIR) optical properties. The work carried out here introduce experimental techniques for improving the characteristics of these quantum dots (QDs) and to determine the variables that can directly result in these changes.

1.2 Materials at nanoscale

The word nano originated from the Greek word *nanos*, meaning "dwarf". This prefix is used in the metric system as 10^{-9} with a nanometre being equivalent to 10^{-9} or one billionth of a metre. Particles with at least one dimension between 1-100 nm are considered to be nanoparticles. [1]

The behaviour of nanoscale materials is very different to that of a bulk solid and individual molecules or atoms. A typical inorganic nanocrystal can be comprised of only a few hundred to a few thousand atoms. This material will therefore behave differently when compared to a single atom with unique properties that are not present in bulk solids. Properties such as boiling point, melting point, chemical stability, optical and electronic characteristics are all different in a nanoparticle when compared to its bulk counterpart, with various examples of improvements made by the modification and control of the size and shapes of the nanostructures. [1]

1.3 Semiconductor band theory

To understand the relationship between nanoparticles and QDs, the properties of semiconductors should first be understood. The unique characteristic of semiconductors towards conducting electric current is intermediate between that of an insulator and a conductor, with its conductivity increasing due to an increase in temperature. In addition,

semiconductors may also have lower resistance to the flow of current in one direction than the other, similar to a diode. The conductivity of a material is dependant on its internal flow of electrons. This can be best understood by band theory, where the difference between conductors, semiconductors and insulators is determined by the separation between the valance band and conduction band (Figure 1.1). [2]

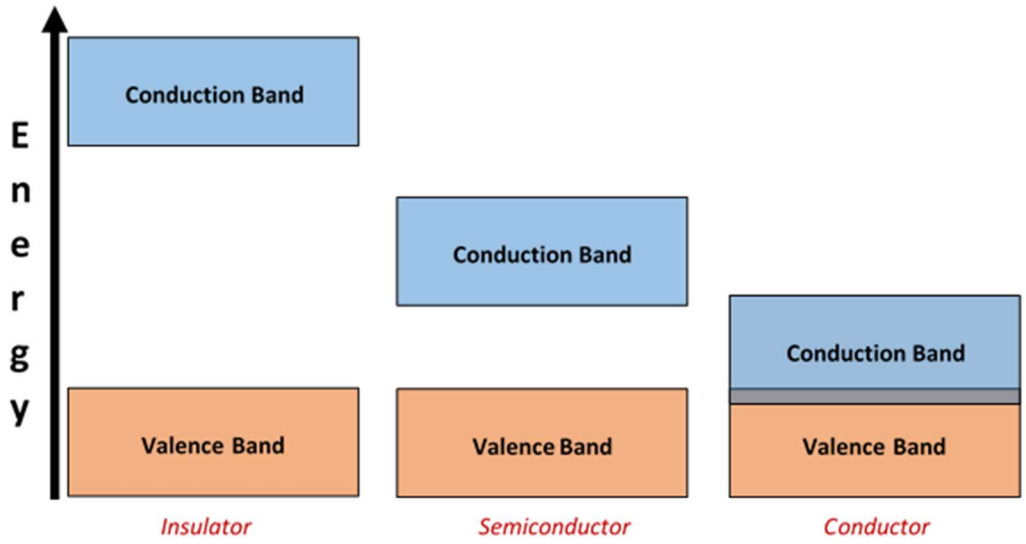

Figure 1. 1 - A schematic representation of the separation difference in the valance and conduction energy bands between conductors, semiconductors and insulator.

In semiconductors, there is a small separation gap between the valance and conduction bands when compared to the large insulator separation. No electrons can reside in the energy gap. The large energy gap within an insulator prevents any electrons from entering the conduction band via the valance band. The larger the gap between these bands within a material, would determine its electrical insulating strength. Conductors consist of a valance band that overlaps the conduction band, allowing electrons to travel freely between them and resulting in a consistent flow of electric current. At low temperatures, all the electrons in a semiconductor are located in a valance band, otherwise known as the

electron reservoir. Due to the high electron density in the valance band, the electrons are immobile preventing the flow of electric current. At higher temperatures, electrons in the valance band would acquire enough energy to reach the nearly empty conduction band, flowing freely due to the lower electron density. In turn, this process will cause an electron hole to be formed in the valance band due to the absence of an electron which flows as current similar to a physically charged particle. The energy of an electron-hole pair is quantified in the form of a natural quasiparticle known as an exciton. The separation distance between the electron and the hole in an exciton is called the exciton Bohr radius, which is characterised by the material and has large implications for the properties of QDs.[2] As the electron in the conduction band loses energy it will eventually fall back to the valance band, reoccupying the energy state of an electron hole. This process of electrons moving from the valance band to the conduction band and relaxing back to the ground state is known as the carrier generation and recombination.[2]

1.3.1 Energy levels and bandgap

The electronic structure of a material is defined by a solution of Schrödinger equations with boundary conditions related to the physical situation. [3] Figure 1.2 shows the electronic structure of a semiconductor in relation to the electron bands. The solutions of Schrödinger equations state that electrons in a semiconductor can only have certain allowable energies which are represented by energy levels within the bands. [3] Electrons cannot have energies between these levels; hence no energy levels can exist in this region. This energy gap region with no electron states is called the bandgap (E_g) and is an essential concept for explaining the physical factor determining the electrical conductivity of a solid and is the fundamental feature behind the function of a semiconductor device. [2] A simple example would be in solar cells that absorb light at wavelengths determined by the bandgap

of the material used. In this case, the bandgap is equivalent to the energy needed to free an electron from orbit around the nucleus within the valance band towards the conduction band. This will create a mobile charge carrier that can move freely within the solid material allowing electrical current to pass through.

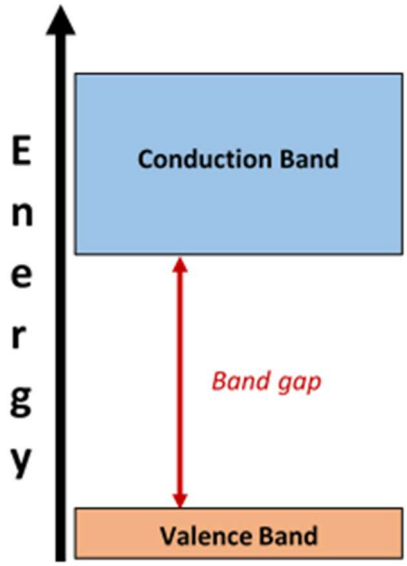

Figure 1. 2 - An illustration of the energy bands within a bulk semiconductor separated by an energy bandgap.

1.4 Quantum dots and their size dependant confinement effects

As previously mentioned, the exciton Bohr radius is the distance between the electron and electron hole created after an electron excitation from the valance band. [2] In a bulk semiconductor, the size of the crystal is much larger than the exciton Bohr radius, resulting in the exciton freely moving within the crystal structure. Quantum dots are semiconductor nanoparticles with characteristics closely related to the size of each individual crystal. These nano-sized crystal structures can have dimensions smaller than the Bohr exciton radius, which in turn results in a wider effective bandgap and the development

of isolated energy levels. [2] The discrete energy levels within a quantum dot are due to the quantum confinement effect, which transpires when the size of the semiconductor is reduced to only a few nanometres and can occur in various dimensions of space. [1] Confinement of the exciton in one dimension creates a quantum well whereas confinement in two dimensions produces a quantum wire. Quantum dots are a direct result of quantum confinement in all three special dimensions, causing changes to the bandgap properties. [2]

In larger particles, the bandgap is not effected and remains at its original energy due to a continuous energy state. This is primarily due to the confining dimensions being larger than the wavelength of the electron wave function, which is in turn known as the exciton Bohr radius. However, as the confining dimensions decrease to a certain limit towards the nanoscale, the energy states become discrete. This means that the energy levels are separated in relation to the size of the particles. Equation 1.1 represents the energy associated with an electron within the conduction band E_e, where h is the planks constant, m_e is the effective mass of an electron and n is the quantum number for the conduction band states (n = 1, 2, 3, etc.). Similarly, Equation 1.2 describes the energy associated with the hole in the valance band E_h, where n' is the quantum number for the valance band states (n' = 1, 2, 3, etc.). [3]

$$\boldsymbol{E_e} = \frac{h^2\, n^2}{8\pi^2 m_e\, d^2} \qquad \textbf{(1. 1)}$$

$$\boldsymbol{E_h} = \frac{h^2\, n'^2}{8\pi^2 m_h\, d^2} \qquad \textbf{(1. 2)}$$

Since m_e is much smaller than the effective electron hole mass m_h the electron energy levels in the conduction band are separated more widely than the electron hole levels

within the valance band. In addition, the diameter (*d*) of the semiconductor significantly affects the energy levels. Hence if the size of the particle is very small, the change created within the energy levels of the lowest conduction band and the highest valance band results in a size-dependant tunable bandgap.

Simply explained, the addition or removal of an atom in a bulk semiconductor is insignificant when compared to the size of the bulk containing large numbers of atoms. Therefore, the change to the bandgap would be negligible with the bandgap considered to be fixed. However, a similar change to a QD would result in the bandgap becoming tunable. For this reason, the innovative electronic structure of QDs is often referred to as "artificial atoms/molecules" due to their close resemblance to that of an atomic or molecular entity.

1.5 Optical properties of semiconductor QDs

Some of the most common QDs used today are cadmium selenide (CdSe),[3] cadmium telluride (CdTe), [4] zinc selenide (ZnSe) and lead(II) sulfide (PbS), [5] however, there are constant innovations that provide many other variations of these particles with other elements. Silicon nanoparticles are a good example of a quantum dot made of just a single element. [6]

As previously stated, the bandgap of a semiconductor quantum dot is inversely proportional to its crystal size, with smaller crystals having much larger bandgaps. This feature provides QDs with their unique optical capabilities allowing absorptions and emissions of electromagnetic radiation as a direct result of electron excitement. [1]

1.5.1 Absorption of light using photon excitation

QDs absorb light at different wavelength depending on their size. Due to the discrete energy levels of QDs, the energy gap between the highest occupied electronic state and the

lowest unoccupied state (electron-electron hole) is widened. Consequently, the optical properties of the semiconductor nanoparticle become dependant on their size. This relates back to Equation 1.1 and 1.2 where the particle size can significantly affect the bandgap, i.e. the bandgap becoming higher as the particle becomes smaller. [2] The bandgap of a QD defines the minimum energy required to create an exciton, thus the energy needed to excite an electron from the valance band to the conduction band. The relationship between energy and wavelength is given by Equation 1.3, where h is Planck constant, c is the speed of light and λ is the wavelength of light. This shows that to satisfy a high bandgap energy, shorter wavelength of light will be absorbed by the quantum dot.

$$E = \frac{hc}{\lambda} \tag{1.3}$$

The absorption of bulk semiconductors is very uniform when compared to QDs. This is because the bandgap is fixed and the energy states are continuous. [2] In the case of quantum dots, as the bandgap can be changed with the size of the crystal, the absorption wavelength becomes tunable. Figure 1.3 shows the difference in absorption curves between a bulk semiconductor and a quantum dot. [4] Samples 1 - 4 peaks correspond to the creation of the exciton, which is the minimum energy needed to excite an electron from the highest value state to the lowest conduction state. This is known as the absorption onset and the quantum dot will not absorb any wavelength of energy longer than this.

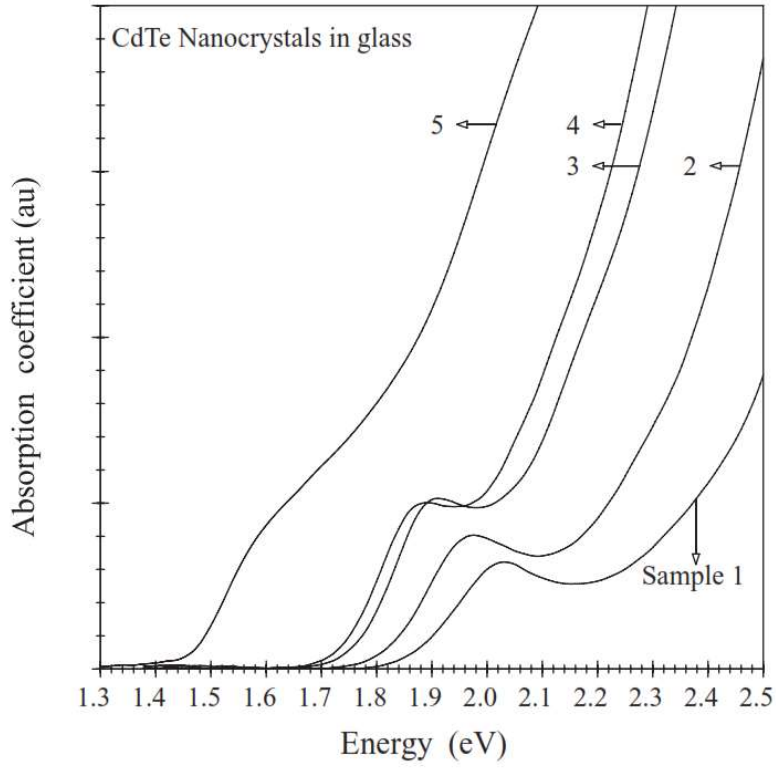

Figure 1. 3 – Room temperature optical absorption spectra for CdTe quantum dots. Samples 1 to 5 represent the increase in nanocrystal size with Sample 5 closely resembling to a bulk semiconductor. [4]

When measuring the absorption of QD nanoparticles, the position of the absorption peak within a UV-visible spectrum is determined by the particle size. For this reason, by observing various absorption readings, it is possible to estimate the size and concentration of the QDs. Different size QDs can be used for different applications, thus the monodispersity within a sample is very important. The absorbance of the QDs can provide an idea of how monodispersed a sample is. As the size of the quantum dot can change its absorbance, the monodispersity of a sample would depend on the peak width and sharpness of an absorption curve, Figure 1.4. A sharper peak would indicate a higher monodispersed sample. In the case of solar cells, it is important to have a high monodispersity as a means to provide optimal abortion of photons from the sun or light source.

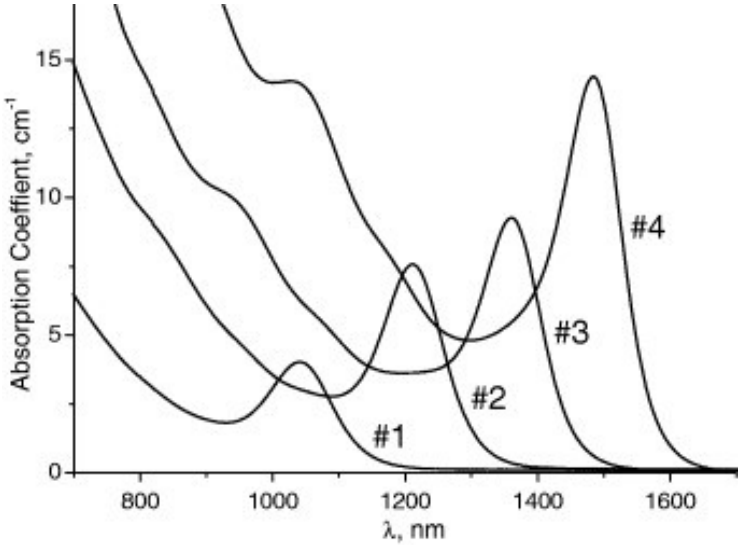

Figure 1. 4 – The absorption spectra of different size PbS QDs. The size distribution increases from #1 to #4 with increased average radii. [5]

1.5.2 Unique photoluminescence features of QDs

The term photoluminescence refers to the emission of photons from any material due to the loss of energy from the excited state to ground state. [2] The two main types of luminescence are fluorescence and phosphorescence. In a fluorescence process, the decay is instantaneous, with an emission rate of around 10^8 s^{-1} and a lifetime of around $10^{-9} – 10^{-7}$ s. This occurs when the excited electron in the conduction band has an opposite spin compared to the ground state electrons within the valance band. This is an allowed transition based on quantum mechanics and results in the rapid emission of a photon. Alternatively, phosphorescence is the emission of light in which the excited state electron has the same spin orientation as the ground state electron. This is a forbidden transition, which in turn results in slow emission rates, typically in the range of $10^3 – 10$ s^{-1}. Therefore, the lifetime of phosphorescence is much longer, with observable luminescence taking seconds to several minutes before the excited phosphors return to ground state. Phosphorescence is still seen even after the excitation light has been removed. The phenomenon of photon emission associated with the transition of electrons from the excited state to their ground state is

known as fluorescence. This unique feature in semiconductor QDs occurs as a direct result of a photon being absorbed with energy equal or greater than the quantum dot bandgap, thus creating an exciton in the process. This exciton eventually drops back into their outer orbit around the atom, in the valence band, losing energy in the process. This energy loss is achieved by a combination of non-radiative decay (loss of energy via heat and vibration) and radiative decay (loss of energy through photon emission). The excited electron moves quickly through the conduction energy levels by means of small non-radiative decays. The non-radiative decay only occurs between close energy levels, as the loss of energy through vibration and heat across larger energy level gaps, i.e. the bandgap can result in the breaking of the crystal bonds. For this reason, the emission of light occurs via a radiative decay across the bandgap, as a final relaxation to ground state. [2] Figure 1.5 shows an illustrated diagram of the path the electron takes from being excited using a high energy light source to relaxation and the emission of a photon.

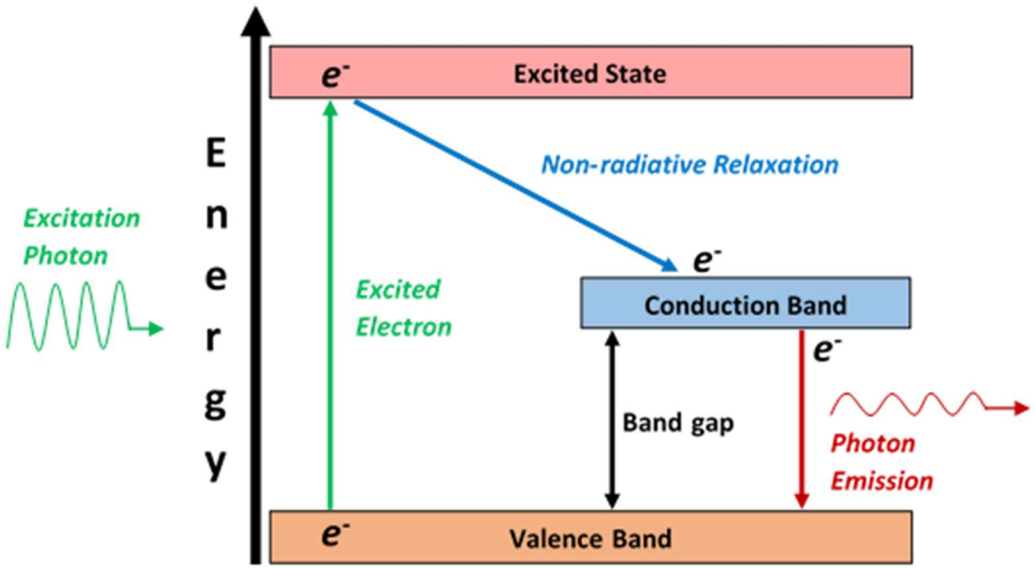

Figure 1. 5 - The emission of a photon due to the carrier generation and recombination process within a QD.

Since some of the energy is lost through the non-radiative decay, the energy of the emitted photon through the radiative decay is significantly lower than that of the absorbed energy, hence the wavelength of the emitted photon is longer than the absorbed light wavelength. This energy difference is called the Stokes shift and can be seen in most absorption-emission spectra. Figure 1.6 shows the difference in absorption and emission peaks for a typical CdSe/ZnS quantum dot. [6] The emission intensity versus the wavelength is represented by a Gaussian bell-shaped curve with the maximum emission wavelength being independent of the excitation wavelength as long as the excitation wavelength is shorter than the absorption onset.

The colour of the emitted light is directly related to the difference in energy between the conductive and valence bands (the bandgap). Hence smaller nanoparticles with a larger bandgap, resulting in a blue-shifted fluorescence. For this reason, the size manipulation of QD is vital for fluorescent tuning in which the synthesised QD can be designed to provide the required photoluminescence for specific applications.

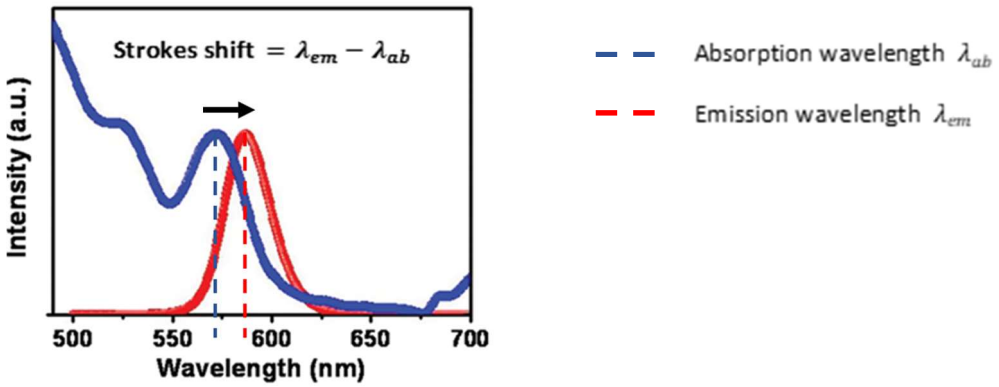

Figure 1. 6 – The absorption (blue) and emission (red) curves for a CdSe/ZnS quantum dot, showing the Strokes shift. [6]

1.5.3 Obtaining the bandgap of a QD

The total energy of the emitted photon ($\boldsymbol{E}$) in a recombination process of a QD can be represented by the sum of the bandgap energy ($\boldsymbol{E_g}$), the confinement energies and the bound exciton energy shown in Equation 1.4.

$$\boldsymbol{E = E_g + E_{confinement} + E_{exciton}} \quad \textbf{(1. 4)}$$

The confinement energy can be modelled as a simple particle in a one-dimensional box with the total confinement energy (Equation 1.5) obtained from the energy levels of both the excited electron and the electron hole represented as the solutions to the equation at the ground state (n = 1), where $\hbar$ is the reduced Planck constant, m_e and m_h are the effective masses of the electron and the hole and r is the particle radius. [2]

$$\boldsymbol{E_{confinement}} = \frac{\hbar^2\pi^2}{2r^2}\left[\frac{1}{m_e} + \frac{1}{m_h}\right] \quad \textbf{(1. 5)}$$

The exciton energy shown in Equation 1.6 can be modelled by the Coulombic interaction between the negatively charged electron and the positively charged electron hole. The negative energy within the attraction is proportional to Rydberg's energy (R_y) (13.6 eV) and inversely proportional to the square of the size-dependant dielectric constant (ε_r).

$$\boldsymbol{E_{exciton}} = -R_y\left[\frac{1}{{\varepsilon_r}^2}\ \frac{\mu}{m_e}\right] = \ -{R_y}^* \quad \textbf{(1. 6)}$$

μ is the reduced mass of the electron/hole represented by Equation 1.7. [2]

$$\frac{\mathbf{1}}{\boldsymbol{\mu}} = \left[\frac{1}{m_e} + \frac{1}{m_h}\right] \quad \textbf{(1. 7)}$$

Hence, as shown in Equation 1.8, by using these models and measuring the energy of the photon emission ($\boldsymbol{E}$), the QD bandgap can be obtained. [3] Additionally, using Equation 1.3 the wavelength of the emitted photon can be calculated.

$$\boldsymbol{E_g} = \boldsymbol{E} - \frac{\hbar^2\pi^2}{2\mu r^2} + R_y{}^* \quad \textbf{(1. 8)}$$

1.5.4 Factors affecting the optical properties of QDs

As mentioned earlier, the diameter of a quantum dot significantly effects its fluorescence properties. The emission of smaller QDs will be blue-shifted with larger ones emitting closer towards the red side of the electromagnetic spectrum (Figure 1.7). For this reason, the size and shape of QDs distinguish the energy of the emitted photon. [1] [2]

Monodispersed samples typically have better defined optical properties, as the majority of the QDs within the sample absorb light at similar wavelengths. These samples will have improved emissions, with photoluminescence that can be observed via their narrow emission peaks. Lower monodispersed samples would typically have wider absorption peaks which can cause lower emissions due to photon reabsorption effects. This is known to cause fluorescence quenching and is generally due to a fraction of emitted light being reabsorbed back into the sample creating an absorption-emission loop that reduces the number of emitted photons detected. Unwanted photon absorption/recombination is most common in QDs that have exciton peaks very close to their emission peaks. Consequently, if there are large variations in the quantum dot sizes within a test sample, the

emission peaks could be significantly affected. This is typically due to the superposition of emission peaks within the sample. [3]

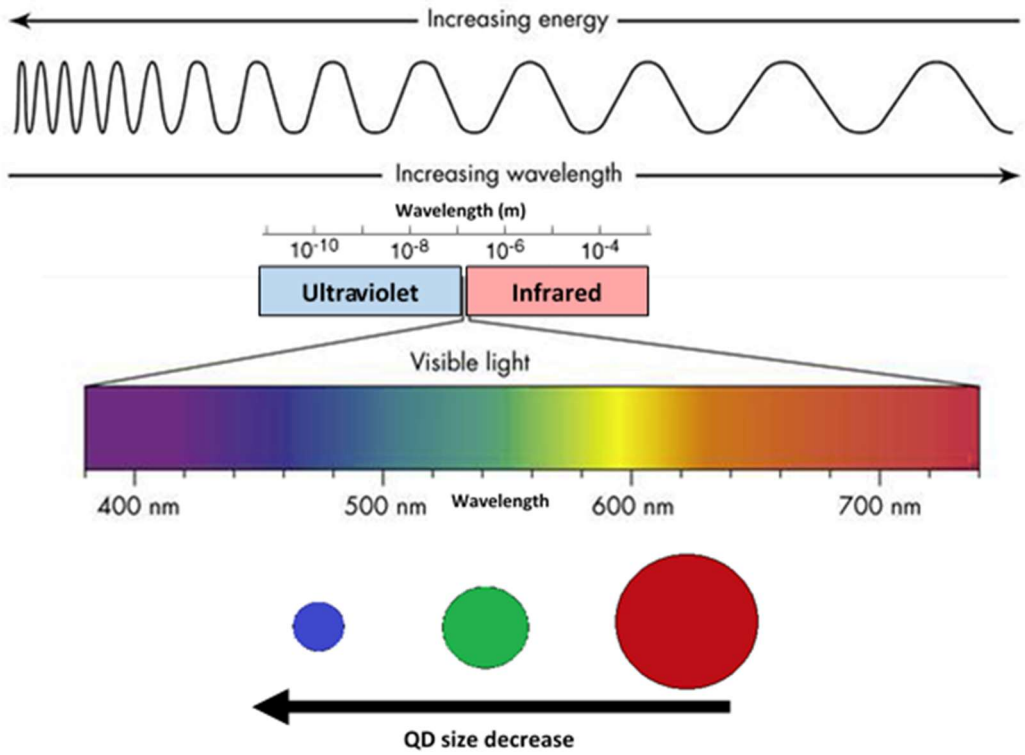

Figure 1. 7 – A diagram showing the blue shift of QDs as their size is decreased. The wavelength indicates the change in exciton energy.

Other key factors that influence the optical properties of QDs are surface defects, the presence of ligands and solvent polarities. Surface defects and imperfections of the quantum dot lattice structure can occur in the form of unsatisfied valencies. This provides a reduction in charge carries within the quantum dot, resulting in unwanted recombination. The presence of surface ligands can reduce the chances of unwanted surface recombination and minimise reabsorption effects. The polarity of the solvent that the QDs are prepared in is very important for the optical properties of the sample.

1.6 Applications involving the use of fluorescent QDs

The interest in nano-composites to researchers is due to various reasons. One of the main drivers for such research is the development of next-generation electronics and photonic devices. Particles of nanoscale materials exhibit unique quantum effects, short interface migration distances for photoinduced hole and electrons in photochemical and photocatalytic systems, and increased sensitivity in thin-film sensors. [7]

The popularity of semiconductor quantum dots (QDs) and their association with next-generation optoelectronic devices and biomedical applications has grown rapidly over the last years. Current research focuses on various synthetic routes as a means to modify QD characteristics to satisfy specific optical and magnetic requirements for applications such as biological imaging, [8] telecommunications, [9] photodetection [10] and solar energy. [11] Quantum dots have provided a new source of electromagnetic radiation. The wavelengths range from near-ultraviolet (NUV), [7] through the visible and even near-infrared (NIR) regions. [9] [12] NIR emission has been used widely in the fields of telecommunication [9] and imaging.[8] In the field of telecommunication, semiconductor nanocrystals producing emission within the IR region have the potential to expand the optical-fibre bandwidth, creating high capacity ultra-broadband optical amplification. [9] Due to its long wavelength, IR emission also has the capability of penetrating through human tissue, hence allowing for bio-imaging. [8] Other applications such as high-efficiency QD-LEDs and their uses in QD displays have also been gaining significant interest in current research. [13]

1.6.1 Biological and healthcare use

The small size of NPs means the most of the atoms are on the surface, hence the surface to volume ratio is very large. In addition, specifically tuned QDs have the capability to respond to various light energies, which in turn can provide highly effective PL properties,

thus they can be used for application such as biomarkers. [14] Due to their large surface area, in the past decade QDs have been tagged to a variety of drugs in order for their paths to be traced. [15]

In many diagnostic processes, the detection of several protein markers is required. Recently optical multiplexing techniques have been used to detect protein biomarkers via the fluorescence signals from different sized QDs. Multiplexing diagnostics allow the simultaneous measurement of multiple clinical parameters from a single volume source. This reduces the time and cost required to individually record each data point and allows quick detection of various infectious diseases. [15] Multiplexing has also been used to target and label DNA molecules using different QDs embedded into polymetric microbeads. [16]

Purposely shaped nanoparticles such as hollow shells can be used as drug delivery agents, thus when capped with an organic coating, these NPs can target the correct cells in order to deliver the required drug.[17] Furthermore, the long wavelength of near-infrared (NIR) emitting QDs (700-900 nm) has been used as an effective method for high-resolution and high sensitivity biological imaging. This is due to their increased penetration abilities using excitation and emission lights through biological tissue with no risk of radiation damage and minimized biological autofluorescence background.[14] These QDs are very successful when used as bio-probes and can be capped with amino groups of proteins to target specific cells. [14]

1.6.2 Photodetectors and solar-cells

To achieve the highest possible efficiency from a solar-cell, the maximum energy from the sun's broad spectrum should be harnessed. The sun's light can be split into different wavelengths in which half of the energy lies in the visible band and the other half in the infrared range. For this reason, single light absorbing semiconductor solar-cells consist of a

bandgap that lies in the near-infrared (NIR) range. [18] The sun's visible and infrared (IR) radiation can be more efficiently harnessed using a number of various light absorbing semiconductors employed in series. [18]

In a bulk semiconductor, due to the fixed bandgap of the material, the absorption energy is limited to a fixed wavelength, resulting in significant amounts of unutilised energy. QDs are used in the field of solar-cells as they can be tuned to absorb energy over a large range of the solar spectrum. This results in the formation of more photo-electrons and hence increases the flow of charge within the semiconductor, allowing more efficient use of the solar energy. [19]

1.6.3 QD-LEDs and displays

The fluorescence tuning of QDs with regards to their dimensions allows them to provide near-unity emission quantum yields and narrow emission bands. This feature results in excellent colour purity that in turn has motivated the development of quantum dot light emitting diodes (QD-LEDs). Semiconductor QDs can function very much like regular LEDs, however with much higher light efficiencies and reduced wasteful charge carriers that could potentially disrupt the production of light. The more common filament incandescent bulbs are known to have very low light efficiencies with the majority of energy dispersed as heat. These bulbs are rapidly being changed to less wasteful fluorescent lights or with more efficient LEDs that are gaining significant popularity to users.

QD-LEDs are becoming the next step in the development of light emitters within electroluminescent devices. In the last decade, advanced research in QD-LEDs has led to dramatic improvements in their performance, resulting in their commercial requirements reaching close to satisfactory levels. [13] Despite the significant progress made in QD-LED technology, one of the challenges being faced today is the low external quantum efficiencies

(EQE) of these light emitters.[20] The EQE represents the efficiency in the last step of light production within a QD-LED, taking into consideration the probability of electron recombination. This can be quantified by the luminescent quantum yield (QY) which is proportional to the EQE. [20]

During recent years, work has been done to improve the charge transfer within QD-LEDs. One example is by using CdSe-CdS QDs coupled with zinc oxide (ZnO), resulting in an increased QY. These improvements in the electroluminescence have made QD-LEDs comparable to state-of-the-art organic light emitting diodes (OLEDs), currently being used in the most advanced large screen displays and mobile devices. [21] In addition, recent publications have suggested the use of ZnSe capped with ZnS as successful candidates for cadmium free QD-LED light emission.[22]

Technologies in the current conventional LCDs use high intensity blue LED backlights with a phosphor coating and white light for displaying image movements. The new QD-LEDs used in displays operate via a thin glass tube containing QDs that can absorb the blue LED backlight and re-emit it as pure red and green. This results in the progression of intense colours when compared with the phosphor coated LED displays. [23]

1.7 Group 12-16 (II-VI) semiconductor QDs

Semiconductors are generally classified on the basis of their periodic table grouping. In the case of group 12-16 semiconductors (II-VI), these consist of materials that have cations from group 12 and anions from group 16 in the periodic table (Figure 1.8). Cadmium selenide (CdSe), cadmium telluride (CdTe), zinc sulfide (ZnS), mercury telluride (HgTe) and mercury selenide (HgSe) are just a few examples of II-VI nanoparticles.

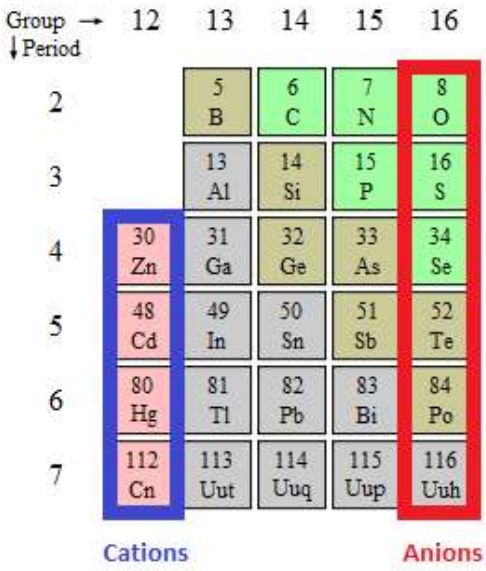

Figure 1. 8 – The periodic table showing the group 12-16 (II-VI) elements.

Cadmium selenide (CdSe) is one of the most popular II-VI semiconductor QDs. This is primarily due to their highly tunable bandgap (typically 712 nm or 1.74 eV), which can be engineered to absorb light throughout the visible range. This is vital when used in the development of solar cells, as the QDs are required to cover the majority of the energy from the solar spectrum. CdSe QDs have also been used in the development of highly efficient QD-LEDs. [20] [21] Though cadmium and selenium are known carcinogens, the harmful biological effects can be overcome by the capping of CdSe with a layer of zinc sulfide (ZnS), thus being used as biomarkers or drug delivery agents. [16]

Cadmium telluride (CdTe) is another commonly used QD with a bandgap of 1.44 eV (860 nm). These QDs are known for their NIR fluorescence capabilities and for this reason, the bandgap of these QDs are much smaller due to their larger size and longer absorption wavelengths. Hence CdTe can be used in conjunction with CdSe QDs to absorb a wider range of the solar spectrum.

1.7.1 Mercury chalcogenides

The preparation of highly crystalline, monodispersed II-VI QDs with protective layer capping has been considered a challenge throughout the years. However various projects have been focused on the development of these QDs in different forms of applications with promising results.

The relatively recent emergence of high quality quantum dots prepared by colloidal routes as a distinct technology can be traced back to a seminal paper in 1993, where metal alkyls were reacted with phosphine chalcogenides in a hot coordinating solvent, yielding passivated, monodispersed, quantum-confined cadmium chalcogenide semiconductor particles, the quality of which had not been seen previously. [24] As a result, thousands of papers now describe numerous advances in both synthesis and applications. The majority of other binary inorganic semiconducting systems (notably the IV–VIs and III–Vs) were prepared using similar chemistry, evolving from organometallic precursors to inorganic and silylated precursors, with surfactants, material composition, structure and reaction conditions becoming as equally important as precursor chemistry. Recent publications have contributed towards new innovations in the organometallic growth of nanoparticles with quantum confinement properties that provide tunable bandgaps. [25] [26] Whilst the majority of semiconductor materials (such as the II-VIs, IV-VIs and III-Vs) have been prepared on the nanoscale using organometallic routes, one of the families that has not emerged as quickly and remains relatively unexplored is the mercury chalcogenides. This is possibly due to the lack of obvious and safe precursors (despite the fact that many early routes to nano-dispersed semiconductors were based on mercury chalcogenides). The focus on mercury chalcogenides has been primarily due to their low reaction temperatures (which has been assigned to the positive redox potential of the mercury precursors) and ease of synthesis resulting in novel IR-emitting and absorbing materials. [12] In addition, mercury chalcogenide quantum dots are

known to have bandgaps and excitonic diameters that suggest widely tunable emission, notably in the near-infrared region (>800 nm). [9] [27] [28] The key material from this family is mercury telluride, HgTe, with reports of HgSe and HgS gradually appearing with improving synthesis. It should be noted that the entire mercury chalcogenide family remains a poorly defined group of materials even in the nonquantum confined regime. Bulk phase HgTe, HgSe and HgS have narrow or negative bandgaps that lend themselves to infrared applications, yet the exact values of these bandgaps remain unclear; HgTe reportedly has a room temperature bandgap between -0.32 eV [29] and -0.15 eV [30] and is often referred to as a zero bandgap material, whilst HgSe reportedly has a room temperature bandgap between 420 meV and -274 meV. [31] [32] HgS exists in two crystal phases; trigonal α-HgS and the metastable zinc-blende structure β-HgS with suggested room temperature bandgaps between -0.19 eV and 0.05 eV. [33] [34] In fact, HgTe is one of several key materials which potentially exhibits bandgap emission at the telecommunications wavelength of between 1.3 and 1.55 mm (Figure 1.9). Bulk mercury chalcogenides are also suggested to be topological insulators, with potential applications in spintronics. [35] [36]

The reasons for the slow emergence of mercury chalcogenide nanoparticles are unclear, although three key factors may play a role. The obvious limiting step is the availability of safe and suitable mercury precursors. Initial work on the organometallic synthesis of passivated quantum dots utilised simple metal alkyls such as Me_2Cd, which, whilst difficult to handle, were relatively safer when compared to the analogous mercury alkyls, which are known to be extremely dangerous. Therefore, the majority of the earliest work on the preparation of high quality, quantum-confined semiconductor particles by the high temperature, hot injection method concentrated on cadmium chalcogenides and to a lesser degree, group III-Vs (which relied on a previously developed solution route which remains definitive to this day). [37] [38] As alternative precursors to metal alkyls emerged, such

as metal oxides and carboxylates, other materials became accessible, and lead chalcogenides (with optical properties in the near-infrared region of the electromagnetic spectrum) became popular, with reports of mercury chalcogenides following. [39]

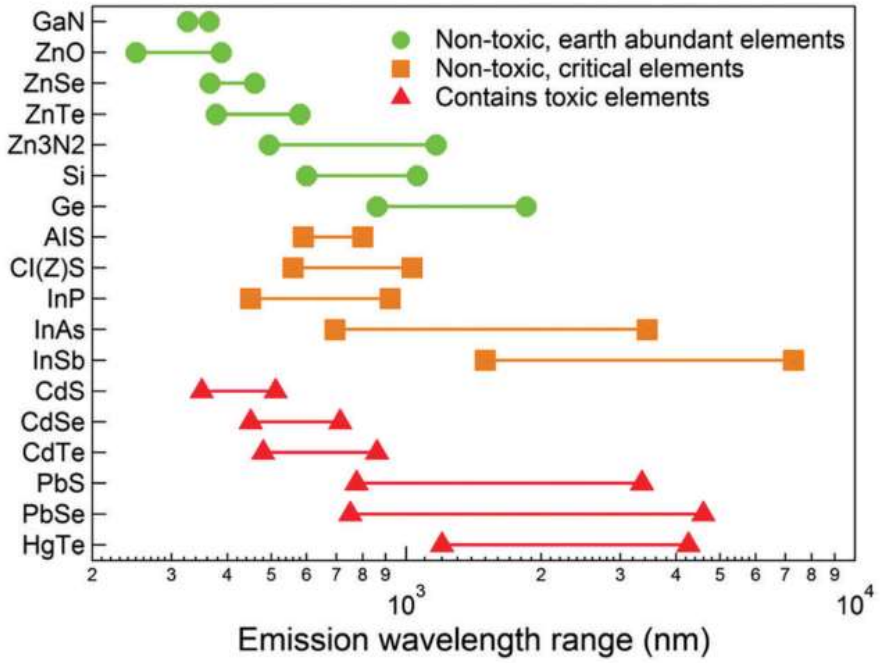

Figure 1. 9 – Emission wavelengths for selected bulk semiconductors. [40]

Secondly, the optics of these materials are predominately in the infrared spectral region, which many research groups will struggle to access. Thirdly, one of the initial and key applications of colloidal quantum dots was biological imaging, [41] where mercury compounds potentially present a toxicity problem, although as will be discussed later, this does not necessarily exclude mercury containing nanomaterials from biological applications.

A key feature of quantum materials prepared by organometallic chemistry is the vivid way in which the quantum confinement of charge carriers can be easily demonstrated by simple spectroscopy. It is therefore easy to overlook the evolution of the organometallic chemistry behind this innovation, and if one were to explore the earliest work on materials precursor chemistry by pioneers such as Steigerwald, who developed the use of phosphine chalcogenides (initially described as 'masked atoms') as solution-based alternatives to more volatile, hazardous species, [42] one would observe that many of the materials prepared were in-fact mercury chalcogenides. One of the earliest reports on the organometallic synthesis of II-VI materials described the thermolysis of $Hg(TeR)_2$ (R = organic groups) in refluxing toluene yielding HgTe at relatively low temperature, and the thermolysis of the related compound $Cd(TeC_6H_4CH_3)_2$ at 200 °C yielding CdTe. [43] This is also noteworthy as it is generally assumed that the use of single source precursors was a much later development, whilst it is clear that such organometallic compounds were, in fact, some of the very first to be explored as precursors for solid-state materials. In this seminal work, no optical data was presented as might be expected for a purely synthetic report, however, a further report where the use of bidentate phosphine complexes of the type $M(ER)_2$ (M = Zn, Cd, Hg; E = S, Se, Te; R = Ph, *n*-Bu) was described, highlighted that solution thermolysis in Lewis base solvents such as 4-ethylpyridine yielded nanoparticles and the initial absorption measurement of CdTe were reported.[44] A notable result was the fact the $Hg(TePh)_2$ formed nanoparticles on mild refluxing, yet continued to grow in the bulk phase. This was overcome by using $Hg(TeBu)_2$ which was converted to HgTe nanoparticles by simple photolysis under ambient conditions. This simple growth at low temperatures was to become a feature in future work and will be discussed later. It is also worth noting the more unusual methods were reported for the synthesis of nanostructured mercury chalcogenides, such as the growth of HgTe in single-walled nanotubes. [45] Whilst novel structures such as

the Hg_2Te_2 motif observed in such systems is impressive, this project will focus on colloidally prepared HgE (E = Te, Se) quantum dots and related materials.

The original method of preparing high quality HgTe quantum dots which finds its origin in traditional colloidal chemistry is the aqueous route, where simple metal salts are reacted in aqueous solution and their growth halted using stabilisers. The advent of the organometallic synthesis of quantum dots provided access to a wide range of materials that were previously unobtainable using aqueous-based techniques. As a result, new NIR-emitting quantum dots such as lead chalcogenides have emerged, and such materials are now considered well-established and efficient fluorophores. One of the first examples of the preparation of mercury-containing quantum dots, synthesised by the more traditional techniques was reported by Eychmüller *et al*. where CdS colloids were prepared in water using polyphosphate as a stabiliser, followed by capping of the particles with $Cd(OH)_2$ (termed activation), giving a green emitting material. [46] [47] Addition of an aqueous solution of $HgCl_2$ to the preformed CdS particles resulted in the absorption edge at *ca.* 500 nm gradually shifting towards the red end of the visible spectrum, with the gradual reduction in CdS emission at *ca.* 500 nm and the emergence of broad emission at *ca.* 625 nm which then shifted towards 770 nm with the increased addition of the mercury salt. The emergence of the red emission was assigned to the formation of the narrower bandgap HgS on the surface of the CdS colloid, forming what is usually referred to as an inverse core/shell structure of CdS/HgS, with the CdS particles acting as the sulfur source. This was then reversed by preparing HgS/CdS core/shell materials using essentially the same aqueous system, but in this case, reacting $HgCl_2$ with H_2S in the presence of a polyphosphate stabiliser in alkaline aqueous solution, followed by the addition of $Cd(ClO_4)_2$ and further addition of H_2S. The resulting core β-HgS particles were reportedly *ca.* 1.8 nm in diameter, increasing to 2.8 nm after treatment with the additional shell precursors. Interestingly, the small HgS particles had

a band edge onset at *ca.* 500 nm, with no evidence of emission from uncapped HgS or HgS/CdS with a thin shell, however, with the addition of increasing amounts of H_2S, emission at *ca.* 950 nm emerged but did not shift spectral position, consistent with a wider bandgap shell.

This was extended by depositing a further layer of CdS on the CdS/HgS, giving a double shell, or quantum dot quantum well (QDQW) structure, [48] with the narrow bandgap HgS layer (quantum well) sandwiched between two wider bandgap materials, giving a CdS/HgS/CdS structure. [49] This was achieved following similar synthetic protocols as described above for CdS/HgS, although after the addition of the mercury salt, H_2S was then added to react with the resulting released Cd^{2+} ions, followed by further addition of precursors for the final shell deposition. It was reported that for this preparation, the core of CdS alone did not emit, and neither did the structure after the addition of the first shell (CdS/HgS). It should be noted that at this point, the CdS core had presumably not been passivated with a $Cd(OH)_2$ shell. Only upon addition of the precursors for the final shell did emission at *ca.* 700 nm emerge, reaching a maximum intensity with a final passivation of $Cd(OH)_2$; the origin of the emission was assigned to the overlap of photogenerated charge carriers recombining in the HgS layer, and later in-depth calculations confirmed the presence of charge carrier wave functions in the HgS shell. [50]

An interesting observation was the fact that the CdS core particles were not simply acting as a sulfur source; as HgS has a significantly lower solubility product compared to CdS, and upon Hg^{2+} addition to the CdS particles, a surface substitution reaction occurred giving a monolayer of HgS, releasing cadmium ions into solution which were available for the deposition of the final shell upon reaction with further H_2S, which was again often just a single monolayer thick.

High-resolution electron microscopy studies confirmed that the particles indeed consisted of a HgS layer epitaxially embedded in a CdS crystallite and that the Hg ions substituted Cd ions in tetrahedral zinc-blende structured CdS particles, maintaining the original morphology. Addition of the final layer of CdS maintained the tetrahedral shape whilst increasing the particle size, although non-tetrahedral particles were also observed and assigned to the final CdS shell growing out of phase with the core particle due to stacking faults on the tetrahedral surface. [51]

The precursor addition could be tuned to give a HgS layer between 1 and 3 monolayers thick, whilst the final CdS shell could be tuned to between 1 and 5 monolayers (Figure 1.10). [52] Generally, the quantum dot quantum well particles exhibited optical band edges with distinct excitonic features and the associated band edge emission between *ca.* 500 nm and 900 nm, with the increasing onset to the red region of the spectrum occurring with increasing HgS shell thickness, and overall dimensions between *ca.* 5 and 8 nm. Emission quantum yields ranged from 10% for the untreated CdS, to as low as 3% for the far-red emitting materials; the quenching attributed to radiation-less transitions at either the HgS/CdS interface or within the HgS structure itself. Interestingly, the emitting state was suggested to be different from the absorbed state due to phonon coupling [47] [51] [53] [54] at the HgS/CdS interface. [55] The aqueous synthesis of HgS has also been achieved by numerous groups and includes notable studies such as the preparation of chiral nanocrystals.[56] [57]

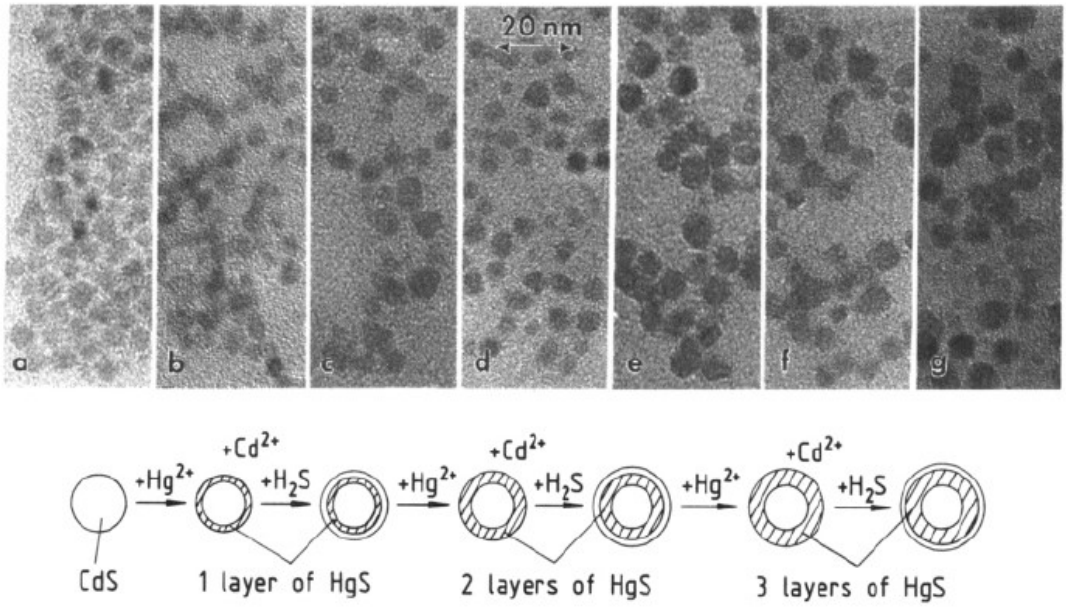

Figure 1. 10 – TEM images of CdS/HgS/CdS quantum dot quantum wells at different stages of growth by aqueous synthesis. Scale bar = 20 nm. [52]

1.7.2 Aqueous routes to mercury chalcogenides

The aqueous synthesis of mercury chalcogenides was followed by one of the most important developments in the field of mercury chalcogenide nanoparticles. In 1999, a key report by Rogach *et al*. described the synthesis of thiol-capped HgTe quantum dots, [58] based on the aqueous synthesis of CdTe quantum dots. [59] (It should be noted that the aqueous synthesis of thiol-capped CdTe quantum dots is a well-established field to rival quantum dots prepared by organometallic-type routes. [60] [61] [62]) In this case, an aqueous solution of $Hg(ClO_4)_2$ was complexed with thioglycerol ($HSCH_2CH(OH)CH_2OH$), followed by exposure to H_2Te gas in a stream of nitrogen. Unlike the synthesis of thiol-capped CdTe, no heating was required and was detrimental to the quality of the nanoparticles produced. The resulting particles, *ca.* 3 nm to 6 nm in diameter with a cubic crystalline core, could be isolated by addition of 2-propanol as a non-solvent, and redispersed back into water. The absorption spectra were reportedly featureless, with a tail

that extended into the near IR region combined with broad emission between *ca.* 800 nm and 1400 nm, and an impressive quantum yield of *ca.* 48%. Slow ageing over a matter of weeks resulted in a gradual red-shift and reduction in quantum yield, which appeared to be the main problem with this synthesis. The emission maxima also shifted from *ca.* 1150 to 1300 once dispersed in pyridine, and was found to be quite dynamic. By using D_2O rather than H_2O, the view of the emission profile was improved, [63] (a detailed study of the impact of using D_2O has been discussed elsewhere [64]) whilst it was also found that by using an excess of H_2Te or by the application of gentle heating, long emission wavelengths were accessible (*ca.* 1600 nm), although the colloidal stability was compromised. The limited near-infrared wavelengths accessible from the simple colloidal route was addressed elsewhere by gentle heating of thioglycolic acid and mercaptoethylamine-capped particles (prepared in a similar manner) which pushed the emission profiles out to the mid-infrared region (up to 4 mm) by increasing the particle size up to 12 nm in diameter, although the emission quantum yield dropped dramatically. [65] Mercaptoethylamine-capped HgTe was also found to be effectively phase transferred to an organic solution using the hydrophobic ligand dodecanethiol. Interestingly, the same report also described an electrochemical reduction of elemental tellurium in acidic media to generate H_2Te gas as a precursor. [66] Such particles could be dispersed in polymers such as poly(methylmethacrylate) and polystyrene, and then processed into devices such as photonic crystals. [67] The wide range of sizes allowed detailed studies of the electronic structures by spectroscopic ellipsometry, finding the semiconductor critical points. [68] Other interesting relevant studies include the observation of multiple exciton generation in thiol-capped HgTe, [69] which is of relevance to solar energy generation. Indeed, HgTe nanoparticles have been incorporated into photodetectors [70] [71] and nanocrystal-sensitised hybrid polymer solar cells, which used both thioglycerol-capped HgTe quantum dots, prepared as described above, and

organically-soluble dodecanethiol capped nanoparticles prepared in exactly the same way, with a secondary ligand exchange step. [72] An important feature of these nanoparticles is their processability, as the particles need to be easily manipulated into various matrices if their optical properties are to be realised in device architectures. In the simplest arrangement, 1-thiolglycerol-capped HgTe were dropcast onto a Si substrate, connected to electrodes for photocurrent measurements. [73] The optical properties of the QD solution and film were similar, suggesting the capping agent remained intact and maintained a discrete separation of the particles. These basic films showed different I–V characteristics in the dark and under illumination, suggesting the presence of a photocurrent. By examining the energy levels of the particle and the thiol, it was determined that the electrons were confined to the core of the particles, whilst the holes delocalised to the capping agent, thus acting as free charge carriers. A similar study was carried out in which thioglycerol passivated HgTe quantum dots were washed with methanol and acetone to remove the thiol capping agents, redispersed in water and drop cast onto a Si/SiO_2 substrate between two gold electrodes. [74] The excitonic features of the HgTe were observed to red-shift, as did the emission from *ca.* 1000 nm to *ca.* 1700 nm with a significant decrease in intensity, attributed to overlapping wave functions of the particles. One should also note that the sharpness in the excitonic feature is not easily comparable to CdSe quantum dots prepared by similar chemistry, as several factors affect such spectral features, such as oscillator strength, and particle packing.

In a more advanced architecture, HgTe nanoparticles were deposited on latex spheres which were then used as subwavelength near-infrared emitters, [75] using layer-by-layer film deposition techniques. [76] The spheres were easily photobleached in air, however, spheres embedded in a polyvinyl alcohol matrix were protected from oxidation effects. Similar chemistry was used to deposit HgTe and HgCdTe quantum dots on micro-sized silica spheres, which were utilised in a whispering gallery mode laser. [77] A popular

application for HgTe particles is their use in light-emitting devices, and near-infrared electroluminescence has been observed from a simple device in which the quantum dots were embedded in a methyl-substituted poly(para-phenylene) polymer.[27] [78] To allow processing, the hydrophilic surface ligand (thioglycerol) on the HgTe particles was exchanged for a long chain thiol (dodecanethiol) which allowed the particles to be solubilised in non-polar hydrocarbon solvents with minimal effects on the optical properties. [79] The resulting devices displayed emissive properties consistent with the constituent quantum dots, with no spectral shift observed in the presence of the applied field. To enhance the emission of dodecanethiol-capped HgTe quantum dots dispersed in polymer films, a PMMA film containing the quantum dots was deposited on a silicon-on-insulator (SOI) 2-dimensional photonic crystal. [80] The coupling of the emission with leaky eigenmodes of the photonic crystal resulted in a 650-enhancement factor for oblique emission, and 80 for vertical emission at the telecommunications wavelength.

Electroluminescent devices incorporating HgTe quantum dots have also been reported without the need for ligand exchange. [81] In this case, the quantum dots were dissolved in DMF then drop deposited onto PEDOT:PPS-passivated ITO substrates, followed by annealing and the deposition of an aluminium cathode. In this case, the electroluminescence was red-shifted by *ca.* 70 nm from the initial colloidal quantum dot solution, and attributed to reabsorption of some of the luminescence in the nanoparticle layer, charging effects, the presence of electrical fields or selective emission due to energy transfer. In related work, HgTe quantum dots deposited on a glass substrate were used in the fabrication of a microcavity light-emitting device, with stability reported up to 75 °C [82] whilst thin-film transistors have been prepared which utilised sintered HgTe quantum dots. [83]

Applying the same aqueous synthetic chemistry towards HgSe yields similar materials, but with narrower emission, smaller Stokes shift and crucially a much-reduced emission quantum yield of 0.5% resulted. [9] Other unusual aqueous-based synthetic methods have been reported, where the biological detoxification process known as mutual antagonism was exploited. In this case, HgSe is a common by-product to the exposure of living systems to mercury. [84] [85] In a typical example, $HgSe_xS_{1-x}$ was prepared by mimicking the biological process, by reacting $HgCl_2$ with Na_2SeO_3 in the presence of glutathione in buffer solution, giving passivated nanoparticles. These particles were structurally analysed in some depth. An absorption spectrum was recorded and showed some evidence of a far-red absorbance tail although the main profile was towards the blue end of the spectrum. No report was made regarding the emissive properties. [86] Biosynthesis has not yet been widely adopted by the materials community and as such, the optical properties of biosynthesised nanomaterials remain poorly recorded. Much of the work centres on HgSe due to the naturally occurring *in vivo* reaction of mercury contaminants with selenoprotein P, which makes the cross disciplinary translation difficult due to the lack of available synthesis models *in vitro* and the poor optical properties of HgSe. Biosynthesis has been adapted *in vivo* by utilising plants that undergo mutual antagonism, and by adapting the synthesis to the more interesting HgTe. In such systems, plants such as the allium family have been utilised to make HgTe quantum dots, which have no capping agents yet emit weakly between 1000–1300 nm. [87]

In another simple example of an aqueous synthesis, selenium powder was dissolved in 5 M NaOH and sonicated whilst an equimolar amount of $Hg(CH_3CO_2)_2$/EDTA was added. Suspension of the resulting insoluble HgSe power in dihydrolipoic acid (DHLA) followed by heating, stirring, deprotonation, dilution in water and purification gave DHLA-capped HgSe. [88] The particles appeared approximately 20 nm in diameter by transmission

electron microscopy, with a hydrodynamic diameter of *ca.* 70 nm. Interestingly, the material exhibited an optical excitonic shoulder at *ca.* 400 nm, with sharp emission at 575 nm, significantly shifted from the near IR emitting materials described above. The observation of emission in the visible spectral region from HgSe nanoparticles is not, however, unique. In detailed work, Kuno *et al.* reported a series of synthetic pathways to HgS, HgSe and HgSeS alloys with optical properties in the visible spectral region. It was reported that the stability constant of the capping ligand was a crucial factor to consider when designing mercury chalcogenide systems; ligands with stability constants less than 10^{17}, such as amines and carboxylic acids resulted in quick precipitation after the reaction, whilst stronger binding ligands such as thiols, phosphines, phosphine oxides and polyamines resulted in the reductive elimination of mercury at the relevant reaction temperatures. Taking these details into account, a micellar route was devised where strongly binding thioglycerol was reacted with mercury acetate $Hg(O_2CCH_3)_2$ to produce a stock solution, which was then added to the surfactant AOT, followed by the room temperature reaction with $(SiMe)_2S$ yielding HgS quantum dots. The particles grew until they were capped with either Cd or Zn using the parent metal alkyls, then further capped with an organic ligand. The HgS quantum dots were between 1 and 5 nm in diameter with a cubic structure (β-HgS). [89] The particles exhibited band edge emission between *ca.* 600 and 700 nm, with quantum yields below 1% without the metal cap and up to *ca.* 6% with the metal shell (Figure 1.11). [90] This chemistry was extended to the preparation of HgSe and $HgSe_{1-x}S_x$ quantum dots, with Kuno *et al.* reporting the use of a reverse micelle approach involving an amphiphilic surfactant, producing stable emissive HgSe clusters with a band edge at 595 nm (2.08 eV) and emission profiles close to 630 nm (1.97 eV). These highly crystalline particles were shown to have a narrow size distribution and a quantum yield of >10%. [91]

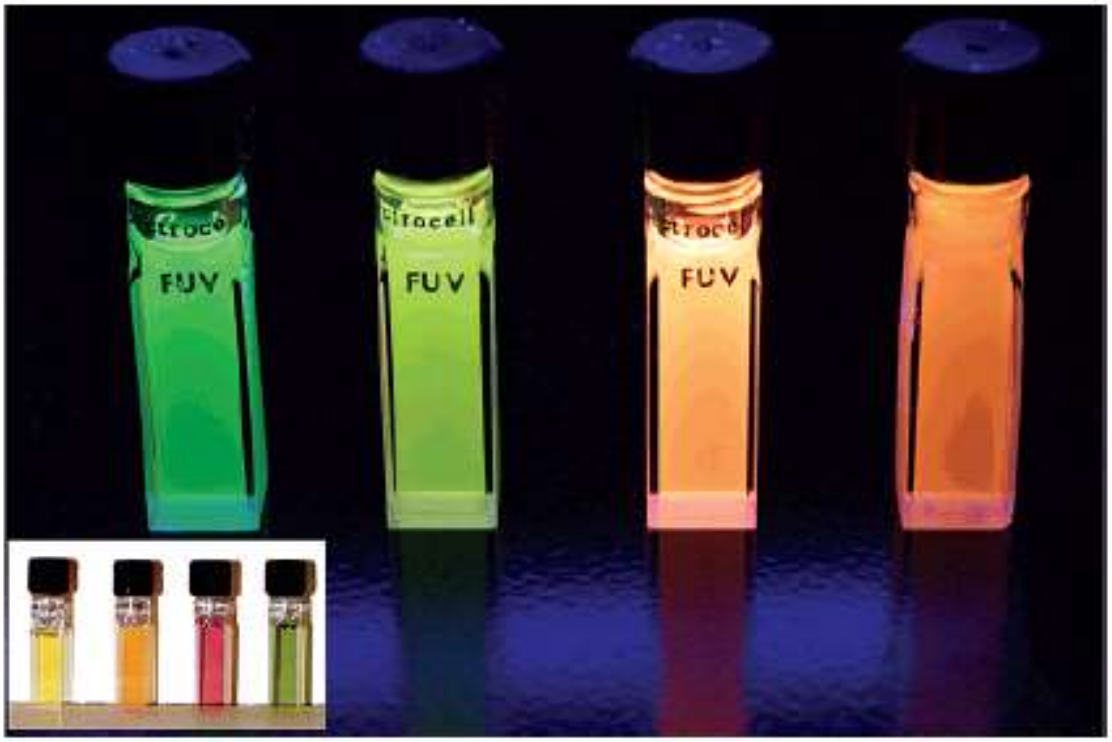

Figure 1. 11 – Luminescent metal-capped HgS particles.

1.7.3 Core/shell structures

The standard method of enhancing emission and protecting quantum dots is to grow (epitaxially) an inorganic shell on the core, which usually offers a barrier to oxidation and electronically passivates the surface, blocking trap states for non-radiative relaxation pathways. Following their initial report of thiol-capped HgTe, Harrison *et al*. described the synthesis of HgTe/CdS core/shell particles by mixing $Cd(ClO_4)_2 \cdot 6H_2O$ and $HSCH_2CH(OH)CH_2OH$ with a diluted HgTe growth solution, followed by the introduction of a N_2-buffered stream of H_2S whilst stirring at pH 10, followed by a brief period of refluxing. [92] In this example, the core HgTe particles, prepared as described above, exhibited a clear excitonic peak at *ca.* 850 nm, which shifted to *ca.* 920 nm upon deposition of the CdS shell. The HgTe/CdS particle emission did not shift and was found to be between

ca. 1000 and 1400 nm with a maximum at *ca.* 1110 nm and was importantly found to be relatively stable towards heating after shell deposition, unlike the naked dots, which exhibited emission which both shifted and quenched even upon short periods of refluxing. The particles exhibited a shift in the XRD pattern after shell deposition, consistent with the extra CdS layers, which could be observed by high-resolution electron microscopy. A variant on this synthetic method was reported by Zhang *et al*., who used essentially the same chemistry, but utilised NaHTe as a tellurium precursor for the core particles making the synthesis significantly easier, and DHLA as a capping ligand. [93] A comparison to $HSCH_2CH(OH)CH_2OH$-capped HgTe particle highlighted that the DHLA particles exhibited improved stability without the shell, even withstanding prolonged reflux. A detailed study uncovered highly tunable, clear and distinct excitonic features in the absorption spectra of HgTe/CdS, accessible by varying reflux times whilst the accompanying emission peaks were tunable between 900 and 1200 nm with quantum yields of up to 52% and again enhanced stability being observed in the core/shell particles. Arguably the most important point of the report is the brief description of the use of the core/shell nanoparticle in live animal imaging. This proves the stability of the particles (as live animals are difficult environments for quantum dots to maintain their light-emitting properties) and overcomes the preconceptions that Hg-containing particles cannot be used in imaging due to toxicity issues. Whilst no toxicity data was supplied, the proof of principle was compelling; it should also be noted that organomercury compounds such as Thiomersal, although toxic, have also been used as antiseptic and antifungal agents. [94]

HgTe can also be used as a shell material; [95] Kershaw *et al.* reported on the addition of a mercury salt to a preformed solution of CdTe, which was only weakly luminescent prior to the additional precursor addition. This resulted in the formation of a CdTe rich core with regions of HgTe on the surface, and it was suggested that over time, it was possible

that a redistribution may have occurred yielding a $Hg_{(1-x)}Cd_xTe$ material. A further synthesis step, adding extra Cd^{2+} precursor and further H_2Te gas resulted in a Cd/Hg/CdTe structure which exhibited emission which was shifted from a weak feature at *ca.* 580 nm to between 800 and 1100 nm with quantum yields of up to 44%. This work was extended in an attempt to prepare CdTe/HgTe/CdTe quantum dot quantum wells, in a similar manner to CdS/HgS/CdS described earlier, by preparing CdTe core particles and gradually adding precursors to deposit further shells. [96] [97] Once prepared, the particles underwent a substitution reaction over time yielding CdHgTe alloyed particles of varying compositions, which exhibited tunable emission from *ca.* 600 nm to 1350 nm, with quantum yields of up to *ca.* 50%. The actual structure of the alloyed particle was suggested to be complicated, with the potential for either HgTe or CdTe shells discussed. Similarly, CdHgTe rods have been prepared by the addition of Hg^{2+} to CdTe rods as templates, pushing the emission from *ca.* 550 nm to 850 nm. [98] Likewise, the addition of 2-aminoethanethiol-capped CdTe particles to a Hg^{2+} solution resulted in the precipitation of a $Hg_{1-x}Cd_xTe$ nanowire network, which showed an increasing red-shift with increasing Hg content. [99]

Alloyed particles, with tunable bandgaps, have been prepared in a one-pot reaction by using essentially the same chemistry employed to prepare thiol-capped HgTe, but including both Cd^{2+} and Hg^{2+} in the reaction vessel prior to the introduction of the NaHTe precursor, which is simpler to generate than H_2Te gas. [100] By varying the ratios of Cd:Hg precursors, alloys of various compositions were prepared from $Cd_{0.14}Hg_{0.86}Te$ to $Cd_{0.46}Hg_{0.54}Te$, with associated emissions from 1135 nm to 940 nm, with a maximum quantum yield of 45% for $Cd_{0.23}Hg_{0.77}Te$. The particles were found to be graded alloys; HgTe-rich in the core whilst CdTe-rich in the shell due to the solubility product of HgTe being significantly lower than that of CdTe, allowing HgTe to grow faster. This work was extended using similar chemistry in a one-pot reaction with small amounts of mercury

precursor (this time returning to the use of H_2Te as a precursor), obtaining materials with compositions of up to $Cd_{0.95}Hg_{0.05}Te$ and quantum yields of up to 60%. [101] Despite the small amount of mercury, the emission could be significantly red-shifted to up to 1600 nm simply by extending the reflux time. It is also noteworthy at this point to highlight the difficulty in making accurate quantum yield measurements, [102] notably in the spectral range of 800 nm to 1600 nm and that an improved integrating sphere set-up was developed to determine quantum yields that are often otherwise overestimated. [103] These materials could also be incorporated into NaCl microcrystals, which induced high photo and thermal stability, with solid-state quantum yields of up to 31%. [104]

Another way of preparing $Cd_xHg_{(1-x)}Te$ alloys was reported in a detailed study by Gupta *et al.,* who carried out ion exchange on 2.3 nm CdTe quantum dots (prepared by aqueous methods) with varying amounts of $Hg(ClO_4)_2{\cdot}xH_2O$; the resulting particles exhibited tunable emission between 541 nm and 1166 nm. After ion exchange, the emission quantum yield was found to fall by up to two orders of magnitude, although some degree of recovery was observed several days after the reaction. [105] Notably in this study, a kinetic investigation uncovered a rapid initial ion exchange followed by a slower phase attributed to cation intermixing. The same group extended this study by utilising a microfluidic reactor to take advantage of the controlled mass transport and rapid mixing to explore the kinetics in cationic exchange and alloy formation, uncovering a complex multistep process which can occur over weeks, with the Hg^{2+} initially exchanging at the surface and gradually cation diffusion occurring on longer timescales yielding structures which can include defects which impact the quality of the materials. [106] It was observed that the concentration of Hg^{2+} impacted on the recovery of the emission quantum yield, with lower doses resulting in slower exchange rate that resulted in a more complete recovery.

Qian *et al*. reported a very similar method for preparing CdHgTe (with Hg at 5%, 10% and 20%) with clear excitonic features and near band edge emission, tunable between 600 and 850 nm with prolonged heating. [107] To facilitate the use of the materials in biological imaging, a shell of CdS was deposited on the core alloyed particles using a cadmium salt and thioacetamide as precursors, and mercaptopropionic acid as a stabiliser. The addition of a shell appeared not to affect the position or emission intensity of the particles, and the particles were shown to be visible once injected into the leg of a live mouse, importantly becoming one of the first example of the use of Hg-containing particles in the biological imaging of a living animal, although no details of toxicity were supplied. [107]

Despite containing both cadmium (and more interestingly mercury) these particles have been used further in several biological imaging studies. In one of the earliest studies, simple CdHgTe particles (without a shell, and with a mercury-rich surface) prepared as described earlier were found to be safe in doses up to 10.5 mg g^{-1}, although 2 mg g^{-1} were often used as this greatly reduced the toxicity whilst maintaining the optical properties. The particles were found to be effective near-IR imaging agents, did not exhibit agglomeration although they were found to accumulate in the liver after injection, whilst evidence was found of long time retention in the intestine, suggesting liver-intestine circulation and clearance through this pathway which further reduced the toxic impact of the particles. [108] The same material was also conjugated to folic acid and used successfully in targeting and imaging S180 carcinosarcoma tumours (Figure 1.12). [109] Other studies showed that these particles (and CdTe) were cytotoxic to human breast and prostate cells, but cleared rapidly from the site of injection. [110] Core/shell CdHgTe/CdS particles, prepared as described above, were also used in effectively imaging the spinal column of a mouse model and in this case the maximum safe dose was found to be 50 mg g^{-1}, clearly indicating the shell

reduced toxicity. [111] It is also worth noting here that CdHgTe quantum dots prepared by aqueous chemistry have also been phase transferred to an organic phase by the ligand exchange procedure mentioned earlier, [79] in preparation for the deposition of a ZnS shell by organometallic precursors. [112] During phase transfer and shell precursor addition, the emission quantum yield of the core particles was quenched, yet recovered to approximately the initial value after shell deposition, which was accompanied by a significant emission red-shift, the origin of which is unknown. The resulting CdHgTe/ZnS core/shell particles, with quantum yields between 20% and 50%, were then encapsulated in phospholipid micelles and used in simple cell imaging experiments.

Interestingly, Hg^{2+} has also been doped into an aqueous dispersion of CdMnTe nanoparticles after synthesis by exposing the preformed nanocrystals to a 0.1 M solution of $Hg(ClO_4)_2$, followed by passivation with bovine serum albumin (BSA). The resulting CdTeMnHg–BSA nanoparticles exhibited a significant shift in absorption band edge with the excitonic feature shifting from *ca.* 575 nm to *ca.* 700 nm, and the emission maxima from *ca.* 625 nm to 775 nm. The quantum dots with the shifted emission profiles were then used as a contrast agent to image vessels in and around a murine squamous cell carcinoma in a C3 mouse, including blood vessels, *ca.* 100 mm at a depth of several hundred millimetres and a beating heart through up to 2 mm of skin, bone and fat. The particles did not show any evidence of emission quenching over one hour of continuous illumination, unlike ICG, a common dye with optical properties in a similar spectral region. There was no toxicity associated with the particles over the course of the experiment, or over a three-day period after subcutaneous injection. [113] A related material, $Zn_xHg_{1-x}Se$ has been simply prepared at room temperature using proteins (such as bovine serum albumin, BSA) as passivating agents, whilst utilising metal salts of different ratios and NaHSe as precursors. [114] The resulting nanomaterial, *ca.* 4 nm in diameter, exhibited emission between *ca.* 670

nm and 910 nm, tunable through the constituent elements, with emission quantum yields of up to 25.6%. The choice of Zn as a constituent of the alloyed particle was driven by the need to coordinate a number of amino acid residues to the material surface. Whilst the protein was incorporated into the nanoparticle synthesis as a capping agent, it was found that the presence of mercaptopropionic acid (MPA) as a co-ligand was essential for high quality optical properties. These particles were then utilised in imaging HeLa cells. A related material, $Zn_xHg_{1-x}Se_yS_{1-y}$, prepared in a similar manner, were used in an *in vivo* imaging system where excess QDs not used in tumour imaging were etched and cleared through the renal system. [115] Notably, no toxicity was observed.

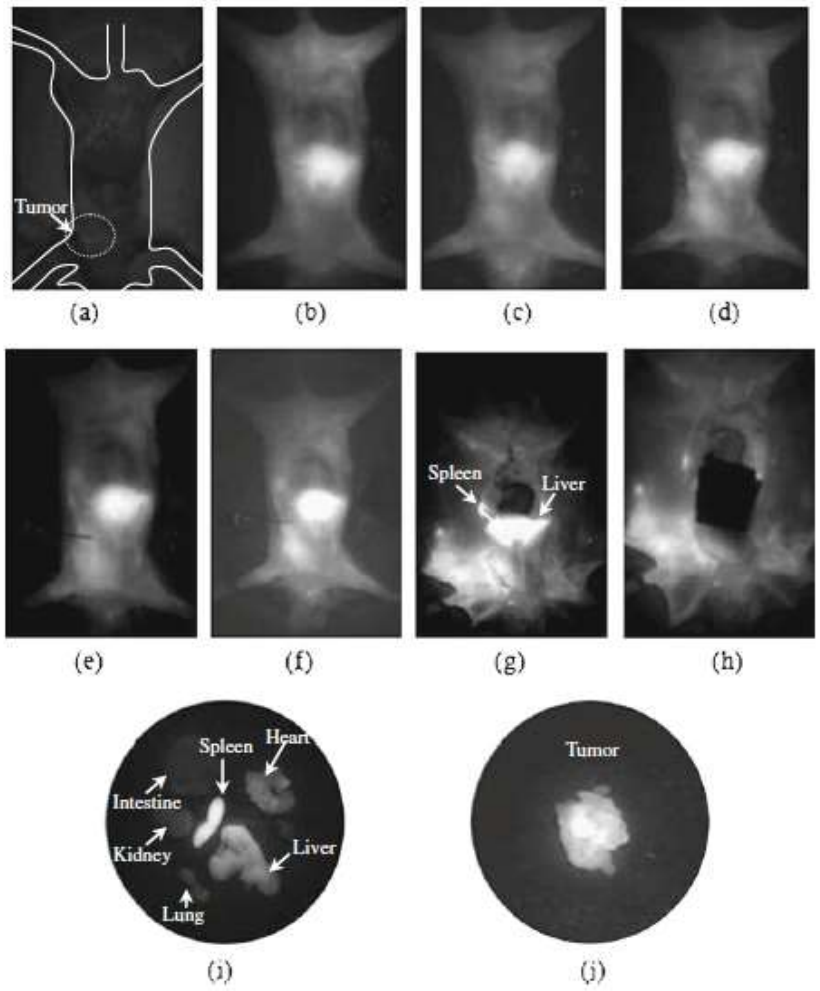

Figure 1. 12 – A series of images of a mouse treated with CdHgTe quantum dots. (a) Background scan prior to particle injection; fluorescent images after (b) 1 minute; (c) 5 minutes; (d) 1 hour; (e) 2 hours; (f) 5 hours; (g and h) images of the mouse after a thoracotomy; (i) major organs harvested after 6 hours; (j) the harvested tumour.

1.7.4 Metal-organic related routes

The majority of work mentioned so far was based on aqueous solution chemistry, finding its roots in traditional colloidal sciences. One of the most important advances in the preparation of quantum dots is the emergence of the 'TOPO' route (so named after the capping agent trioctylphosphine oxide, TOPO), reported by Murray *et al.* in 1993,1 which utilised organometallic precursors inspired by the work of Steigerwald as described earlier, combined with the use of phosphine oxides as a capping ligand, inspired by the early work of Bawendi *et al.* [116] This allowed the preparation of quantum dots under inert atmospheres at high temperatures (routinely up to 350 °C) resulting in passivated, relatively monodispersed, crystalline materials with extremely high-quality optical properties. This synthetic strategy allowed the preparation of other semiconducting systems not normally considered accessible by aqueous chemistry, notably the III–Vs and IV-VI families of materials, and has been expanded to cover infra-red emitting particles, including mercury chalcogenides. [117] Initial work by Murray on the synthesis of II-VI quantum dots utilised $Hg(CH_2C_6H_5)_2$ as the group-II precursors toward Hg chalcogenides, with synthesis temperatures reportedly as low as 100 °C, although no optical characterisation was reported. [24] [118] One of the first attempts to prepare HgTe using the TOPO route utilised $HgBr_2$ and trioctylphosphine telluride (TOPTe) as precursors in the presence of various stabilising ligands, avoiding the use of metal alkyls. [119] The precursors were chosen whilst referring to work by Huang *et al*., [120] who reported a similar reaction proceeded via the air sensitive intermediate $[Hg_3(TePR_3)_3Br_5][HgBr_3]$, although further reports in deducing mechanisms for PbSe and CdSe systems later emerged that highlighted numerous potential pathways for quantum dot formation in the presence of trioctylphosphine, a known reducing agent. [121] [122]

The simplest chalcogen precursors for quantum dots prepared by a binary route are the elements dispersed/dissolved in a solvent, usually a long chain phosphine (although alkylamines have also been found to be effective in the delivery of tellurium for monodispersed HgTe particle synthesis [123]). The reaction, which utilised TOPO and long chain amines were notable for the low injection and growth temperatures of 100 °C and 70 °C respectively, a common reaction condition in the synthesis of mercury chalcogenide nanoparticles using inorganic and metal-organic precursors. The resulting HgTe particles were relatively large, *ca.* 20 nm although no emissive properties were reported. Using an effective mass approximation, it was determined that the excitonic diameter for HgTe was 80 nm with a semimetal to semiconductor transition at *ca.* 18 nm. Similar results using effective mass approximations were reported in another study into the electronic structure of HgTe quantum dots and associated g factors, [124] although it should be noted that such calculations may be too simplistic as the effective mass approximation neglects non-parabolicity and applying the Brus equation to the light hole bands is known to give inaccuracies. [125]

Piepenbrock *et al*. developed this route further and reported a similar synthesis of organically passivated HgTe nanocrystals. By using $Hg(O_2CCH_3)_2$ complexed to excess hexadecylamine in ethanol, cooled in dry ice, followed by the drop-wise addition of trioctylphosphine telluride (TOPTe), HgTe quantum dots formed as a dark precipitate. [126] The precipitate was allowed to cool to -78 °C for 10 minutes, and then washed in acetone and dissolved in toluene. The result confirmed the observation of rapidly growing zinc blende particles with average size *ca.* 3.2 nm in diameter, exhibited an excitonic shoulder at *ca.* 1120 nm which red-shifted by 170 nm two weeks after synthesis. The emission was found to be between 1200 nm and 1600 nm, ideally suited for telecommunications, with freshly prepared samples exhibiting quantum yields of up 60%, again red-shifting over a

two-week period with a reduction in quantum yield to *ca.* 26%, still relatively high for inorganic quantum dots without a further inorganic shell. Li *et al.* reported a similar method and successfully synthesised HgTe quantum dots inspired by the work of Peng and Peng into the use of metal oxides as alternative precursors for group II elements. [127] Using Hg^{2+} complexed to oleic acid as a precursor in octadecene into which dodecanethiol was added followed by an injection of tributylphosphine telluride at room temperature. [128] The presence of the thiol was found to be essential, as the use of oleic acid alone resulted in uncontrolled growth; in this case, the thiols were found to bind stronger than carboxylic acids. Higher synthesis temperatures (130 °C) also resulted in the reduction of the Hg^{2+} precursors to elemental Hg. The reaction proceeded rapidly, the solution turning a dark colour in *ca.* 1 minute consistent with HgTe formation. The resulting zinc blende structured HgTe particles capped with dodecanethiol were *ca.* 2.3 nm in diameter and the absorption spectra obtained after 5-second growth showed an excitonic peak at *ca.* 850 nm, which blue-shifted to *ca.* 715 nm over a further minutes growth, after which the band edge red-shifted to *ca.* 750 nm. Interestingly, the emission profile, a single peak at *ca.* 825 nm appeared to shift to a much lesser degree, with a quantum yield of between 20 and 30%, which was stable over several months in the dark at room temperature. The lack of emission tunability and observed stability in peak position may in part be due to limitations in the spectrometer used.

Kim *et al*. again used a similar synthetic procedure, using $Hg(O_2CCH_3)_2$ complexed to a mixture of dodecanethiol and oleylamine in diphenylether, into which was injected TOPTe at room temperature followed by heating at one of a range of temperatures between 60 °C and 100 °C for 10 minutes. [129] The resulting HgTe quantum dots also possessed a zinc blende core, were between 3.6 and 7.2 nm in diameter and relatively monodispersed with absorption edges between 900 nm and 1300 nm, and emission between 1050 nm and

1420 nm. The quantum yield was determined to be between 8 and 10% and the presence of the thiol was again confirmed to be essential for colloidal stability and was identified as a capping agent using XPS. Samples prepared by this method were used in the manufacture of photodetectors up to three months after synthesis, whilst related materials have been used in the preparation of a MoS_2–HgTe hybrid photodetector. [130]

The above TOPO-based routes are notable for the low synthesis temperature, a key parameter in the formation of mercury chalcogenide nanoparticles using metalorganic-type synthetic pathways. In most of the non-aqueous synthetic routes, temperatures normally associated with the synthesis of the II-VI family of materials (such as CdSe, 4250 °C), reportedly gave bulk HgTe. To avoid the rapid growth to bulk HgTe, Keuleyan *et al*. suggested a viscous reaction mixture obtained by a high concentration of precursors was a desirable factor in maintaining an acceptable size distribution over a prolonged growth period. [131] In this case, HgC_{l2} was dissolved in oleylamine at a ratio of 1:120 and injection of TOPTe at between 60 °C and 100 °C resulted in a black colouration in the reaction flask obtained after 30 seconds. Aliquots were taken and growth quenched by injection into C_2C_{l4} containing long chain thiols, which replaced the amine and chloride on the particle surface. The resulting particles, the size of which was controlled by the injection temperature, had excellent optical properties, with tunable emission from 1.3 mm to 5 mm and well-defined associated absorption band edges with clear excitonic peaks. The particles showed evidence of a tetrahedral morphology, especially at larger sizes, consistent with the slow growth of a zinc blende crystal. A detailed study [132] of the optical properties of these materials between 1550 nm to 5500 nm showed a lower quantum yield value compared to previous reports on similarly-sized HgTe dots prepared by the aqueous method, and also reported a quantum yield drop from 0.1 to 10^{-4}% at lower energies, attributed to energy transfer to ligand vibrations. These materials were used in photodetectors between 2 mm and 5 mm [133] and

materials prepared based on this method have also been found to exhibit ultralow threshold optical gain and amplification of stimulated emission, assigned to a transition between the conduction band and surface states. This work was notable for the report of long gain lifetimes, with the potential for electrical pumping. [134] [135] For such materials to be used routinely in real-life applications, the absolute positions of the energy and Fermi levels need to be known as band alignment is essential in applications such as solar energy conversion (charge carrier separation), [136] light-emitting devices (charge injection) and thermoelectric devices. [137] Specifically for mercury chalcogenide quantum dots, the stability of doped particles is dependant on the relative energy levels of the particles and the environmental Fermi level, and these have been determined using electrochemistry. [138]

Further reaction modifications, such as diluting the TOPTe solution with oleylamine resulted in clearer excitonic features in the absorption spectra, with up to five electronic transitions being observed. [139] To grow particles with emission beyond 5 mm, raising the synthesis temperature or extending the reaction time resulted in materials that precipitated after isolation, and a secondary precursors addition strategy was adopted to grow particles that could withstand isolation in the growth quenching solution. These larger particles, with crystal facets up to 20 nm, did not show any excitonic features, consistent with polydispersed samples but were found to exhibit photo-conduction up to 12 mm.

The main issue with HgTe quantum dots grown from organic solutions is their tendency to aggregate due to their poor surface stability. This, as described above, could be overcome using thiols as strongly binding stabilising agents. Non-aggregating particles could also be prepared using $((CH_3)_3Si)_2Te$ as a precursor, avoiding the use of trioctylphosphine telluride and the poorly coordinating trioctylphosphine as a capping ligand. [140] The inclusion of a large excess of mercury precursor coordinated to a long chain amine presented a surface species that led to enhanced colloidal stability and superior

monodispersed samples. These non-aggregating particles also exhibited air-stable n-doping as determined by absorption spectroscopy and cyclic voltammetry (Figure 1.13). Mercury chalcogenides appear to be excellent examples of self-doped quantum dots and further examples will be described later.

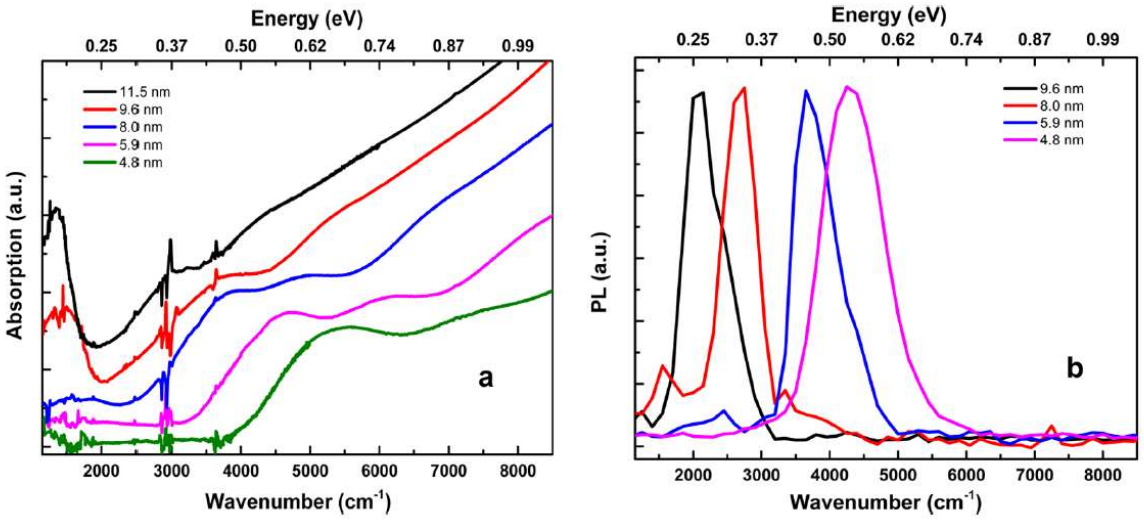

Figure 1. 13 – (a) Absorption spectra of a range of HgTe quantum dots in tetrachloroethylene, showing a clear intraband absorption feature at ca. 1500 cm. (b) Emission spectra from a range of HgTe quantum dots.

Again, to find practical applications in photonic devices, the quantum dots must be able to be manipulated into thin films or similar structures. Due to the particle's tunable optical properties beyond 5 mm, these materials have the potential to push the current limits of colloidal quantum dot-derived devices. In key studies, [11] [141] [142] Keuleyan described the application of HgTe quantum dots with optical properties in the mid-infra-red region between 3 mm and 5 mm as photodetectors. In this case, a slightly different method of preparing the particles was utilised, where the reaction was carried out in ethanol at a range of temperatures from 0 °C to 90 °C, obtaining quantum dots with a range of absorption features from *ca.* 1 to 5 mm respectively. Drop-cast films were then prepared from particles

of either 10.5 - 2.5 nm HgTe (band edge of *ca.* 5 mm) or 7.1 - 1.0 nm particles (band edge of *ca.* 3 mm) which showed some evidence of particulate aggregation, resulting in an inherent conductivity without further treatment. These unoptimised, simply-prepared films compared favourably with quantum-well infrared photodetectors and type-II strained lattice detectors, despite the facile method of preparation. Also, of note is the unusual photoconductivity mechanism. Quantum dots of HgTe, prepared as described above, were drop-cast onto a stainless-steel electrode, immersed in a solution of 1,7-heptanedithiol, dried and underwent electrochemical measurements that revealed that the films were ambipolar, with a strong p-photoresponse that would suggest their use as the p-side in a heterojunction. [143] Whilst such particles were found to make effective photodetectors, the use of the dithiols was found to be essential. Replacement of the native ligand with the inorganic ligand As_2S_3 was also found to be an acceptable surface species for stable photodetectors, as it reduced C–H vibrations in the mid-IR region. [144]

Whilst HgTe is the most explored material in this family, others have also been prepared. Mercury sulfide (HgS) particles have been synthesised in a similar manner. In a typical example, sulfur powder was dissolved in octadecylamine and octadecene, degassed, heated to between 100 °C and 230 °C, then maintained at 100 °C until required. [145] In a separate flask, HgO was dissolved in oleic acid and octadecene and also heated to 100 °C, whereupon the sulfur precursor was injected into the flask and stabilised at 80 °C for one hour. It was found that including octadecylamine was essential for reproducibility, and that an injection temperature above 100 °C resulted in polydispersed particles. Using the sulfur precursor prepared below 160 °C resulted in the formation of HgS nanoflowers up to 33 nm in diameter, whilst dot-shaped particles, *ca.* 6 nm in diameter dominated when a precursor prepared at a higher temperature was used. Both sets of particles exhibited a cubic crystalline core. Using sulfur precursors prepared at different temperatures also impacted

on the quality of the absorption spectra, with most precursors giving samples that exhibited featureless spectra, although in some cases excitonic shoulder were observed at *ca.* 800 nm. No emission spectra were reported. A similar route was reported by Wichiansee *et al*.[146]where TOPO was used instead of an amine and once again a hot solution of sulfur precursor was utilised, in this case, dissolved in trioctylphosphine (TOP). The resulting particles were dot shaped, *ca.* 4 nm in diameter, and exhibited the β-HgS crystalline phase. Both these reports were unusual as they highlighted the unreactive nature of the sulfur precursor, a factor normally lost in high-temperature syntheses of other quantum dots (although the inert nature of TOP = S has been commented on previously [147]). The particles displayed an excitonic shoulder at *ca.* 900 nm, with weak photoluminescence at *ca.* 1100 nm, attributed to two distinct processes. Following previous calculations of the electronic properties of mercury chalcogenide quantum dots using effective mass approximations that were found to be inadequate, an atomistic tight binding approach was utilised and found to be in good agreement with the experimental results. Jeong *et al*. also explored the synthesis of HgS quantum dots, and highlighted that the use of TOP = S as a precursor was not successful, and used $(NH_4)_2S$, $((CH_3)_3Si)_2S$, or $CH_3C(S)NH_2$ as a sulfur source in a room temperature synthesis instead. [148] This report is also noteworthy for the in-depth examination of the electronic structure of the resulting β-HgS quantum dots, and the intimate link between the surface and quantum states that shifted above or below the Fermi level, essentially doping the particle. This was elegantly demonstrated by the deposition of successive Hg^{2+} and S^{2-} layers, which drastically shifted the absorption spectra. The unusual electronic properties of these n-doped particles such as air stability and conductivity were in part attributed to the redox potentials. The optical bandgap was found to be *ca.* 0.6 eV, whilst weak intraband emission (quantum yield between 10^{-3} to 10^{-4}) was observed at *ca.* 5 mm, and interband emission was observed only after capping the particles with a CdS shell.

A similar synthesis reported from the same group described how a non-polar solution of HgC_{l2} in oleylamine, trioctylphosphine and tetrachloroethylene was injected into an aqueous solution of $(NH_4)_2S$ at room temperature, followed by 30 minutes of growth again resulted in β-HgS quantum dots with a doping density of 2 electrons per particle. [149] A shell of CdS was grown using similar chemistry, yielding particles with tetrahedral and irregular structures giving a type-I HgS/CdS core/shell structure. The particles again showed intraband and interband features, the former of which disappeared upon shell growth although weak intraband emission could still be detected. For the larger HgS particles, a surface plasmon was also observed. Band edge emission was observed from the core/ shell materials with a quantum yield of *ca.* 5%. Several other amendments to this route have been reported, including the ligand exchange of oleylamine-capped HgS using NH_4Cl to give a –Cl terminated surface, which resulted in the particles being readily transferred into a polar solvent. Such particles still exhibited intraband transitions under ambient conditions, thus proving that such transitions do not require the presence, for example, of a thiol group. [150] Field effect transistors using oleylamine-capped HgS have been prepared, with an electron mobility of *ca.* 1.29 $cm^2\ V^{-1}\ s^{-1}$, a relatively high value assigned to the excess electrons in the doubly occupied quantum states. [151]

Mercury selenide (HgSe) has also been explored, although not in the same depth as HgTe. As described above, the simple aqueous synthesis towards thiol-capped HgSe resulted in materials with emission vastly inferior to that of the tellurium analogue. [10] In recent years, Esmaeili-Zare *et al.* used a sonochemical technique to synthesise HgSe nanocrystals with a reported band edge of 2.23 eV. [152] The report described the use of $SeCl_4$ and $HgCl_2$ in the presence of hydrazine and capping agents, where ultrasonic waves were used to irradiate the reaction to form the required nano-crystals. The same group developed cubic phase HgSe particles using a similar synthesis method with a band edge

of 3.15 eV. [153] Attempts to make HgSe via the 'TOPO'' route, using mercury acetate and trioctylphosphine selenide (TOPSe) as precursors, and TOPO as a surfactant in ethanol at room temperature yielded air-sensitive zinc blende HgSe particles approximately 5 nm in diameter, approximately spherical with a slight aspect ratio. [12] The particles exhibited an excitonic shoulder at *ca.* 3 eV with no emission reported. It was found that the surfactant concentration dictated the particle shape, with a reduced concentration favouring an anisotropic morphology. This report also questioned why the reaction proceeded rapidly at a relatively low temperature and examined the potential reaction mechanisms and whether this may have an explanation. It was suggested that the standard redox potentials for the cation precursors may contribute, with the more positive species reacting readily with the phosphine present in the reaction yielding elemental metal, previously identified as an intermediate. This explanation was also used to explain why Pb-chalcogenides also formed rapidly in solution, whereas Cd-based materials were relatively controlled and synthesis of Zn-based quantum dots often required help when using a metal salt as a precursor. This system was explored further in this project, by removing the phosphine and utilising oleic acid as the capping agent in octadecene. [154] In this case, the reducing agent for the metal salt was unclear, although it was suggested that octadecene has been previously employed as a reducing agent. The reactions in these cases were carried out at 90 °C, room temperature, and whilst warming up from liquid nitrogen temperatures after room temperature injection. The separation of nucleation and growth afforded by the freezing of the reaction flask immediately after precursor injection yielded spherical monodispersed particles that close-packed on a grid, whilst higher growth temperatures resulted in materials with a range of sizes and morphologies. Interestingly, these materials were emissive at the band edge, with absolute quantum yields of *ca.* 7% with a spectral range of *ca.* 1000–1300 nm. A similar reaction was reported by Deng *et al*. in a study exploring

intraband transitions in HgSe. [155] In this synthetic route, self-doped HgSe quantum dots were prepared using HgC_{l2} and selenourea as precursors, and oleylamine as a capping agent with a reaction temperature of 110 °C. The particles, between 5 and 7 nm in diameter, were grown for up to 12 hours and the reaction halted using a solution of TOP, dodeceanethiol and tetrachloroethylene to quench growth. The resulting particles exhibited intraband absorption features between 3 and 5 mm and intraband photoconduction was observed and controlled when the particles were coated with sulfur on the surface using $(NH_4)_2S$. Interestingly, intraband photoluminescence was observed, with a QY of 1-5 x 10^{-4} % although this was not comparable to typical band edge emission. Further work confirmed that the surface capping agent was intimately linked to the doping level, which could be controlled to between 0.1 and 2 electrons per dot by altering the surface passivating species with those with differing dipoles. [156] The origin of the doping was suggested to be the reduction of the particles by water, and that the alignment levels explained why HgS and HgSe could be stable whilst negatively charged, whilst HgTe, which exhibits a band structure closer to the vacuum level is not. This work was extended to deposit a CdS shell on HgSe, by growing the core particles followed by the further addition and reaction of cadmium oleate (but not the chloride or acetate salts) and one of a number of sulfur precursors, typically H_2S. The previously observed intraband transition is notably absent in the resulting HgSe/CdS particles, with the emergence of a band edge excitonic peak, suggesting a type I core/shell system. The intraband emission is likewise quenched, with the emergence of an interband emission peak at *ca.* 2130 nm. The change in the optical properties of the HgSe particles strongly suggested the doping was lost during shell deposition, although this was recovered when the particles were deposited and dried as a film and was even more pronounced upon further ligand exchange. [157]

Alloys of mercury chalcogenides prepared by organometallic based chemistries have also been reported but not in the same depth as the materials prepared by aqueous routes described above. The addition of $HgBr_2$ to preformed CdTe quantum dots resulted in the formation of a CdHgTe nanowire alloys-like structure, which was compared to macro-scale welding by cation exchange. [158] The optical properties of the resulting nanowires were shifted from the parent CdTe dots, with the excitonic absorption peak shifting from *ca.* 640 nm to *ca.* 800 nm, and likewise the emission maxima shifting from *ca.* 650 nm to *ca.* 850 nm upon alloying. Analogous work with CdSe quantum dots and nanorods as the parent material also exhibited a similar optical shift, although the emission was significantly quenched and the optical shift was less pronounced in the rods structures. [159] Similar work was reported by Smith and Nie, [160] who used mercury octanethiolate to induce cation exchange in CdTe, again producing alloyed structures with reduced bandgaps, which exhibited the tunable associated red-shifted optical properties. In this case, the emission was reported to be tunable with Hg cation content from *ca.* 600 nm to *ca.* 1000 nm. The use of the thiolate compound was shown to be essential, as this resulted in particles with unaltered morphologies, unlike the use of $HgBr_2$ mentioned above which gave wire-like alloyed particles. These particles were then subject to a shelling process, where it was found that a barrier layer of CdTe was essential before a further layer CdZnS was deposited. Failure to add a barrier layer yielded a strained interface and a type II heterostructure, resulting in a further red-shift in the optical properties. Once capped, the particle exhibited tunable emission from *ca.* 700 nm to *ca.* 1150 nm, with quantum yields as high as 80% at room temperature. Smith extended the cation exchange of CdTe with a Hg species further, using computational models to explore the distribution of charge carriers in such structures. It was noted that by using larger CdTe particles and cation exchange, core/monolayer shell type structures could be obtained, whilst the use of CdTe particles below 5 nm resulted in

homogeneous alloying. It was also observed that certain precursors (mercury thioglycerol and mercury octanethiolate) resulted in slow exchange, whilst mercury acetate resulted in rapid exchange, allowing structures – and optical properties – to be tailored. [161] Mercury octanethiolate has also been used with CdSeS quantum dots to prepare $Hg_xCd_{1-x}Se_yS_{1-y}$ quantum dots. [162] Cation exchange has also been used with particles of differing morphologies. Using nanoplates of CdTe instead of spherical particles, and using mercury acetate in oleylamine as the Hg source resulted in total cation exchange in *ca.* 1 hour, with notable red-shifts in the optical properties, giving HgTe nanoplates with emission at *ca.* 880 nm and linewidths with a full width at half maximum (FWHM) of 40 nm, substantially narrower than most other IR-emitting QDs. [163] These HgTe nanoplates, once deposited as a film and exposed to either ethanedithiol or S^{2-} ions exhibited a red-shift in the emission profile consistent with exciton leakage. The addition of S^{2-} ions resulted in the formation of an n-doped HgS layer, whilst ethanedithiol resulted in p-type behaviour. [164]

Cation exchange was also used to make $Cd_xHg_{1-x}Se$ nanoparticles, starting from CdSe quantum dots using mercury oleate as a cation source at 150 °C. [165] This route was notable as the bandgap did not initially appear to shift, with a slight blue-shift in the initial excitonic feature of CdSe upon the first addition of Hg precursor, attributed to the possibility of a shrinking CdSe core combined with an HgSe shell giving an inverse type-I structure that cancelled out the blue-shift, or the initial coverage of the CdSe particles with Hg^{2+} ions. After several additions of Hg precursor, a feature emerged at *ca.* 5000 nm in the absorption spectra, attributed to an intraband transition that ultimately transformed to a surface plasmon resonance. The addition of the mercury precursor also appeared to significantly increase the quantum yield of the sample, with increased Hg addition red-shifting the emission from *ca.* 560 nm to *ca.* 650 nm. The particles appeared as graded alloys, exhibiting a mercury-rich surface and cadmium-rich core.

Polydispersed $HgSe_xS_{1-x}$ particles with a cubic crystalline core were prepared by the reaction between mercury acetate in tributylphosphine and $Me_3Si–SeS–SiMe_3$ in toluene at -78 °C, giving an unidentified pink solid which decomposed into the particles upon warming to room temperature, although few optical properties were provided. [166] This report was notable due to the use of a single source precursor for both chalcogen species; as shown earlier, most single source precursors provide both anion and cationic species. A more recent example which utilised both single inorganic compound and the high-temperature route was reported by Kedarnath *et al*., who thermolyzed $[Hg(TeCH_2CH_2N(CH_3)_2)_2]$ in hexadecylamine at *ca.* 100 °C giving spherical HgTe particles with a cubic crystalline core, with an average diameter of approximately 7 nm. [167] In this example, the inclusion of a manganese salt resulted in Mn-doped HgTe particles. The related compound, $[Hg(SeCH_2CH_2CH_2N(CH_3)_2)_2]$, when thermolysed in tributylphosphine also yielded nanoparticulate HgSe however the phosphine did not coordinate to the surface. [168] Single source precursors to HgS nanoparticles include $Hg(S_2CNR_2)_2$ (where R = $CH_2C_6H_5$ or CH_3, $CH_2CH_2C_6H_5$) [169] [33] although these routes did not utilise surfactants or report the optical properties in any depth. Single source precursors are not always effective; attempted chemical vapour deposition of thin films using $M[(TePiPr_2)_2N]_2$ (M = Cd, Hg) as precursors was successful with cadmium, although yielded only tellurium thin films when the mercury complex was used. [170] Further investigations found a range of related compounds were successful precursors for HgSe and HgS, although these were not simple solution routes to nanoparticles.[171] A related compound, $[Hg(TePyridine)_2]$, when thermolyed in TOPO at 145 °C for 20 minutes yielded HgTe quantum dots although few details were reported.[172]

There are issues with both the aqueous and organometallic-based synthesis pathways, such as the tendency of water-prepared materials to aggregate when the particles

grow larger than *ca.* 4 nm, whilst the larger particles grown by the organometallic-type synthesis require a quick homogenous reaction, which is often difficult to achieve with larger batch sizes. A method based on the aqueous synthesis protocols has been developed by Abdelazim *et al*. using dimethylsulfoxide (DMSO) as a reaction solvent, which avoided hydrogen bonding and hence the aggregation of particles, and furanmethanethiol as a capping agent which bound to the nanoparticle surface whilst again reducing other interactions which would lead to particle agglomeration. [173] The telluride precursor was electrochemically generated H_2Te, which could be introduced to the reaction in multiple steps, allowing the slow growth of sequentially larger particles. The resulting HgTe quantum dots have excellent optical properties, even at longer wavelengths and large reactions volumes, with growth solutions of up to 500 mL batches achievable, and emission quantum yields of up 17% at emission wavelengths of 2070 nm. By varying the ligand to capping agent ratio and electrolysis current, differing particles sizes were obtained with different quantum yields. Materials with emission wavelengths between 1500 nm and 2000 nm and quantum yields as high as 40% could routinely be achieved. Materials prepared by this method were used in the manufacture of photodetectors and phototransistors. [174]

1.8 Conclusion

In summary, the synthetic chemical routes to nanostructures of mercury chalcogenides and their promising optical characteristics across the visible and near-infrared regions have been highlighted, offering alternatives to typical III–V and IV-VI based quantum dots. It is worth noting that so far, the synthetic chemistry might be considered variants of two routes – the addition of a tellurium source to an aqueous solution of thiol and mercury salt, or the metalorganic-equivalent where organic solvents and precursors are utilised. The advantage of the metalorganic route is the wider range of

synthesis temperatures available and hence the potential for differing particle sizes. Thus far, only a handful of precursors have been explored in both cases; usually metal salts as mercury precursors, and Te, NaHTe or a phosphine chalcogenide for the required chalcogen. It is well known that varying precursors can result in differing structures, and similar effects have also been observed by varying capping agents. To this end, synthetic chemistry has some way to go until it reaches the same level of sophistication enjoyed by cadmium-based quantum dots. Likewise, the range of core/shell structures and anisotropic materials based on mercury chalcogenides lack behind other quantum dot families, although it is only a matter of time until these novel structures emerge. With the emergence of novel, mercury-based materials will come improved devices and device structures, notably in the photovoltaic arena and one looks forwards to seeing stable efficient photovoltaic devices, and notably, IR emitting lasers at which, recent advances hint. It can also be noted that mercury chalcogenide particles have been, surprisingly, realised in biological imaging applications. Whilst one doubts whether such particles will find applications in a clinic, as highlighted, mercury-based medicine are not new. One of the most pleasing aspects in the emerging field of mercury-based quantum dots is the new physical properties not routinely observed in other families to the same depth, such as stable self-doping and even plasmonic effects. In short, exciting advances in the chemistry, physics, engineering and even biology of mercury chalcogenide quantum dots should be expected in the upcoming years.

1.9 Objectives

As it was briefly mentioned, in this project the synthesis of HgSe and HgTe quantum dots has been extended to a phosphine-free route, yielding near-infra-red emitting materials.[154] This has been implemented by utilising a combination of mercury(II) acetate ($Hg(OAc)_2$), oleic acid (OA), octadecene (ODE) and selenium (Se), including the addition

of an ionic liquid with sodium borohydride ($NaBH_4$) and tellurium (Te). In both cases, the process for these syntheses uses OA for the capping agent and ODE as a non-coordinating solvent and reduction agent, further use of sodium borohydride to assist with the reduction of Te. These newly developed methods seek to provide materials with improved optical properties and characteristics relative to previously reported HgSe and HgTe particles. [12]

Furthermore, as a means of developing new techniques in the formation of mercury chalcogenide quantum dots, a simple biosynthesis method has been implemented for obtaining highly crystalline HgTe nanoparticles. [87] This method utilises the mutual antagonistic reaction occurring within an *Allium fistulosum* (common spring onion) root after exposure to mercury and tellurium salts under ambient conditions. The resulting HgTe nanoparticles have been tested for optical characterisation and observed under transmission electron microscopy for structural analysis. It is anticipated that this approach will encourage further studies towards the advance of solid-state materials using less toxic and cost-efficient routes.

Chapter 2:

Synthesis of HgSe Quantum Dots

2.1 Introduction

As mentioned in Chapter 1, whilst the synthesis of HgTe has been relatively widely reported, the production of luminescent HgSe quantum dots has yet to be fully investigated. Mercury selenide, HgSe, is a negative bandgap semiconductor with a bandgap of -0.24 eV and an exciton diameter of 27.5 nm; smaller than HgTe (*ca.* 80 nm) but substantially larger than the majority of II-VI materials. [131] Using the aqueous route (which was successfully used to prepare thiol-capped HgTe) in an attempt to synthesis HgSe resulted in material with low quantum yields. [9] In recent years Esmaeili-Zare *et al.* used a sonochemical technique to synthesise HgSe nanocrystals with a band edge of 2.23 eV. [152] The report described the use of $SeCl_4$ and $HgCl_2$ in the presence of hydrazine and capping agents, where ultrasonic waves were used to irradiate the reaction to form the required nano-crystals. The same group have also developed cubic phase HgSe particles using a similar synthesis method with a band edge of 3.15 eV. [153] In a notable report, Kuno *et al.* reported high reactivity and instability in mercury chalcogenides. [91] By using a reverse micelle approach involving an amphiphilic surfactant, control over the particle growth was achieved, producing stable emissive HgSe clusters with a band edge at 595 nm (2.08 eV) with emission close to 630 nm (1.97 eV). These highly crystalline particles were shown to have narrow size distribution and a QY of >10%. [91] This group have previously reported the synthesis of HgSe quantum dots with tunable sizes and morphologies using inorganic precursors, but have not investigated the optical properties in any depth. [12] Here, the synthesis of HgSe QDs has been extended to a phosphine-free route, yielding near-infra-red emitting materials by utilising a combination of mercury(II) acetate ($Hg(OAc)_2$), oleic acid (OA), selenium (Se) and octadecene (ODE). The process for this synthesis uses OA for the capping agent and ODE as a non-coordinating solvent. The newly developed methods seek to provide materials with improved optical properties and characteristics relative to previously reported HgSe particles. [12]

2.2 Synthetic methodology

Mercury chalcogenide quantum dots are known to form at room temperature, making them ideal for simple synthesis and experimental tuning during the production process. [128] The synthesis process to obtain colloidal HgSe nanocrystals was split into three stages. The first step involved combining mercury acetate with oleic acid under heat and nitrogen to form the base solution. After reaching room temperature, the solution was kept under vacuum conditions for a few hours as a means to remove any build-up of acetic acid within the solution. The selenium (Se) precursor was prepared in the second stage by reacting degassed octadecene (ODE) with Se under nitrogen and high temperature until an amber colour solution is obtained. This was then allowed to cool down to room temperature, turning green in colour. The final stage involved injecting the Se precursor into the Hg base solution at room temperature and observing the colour change from yellow to amber to brown and subsequently into black. The obtained solution was purified using acetone resulting in the isolation of solid nanoparticles that were able to distribute into organic solvents, which in this case was toluene. The synthesis was repeated for a second time with the Se precursor being injected into the Hg solution under 100 ºC. Size-selective precipitation techniques were used in the purification process for both reactions to improve the monodispersity of the particles.

In addition to size-selective precipitation, another method of preparing monodispersed particles is to separate the nucleation and growth phases, usually achieved by utilising a high-temperature precursor injection and a slow, lower temperature growth step. This was attempted with the room temperature growth route by freezing the reaction to liquid nitrogen temperatures immediately after precursor injection. The reaction solution was then allowed to warm slowly to room temperature over a period of 8 hours followed by isolation of the particles as described above.

2.4 Structural analysis

In a standard room temperature reaction, multi-shaped, predominantly pyramidal-shaped HgSe particles (Figure 2.1A) were produced with an average size of 24 nm ± 4.1 nm, which were clearly larger than the analogous HgSe particles previously obtained.[11] The particles were relatively monodispersed with a range of shapes, including spherical, pyramidal and cubic, and appeared in some cases to aggregate. As shown in Figure 2.1B, particle aggregation was reduced by removing the acetic acid formed from the reaction between the mercury salt and oleic acid by vacuum evacuation. [175]

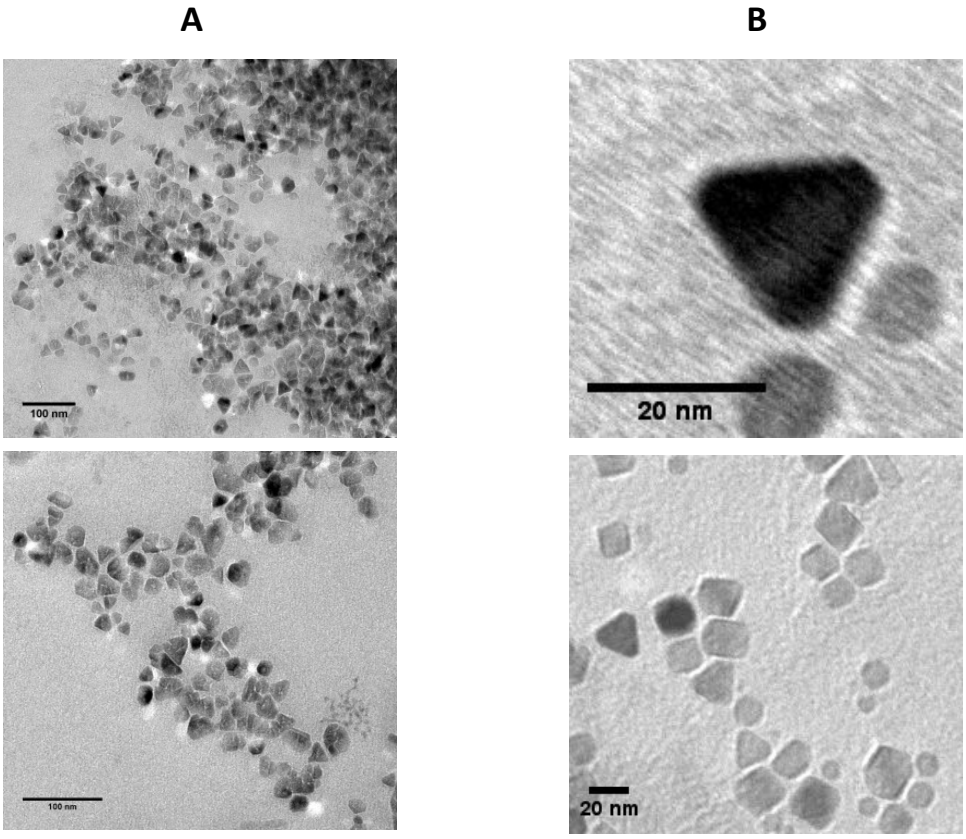

Figure 2. 1 - TEM images of HgSe nanoparticles synthesised at room temperature - A) Room temperature (aggregated due to acetic acid effects). Scale bars = 100 nm; B) Room temperature synthesis with reduced acetic acid. Scale bars = 20 nm.

This changed the mean particle size to 22 nm ± 2.6 nm, indicating a slight increase in monodispersity. As the technique of acetic acid removal was effective, it was used for all further synthesis of HgSe samples. The growth of mercury chalcogenides at low (room) temperatures has previously been observed, and suggested to be due to the positive redox potential of the mercury precursor, (E^0 $Hg_2^{2+} + 2e^- \rightarrow 2Hg$ is 0.79 eV, unlike the analogous Cd, Zn and Pb precursors which are all negative) which resulted in the room temperature reduction of the mercury precursor by the phosphine yielding Hg^0 monomers which then reacted with the chalcogen source. [12]

Whilst HgSe and HgTe were reported to form at low temperatures, HgS prepared by the use of mercury salts and TOPS was found to require a preheating step for the TOPS, attributed to the stronger phosphine-sulfur bond and low conversion rate. [146] Here, the source of mercury salt reduction is unclear, and whilst a recent publication has suggested that octadecene is a reducing agent, [176] this is far from proven. The mercury nuclei, once generated were then available to react with the selenium monomer provided by octadecene/selenium. [177] As the reaction proceeded smoothly at room temperature without the need for external heating, this presented the opportunity to measure the emergence of an optical band edge *in situ* by carrying out a reaction in an absorption cuvette and monitoring the band edge in real-time. The main aim was to observe the growth of the nanocrystals in accordance with their absorption spectrum. Figure 2.2 shows the emergence of the absorption features of HgSe particles prepared at room temperature from 2 min to 100 min. The emergence of an excitonic feature can clearly be seen at 55 minutes. Taking the emergence of the excitonic feature at 55 minutes at *ca.* 760 nm, and the excitonic feature at 90 minutes at *ca.* 820 nm, it can be estimated using the effective mass approximation explained in Chapter 1 sub-section 1.5.3 and assuming effective masses of electrons and holes at 0.03 and 0.78 respectively and a dielectric constant of 7.5, [12] that the

particles grew just 0.17 nm in 45 minutes at room temperature, which is much less than a unit cell of HgSe (6.085 Å).[178] This highlights how small structural changes can drastically affect the optical properties of nanomaterials with a large excitonic diameter.

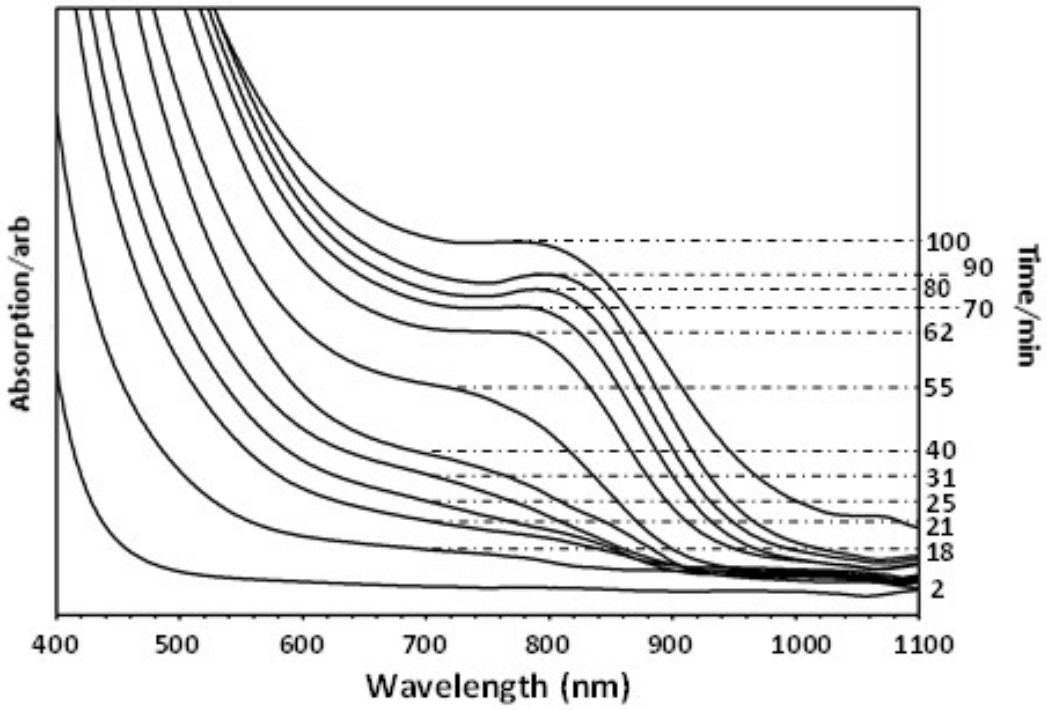

Figure 2. 2 – *In situ* Real-time monitoring of absorption features for room temperature growth.

The particles obtained from using liquid nitrogen after the precursor injection were observed to be monodispersed, approximately spherical in morphology (Figure 2.3) with some hexagonal and cubic particles observed. The average size of these particles was 14 nm ± 2 nm. The close-packing formation of these particles was observed, unlike particles prepared without acetic acid removal, which had a tendency to agglomerate. This indicates good oleic acid surface passivation during nucleation and a positively controlled growth process assisted by the sudden reduction of the reaction temperature.

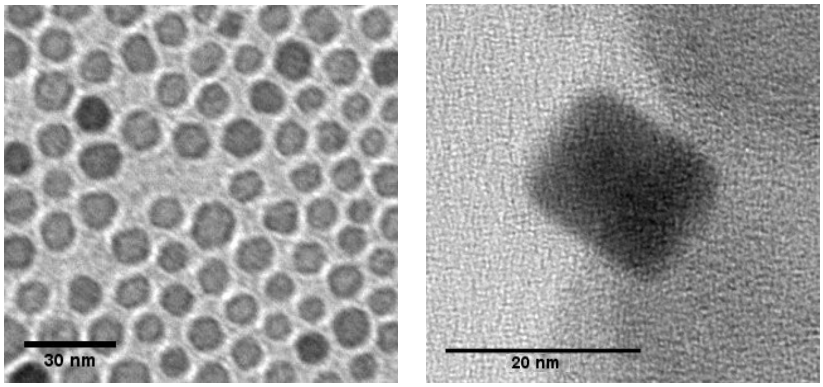

Figure 2. 3 - TEM images of HgSe nanoparticles synthesised using room temperature injection followed by freezing. Scale bars = 30 nm (left) and 20 nm (right).

The high-resolution electron microscopy (HRTEM) images of particles prepared by low-temperature growth (Figure 2.4) showed the highly crystalline lattice structure of these particles despite the absence of thermal annealing normally afforded by high-temperature growth.

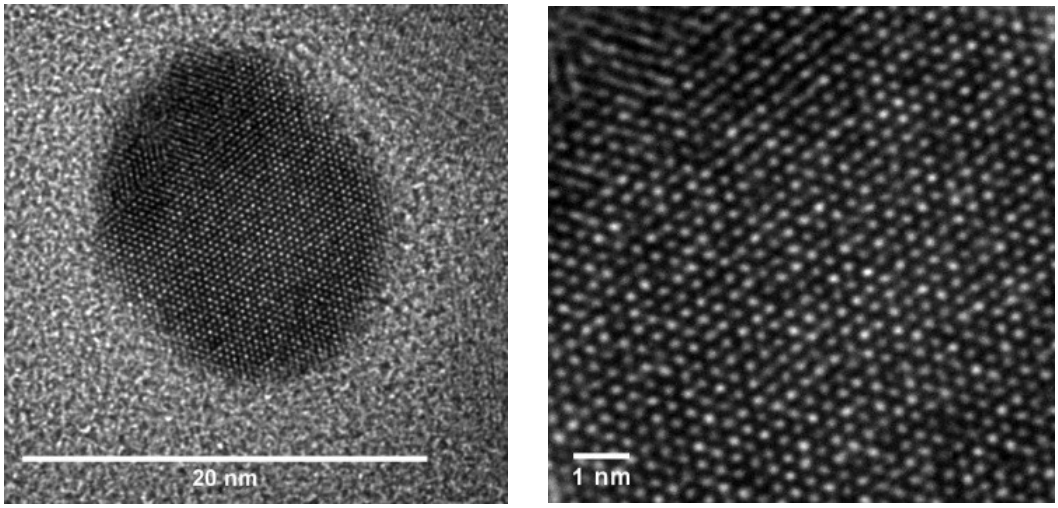

Figure 2. 4 – High-resolution transmission electron microscope (HRTEM) images after room temperature injection/freezing. The internal crystal structure is clearly visible. Scale bars = 20 nm (left) and 1 nm (right).

It should be noted that the nanoparticle sample shown in the HRTEM (Figure 2.4) has a slightly lighter colour in the centre in comparison to the outer edges, potentially indicating a weaker central structure. This could perhaps be due to metal oxidation and the initial signs of Kirkendall void formations. Discovered by Ernest Kirkendall in 1947, the Kirkendall effect in nanostructures is a phenomenon in material science which is linked to the inner diffusion process of two metals with different diffusion rates, resulting in the formation of vacancies within the crystal structure. This phenomenon has been observed and studied in various recent articles showing the formation of hollow nanoparticles. [179]

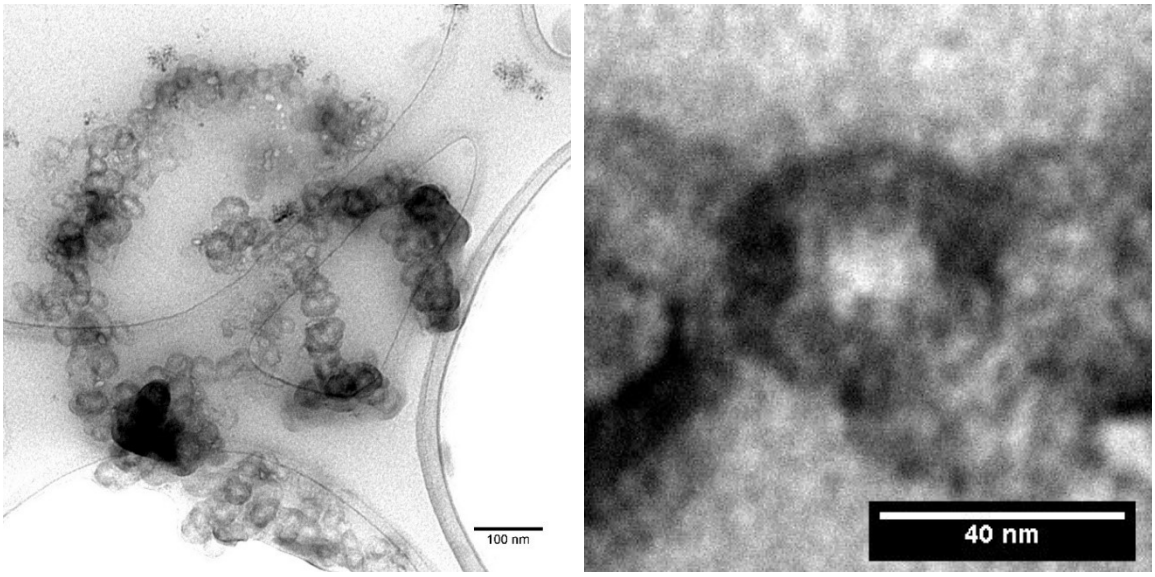

Figure 2. 5 - Transmission electron microscope images of HgSe nanoparticles after six months showing the Kirkendall void formation in the centre, scale bar = 40 nm (Right) and significant particle aggregation, scale bar = 100 nm (Left).

The same HgSe samples were observed again after a six-month period as a means to understand how their structure changes over time. The transmission electron microscope (TEM) images in Figure 2.5 clearly show the hollow central structure of the nanoparticles due to the Kirkendall effect. In addition to the structural change, significant aggregation was visible, potentially due to the loss of the particle's ligands. This is also supported by the fact

that these HgSe nanoparticles precipitate out of the organic solvent after a period of time and cannot be redispersed.

When the reaction was carried out at 100 ºC, the particles were observed to be significantly larger than those prepared at room temperature, approximately spherical and polydispersed due to rapid uncontrolled growth (Figure 2.6**)**. The average size obtained was 78 nm ± 58 nm. This was no surprise due to previously reported rapid growth observations from various mercury chalcogenides reactions at room temperature. [128]

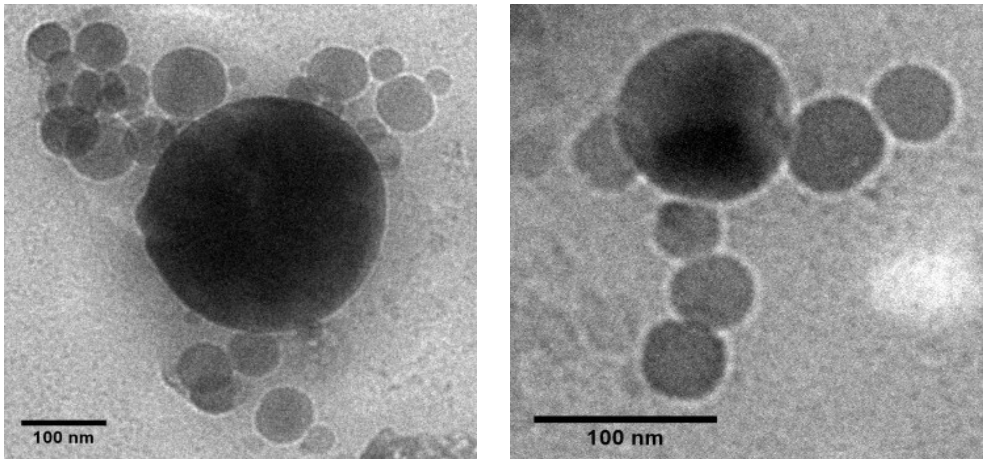

Figure 2. 6 - TEM images of HgSe nanoparticles synthesised at 100 ºC. Scale bars = 100 nm.

X-ray diffraction (on particles prepared at room temperature) confirmed the cubic zinc blende structure of the HgSe quantum dots (Figure 2.7), [89] similar to a recent report on the synthesis of HgSe and HgCdSe quantum dots prepared by an aqueous route. [180] In this case, the particles were used as near-infrared photodetectors. The broad reflection at *ca.* 20 °2Θ was attributed to the amorphous glass slide used to hold the sample.

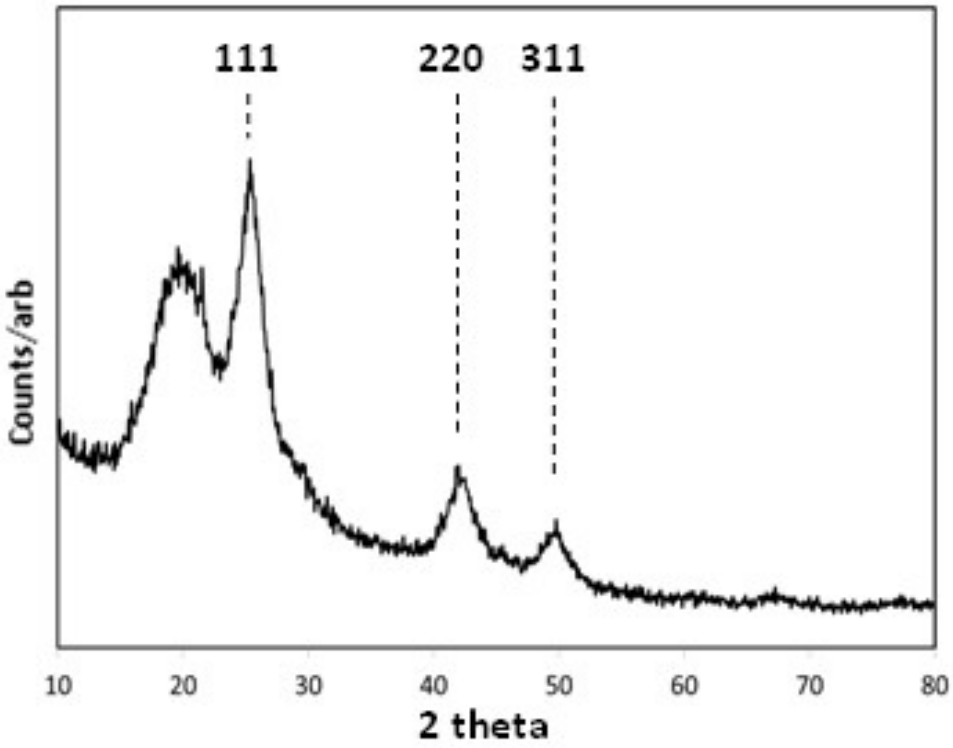

Figure 2. 7 – Measured X-ray diffraction pattern (XRD) of zinc blende HgSe particles prepared at room temperature and associated Miller indices.

2.5 Optical analysis

Optical spectroscopy of the synthesised materials showed size-dependant absorption and emission in the near-infrared region (Figure 2.8). Material prepared at 100°C displayed an onset of absorption at approximately 1300 nm (0.95 eV) and an excitonic shoulder at *ca.* 1050 nm, a substantial widening of the bandgap of *ca.* 1.2 eV. Emission was found to be slightly Stokes shifted with a maximum at *ca.* 1250 nm (0.99 eV) with a full width at half maximum (FWHM) of 184 nm.

Room temperature injection and growth resulted in smaller materials with an absorption band edge onset at *ca.* 1100 nm (1.12 eV) and a less well-defined excitonic feature, possibly attributable to the less well-defined separation of nucleation and growth. The blue-shifted onset of absorption relative to the materials prepared at 100°C is expected

from smaller particles exhibiting a larger widening of the bandgap. Emission was found to be Stokes shifted, with a maximum at *ca.* 1070 nm (1.15 eV) with a FWHM of 135 nm.

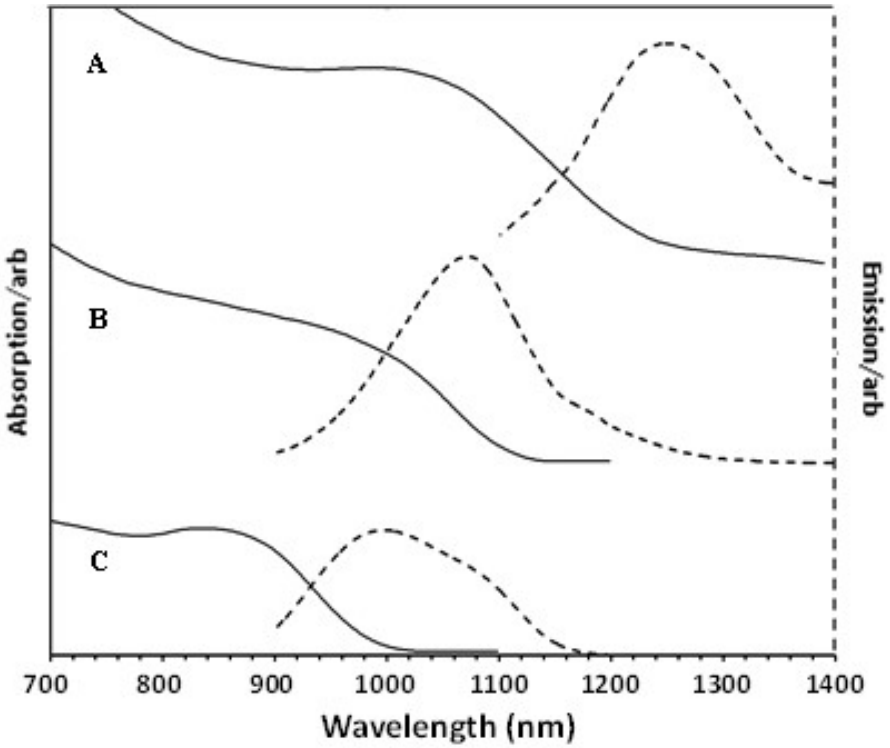

Figure 2. 8 - Absorption and emission spectra of HgSe nanoparticles synthesised at various growth temperatures. A) 100 ºC; B) Room-temperature; C) Room-temperature injection/freezing.

Particles prepared by room-temperature injection followed by immediate freezing displayed an onset of absorption at *ca.* 1000 nm (1.24 eV), with an excitonic feature at *ca.* 875 nm. Emission was again Stokes shifted from the band-edge with a maximum at *ca.* 1000 nm (1.24 eV) with a FWHM of 170 nm. This increase in the bandgap confirmed that particles prepared by the slow growth method were smaller than the particles grown entirely at room temperature. All particles displayed similar emission quantum yields (approximately 4 %) irrespective of the method used to manufacture them, and whilst significantly lower than prevalent HgTe quantum dots prepared by analogous synthetic techniques, [58] is one of the highest recorded for HgSe.

2.6 Conclusion

This chapter establishes a successful synthetic pathway to prepare crystalline HgSe quantum dots at low temperatures using a simple phosphine-free method. The particles, with a range of different morphologies, were approximately 15 nm to 200 nm in diameter and exhibited tunable band-edge emission between 1000 and 1350 nm with a quantum yield of approximately 4 %.

Another interesting observation was the growth rate of the HgSe nanocrystals at room temperature using their absorption spectrum in Figure 2.3. This clearly displays the nucleation process without the use of any external catalyst. The growth that took place within the spectrometer evidently shows the development of the excitonic peaks over time and the rate at which the quantum dots are formed. HgSe particles are ideal candidates for this observation as their growth at room temperature is not aggressive and can be controlled even further by using sudden temperature reduction.

Despite this, a significant problem facing the production of mercury chalcogenide QDs is the rapid aging of the nanoparticles. Freshly prepared mercury chalcogenide QDs tend to have the best quantum yield, with the PL gradually moving towards longer wavelengths with time followed by a sudden drop in QY after about two weeks. [92] This effect has been known to be more rapid during after heating the nanocrystals, with the efficiency dropping within minutes at 100 ºC. [92] This sudden drop in efficiency is a genuine concern for the long term stability and use of these materials in various applications.

One possible way of overcoming this issue is by capping the nanocrystal surface with a higher bandgap inorganic layer. A wider bandgap shell has the potential to provide the passivation of active surface states of the core nanocrystal, eliminating any surface degradation which can result in unwanted non-radiative recombination. [181] Nanoparticles with core-shell structures are known to have enhanced radiative recombination with higher

QY and PL levels in comparison to their bare organically passivated core. Hence by adding a shell, a much more stable material with higher tolerance is formed where the ageing process is significantly reduced. Examples of various core/shell structures include HgTe/CdS [92], HgTe/CdTe [182], CdSe/HgSe [181], CdSe/HgS [49] and CdSe/ZnS [183] with reports of quantum yields of up to 98% for CdSe/ZnS materials, depending on the ZnS shell thickness. [184]

The next chapter will look at the development of HgTe QDs using a modified methodology to the HgSe nanoparticles synthesised in this chapter and presents the addition of some necessary adjustments that were required as a means to encourage the nucleation process between the mercury base solution and tellurium precursor. This was implemented by introducing a form of ionic liquid and further reduction agents to the synthesis process. The structure of the new HgTe QDs will be studied and compared to the HgSe nanoparticles in this chapter, using TEM and HRTEM images including XRD analysis.

Chapter 3:

Synthesis of HgTe Quantum Dots

3.1 Introduction:

The production of high-quality semiconductor nanoparticles has been significantly growing in demand due to the increase in their applications within the field of fluorescent labelling, photovoltaic and light-emitting devices. [185]

Similar to HgSe, as a bulk material HgTe exists as a semimetal exhibiting a negative bandgap of -0.15eV. [119] By forming this material into small nanosized particles, quantum confinement can occur, resulting in the widening of the bandgap. This may cause the material to exhibit properties of a narrow bandgap semiconductor with optical properties in the near-infrared (NIR) wavelengths.

HgTe quantum dots are one of the more popular types of mercury chalcogenide nanoparticles with potential applications in the optoelectronic industry. [119] The growing interest in these types of nanomaterial can be linked to their ability to be synthesised in room temperature, taking into consideration that colloidal HgTe quantum dots are also being investigated for infrared applications such as photodetectors, photovoltaics and light emission in the NIR and mid-infrared range as described previously. [140] The initial strategies for the development of HgTe nanocrystals exhibited problems, mainly due to the rapid growth of the particles after nucleation. This is known to be caused by the highly reactive nature of the mercury precursor in the reaction and has been reported in various investigations. [12] [128] However, as a means to produce monodispersed samples, it is preferable to control the growth rate during the synthesis process. As mercury chalcogenide QDs are highly reactive at room temperature, the morphology of the particles can potentially be tuned. This was observed in the previous chapter for the HgSe QDs and the differences in bandgaps were clearly shown.

By using liquid nitrogen to control the particle growth during synthesis, better monodispersity was achieved. This monodispersity was observed in the TEM images in

Figure 2.3, which showed a narrow size distribution with an average particle size of 14 nm ± 2 nm. Improved optical properties were also obtained from these samples, indicating that the freezing process could potentially increase nucleation without the risk of rapid particle growth during the reaction. Hence, due to the success of this process with HgSe, it was applied in the preparation of monodisperse HgTe.

Synthesising high-quality telluride nanocrystals requires the preparation of a soluble tellurium precursor, which has presented a considerable challenge. [123] Trioctylphosphine (TOP) has commonly been used to achieve this, hence the majority of HgTe reactions consist of a TOPTe precursor combining with a Hg precursor, normally a salt, resulting in HgTe nanoparticles capped by trioctylphosphine oxide (TOPO) as a passivating agent. This results in the formation of long TOPO-capped nanoparticles with the capability of being redispersed in organic solvents, such as hexane or toluene. Despite the success of TOPO as a protecting surface capping agent, the surfactant TOPO has been known to exhibit remedial effects in biological systems, hence it has been identified as a toxic material. [186] This factor is critical for nanoparticles that could have the potential to be used in biological imaging and diagnostics, motivating the consideration of alternative synthesis pathways.

In the past decade, work has been carried out to synthesise semiconductor nanocrystals without the use of organometallic precursors. [185] However, the elimination of phosphines as a coordinating solvent has been challenging within the synthesis process. This chapter will look at a synthetic method for high-quality HgTe colloidal nanoparticles, eliminating the use of TOP and hence providing an alternative and less toxic method to produce these nanocrystals. The introduced method will use ideas put forward in the previous chapter for synthesising HgSe quantum dots in an oleic acid surfactant and introduces further modifications that allow a successful reaction between the tellurium (Te) precursor and the Hg base solution. The use of oleic acid as a surfactant is significant since it is naturally

present in olive oil with substantially lower toxicity levels than TOPO. Oleic acid has long alkyl chains that passivate the nanoparticles. This provides a suitable alternative for TOPO to be eliminated from the reaction process. Furthermore, the synthesis of HgSe nanoparticles without the use of TOP is a significant step forward towards the production of phosphine-free selenide nanocrystals. This is mainly due to selenium powder being able to dissolve in octadecene (ODE) at high temperatures without the need for any additional reducing agents. In the case of tellurium, the metallicity is much stronger when compared with Se. This raises a challenge for creating a stable Te precursor using only ODE. Thus, modifications need to be made to the previous method as a means to support a stable reaction. [123]

The entirely phosphine free synthesis of HgTe nanocrystals is still very challenging, however. Due to their unique and excellent photovoltaic and thermoelectric performances, telluride nanoparticles are highly desirable materials which is the main motivation to find cheaper, less toxic and safer approaches for obtaining high-quality HgTe nanocrystals.

In the past few years, ionic liquids have been used for preparing a variety of nanoparticles such as aluminum antimonide [187], metal fluorides [188] and cobalt platinum alloys [189]. The use of phosphonium ionic liquid as a replacement for TOPO has also been demonstrated in the synthesis of CdSe and CdTe nanocrystals. [186] [190] In this case, the synthetic pathways benefit from having the capability to bind to both anionic (Te) and cationic (Hg/Cd) surfaces whilst remaining soluble in organic solvents and potentially providing a better, more defined surface passivation around the nanoparticles.

The alternative approach implemented in this chapter introduces sodium borohydride ($NaBH_4$) as a reducing agent for tellurium, combined with an ionic liquid, trihexyltetradecylphosphonium bis(2,4,4-trimethylpentyl)phosphinate and ODE to form the necessary tellurium precursor. The ionic liquid used is a phosphonium phosphinate and is used as a polar solvent to assist with the tellurium transition after it has been reduced by the

sodium borohydride ($NaBH_4$) as shown in Equation 3.1. The formed precursor will be combined with the mercury and oleic acid surfactant, as a means to form high-quality HgTe nanocrystals at room temperature. Similar to the HgSe reaction, liquid nitrogen will be used to control particle growth and encourage nucleation.

$$Te + 2NaBH_4 \rightarrow Na^+{}_2Te^{2-} + 2BH_3 + H_2 \quad \textbf{(3. 1)}$$

Certain ionic liquids (which possess long alkyl chains) exhibit desirable similarities with existing capping agents, such as commercial availability, thermal stability at elevated temperatures, long alkyl chains, and functional groups allowing coordination with the particle's surface. Trihexyl tetradecyl phosphonium phosphinate is a suitable candidate to be used as a surfactant for nanoparticle synthesis. However, in this case, as oleic acid is the main surfactant used to pacify the nanocrystal surface, the ionic liquid $[P(R)_3(R')]^{1+}$ $[P(R'')]^{1-}$ will be primarily used to bond with Te^{2-} to form the required tellurium precursor represented in Equation 3.2.

$$Na_2Te + 2[P(R)_3(R')][P(R'')] \rightarrow 2Na[P(R'')] + Te[P(R)_3(R')]_2 \quad \textbf{(3. 2)}$$

$R = C_6H_{13}$ $\quad R' = C_{14}H_{29}$ $\quad R'' = C_{16}H_{34}O_2$

3.2 Synthetic methodology:

Similar to the synthesis of HgSe QDs explained in the previous chapter, mercury acetate $Hg(O_2CCH_3)_2$ was combined with oleic acid (OA) $C_{18}H_{33}O(OH)$ at 90°C heat under nitrogen to form the mercury precursor solution. As shown in Equation 3.3, the mercury (Hg) combines with the OA to form mercury oleate $Hg[C_{18}H_{33}O_2]_2$ with acetic acid $CH_3CO(OH)$ as a by-product. For this reason, the solution was kept under vacuum for two hours to prevent the excess build-up of acetic acid.

$$Hg(O_2CCH_3)_2 + C_{18}H_{33}O(OH) \rightarrow Hg^{2+}[C_{18}H_{33}O_2]^{2-}{}_2 + [CH_3CO(OH)]_2 \quad \textbf{(3. 3)}$$

The trihexyl tetradecyl phosphonium phosphinate ionic liquid was reacted with Te, sodium borohydride and ODE under consistent heat to form the main precursor. The reduction process of Te (Equation 3.2) could be identified by observing the solution changing colour from clear to dark purple. It should be noted that without heating the ionic liquid, this process could not take place and the tellurium did not react with the ionic liquid. It is also worth adding that the reaction between the ionic liquid and Te should be kept under nitrogen as any exposure to air prevented the precursor from forming, causing the tellurium to precipitate out of the solution. This failure could be seen as a colour change from purple to green. In the event of this happening, the solution could be exposed to a vacuum and reheated under nitrogen to reform the desired precursor, suggesting a reversible reaction.

After both solutions containing Hg and Te precursors have been cooled to room temperature, the Te precursor was injected into the mercury precursor solution under nitrogen and rapidly cooled using liquid nitrogen to prevent aggressive growth, as observed for the HgSe nanocrystals. The final solution was formed after the reaction was allowed to gradually reach room temperature over an 8-hour period and the colour of the solution turned to black. By referring to reported HgSe reaction representations [12] and applying it to this synthesis, the reaction mechanism can be represented using Equation 3.4, showing the formation of the HgTe nanocrystals after the combination of the Hg and Te precursors.

$$Te[P(R)_3(R')]_2 + HgX_2 \rightarrow HgTe + 2X + 2[P(R)_3(R')] \quad \textbf{(3. 4)}$$

$R = C_6H_{13}$ $R' = C_{14}H_{29}$ $X = C_{18}H_{33}O_2$

By implementing size-selective purification using acetone and filtering the solution, the obtained HgTe nanocrystals were dissolved in an organic solvent such as toluene. The size-selective precipitation allows the separation of smaller nanoparticles from their larger counterparts by adding acetone in small increments in the purification process before distributing the precipitates in organic solvent and this will be explained in more detail in Chapter 5. It is worth noting that if the purified nanocrystals did not dissolve in the organic solvent, then this indicated a failed reaction which is typically caused by an unsuccessful reduction of tellurium within the ionic liquid and ODE. This was understood to be caused by aged $NaBH_4$, which play a critical role in reducing the tellurium within the precursor solution.

3.3 Structural analysis

Particle monodispersity is very important when synthesising quantum dots. The size tuning capabilities of nanoparticles correlates to the distribution range of their optical wavelengths. Hence, poorly dispersed samples would result in wider emission peaks and lower quantum efficiency due to a large particles distribution rate, absorbing light at a longer wavelength range.

The HgTe samples synthesised in this chapter have been capped by long-chained oleic acid (and possibly the ionic liquid) and dispersed in toluene after purification. The growth rate was controlled by rapidly lowering the reaction temperature using liquid nitrogen, allowing the particles to naturally reach room temperature over time. The initial transmission electron microscope (TEM) images in Figure 3.1 show the HgTe particles with good monodispersity and an average particle diameter of 5 nm ± 0.7 nm. The images show various magnification of the same sample whereas, in Figure 3.1D, an individual particle with some lattice structure visibility is observed. HgTe nanoparticles are known to vary in

size from 3 nm to about 12 nm, depending on their reaction method and growth rate. [191] The observed aggregation within the samples, shown in Figure 3.1A,C, is most likely due to a poorly passivated surface caused by rapid growth. This could also be caused by the long-chained ionic liquid within the Te precursor interacting with the oleic acid ligands. Similar structures have been reported in other HgTe investigations [192] with particle aggregation being linked to the synthesis scheme and the fast nucleation of II-VI materials, resulting in some bulk structures. [119]

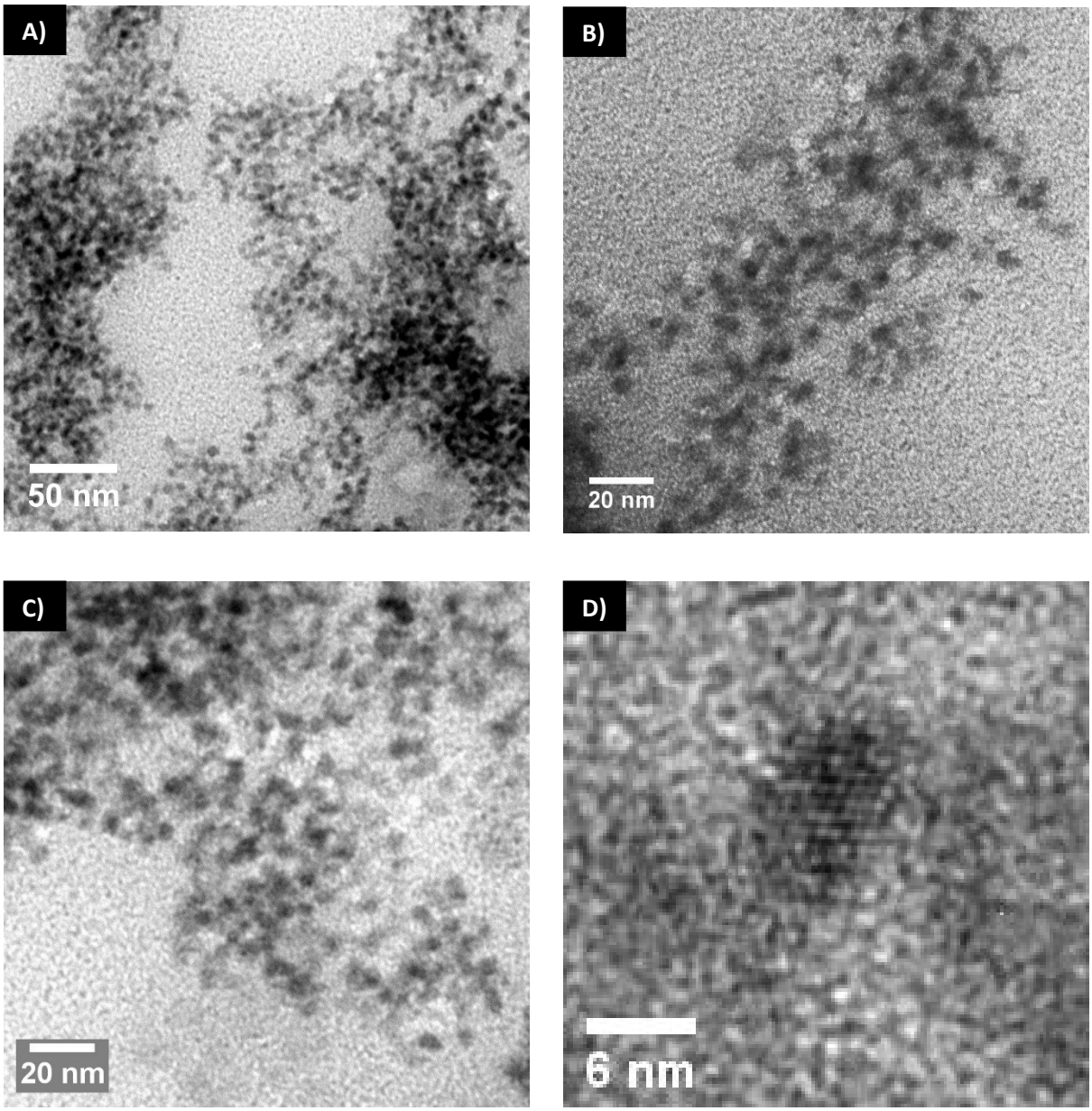

Figure 3. 1 - TEM images of HgTe nanoparticles synthesised at room temperature with injection/freezing - A) Low magnification image. Scale bars = 50 nm; B) Standard magnification. Scale bars = 20 nm; C) Standard magnification with some visible aggregation. Scale bars = 20 nm; D) Individual particle view. Scale bars = 6 nm.

In the case of photodetectors and IR devices, nanoparticle aggregation is encouraged and very beneficial as it provides natural electronic coupling between the particles, reducing the barrier width between them. [11] Ligand exchange within a quantum dot film is essential for achieving conductivity between the particles as they are prepared using drop casting

techniques. [131] Therefore, these types of aggregated HgTe quantum dots are readily conductive without the need for any further treatment, which could become a critical cost saving factor. In some instances, HgTe quantum dots are capped with shorter dithiol molecules, such as ethanedithiol (EDT), using solid-state ligand exchange, to improve photoconductivity between the particles without significantly compromising their colloidal stability. [193]

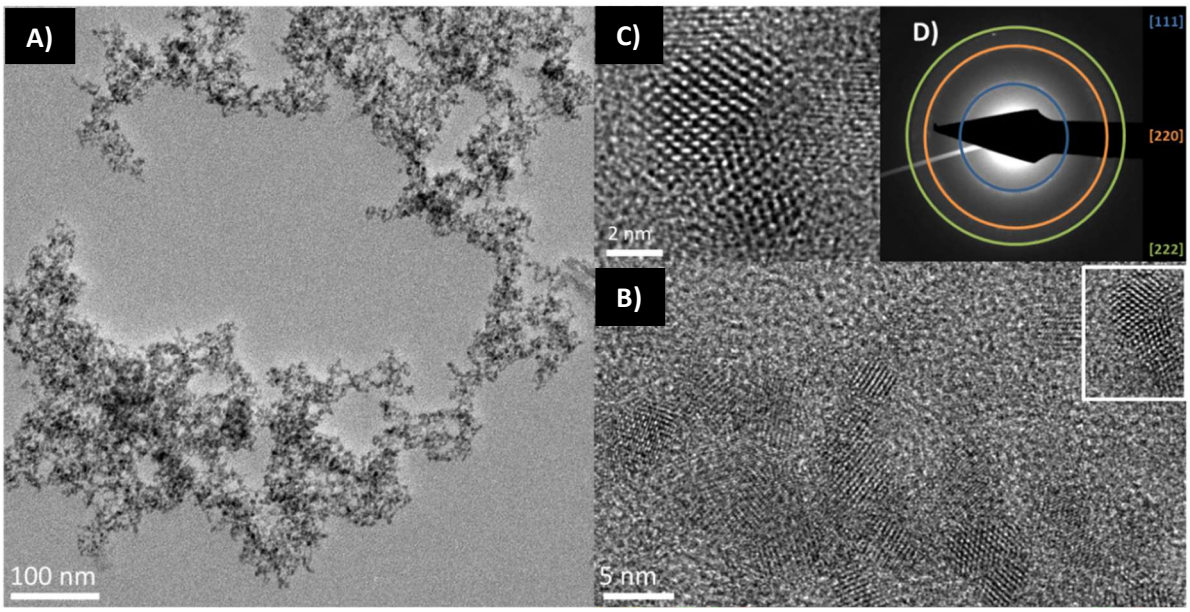

Figure 3. 2 – HRTEM images of HgTe samples synthesised at room temperature with injection/freezing - A) Low magnification image of QDs. Scale bars = 100 nm; B) image of QD showing highly crystalline. Scale bars = 5 nm; C) image of individual QD shown in B. Scale bars = 2 nm.

The high-resolution images (HRTEM) in Figure 3.2A,B show the samples with a clear lattice plane visible in Figure 2C, indicating high crystallinity and analogous to the HgSe nanoparticles previously observed. Similar lattice fringes have been observed in other investigations which support this crystalline structure. [194] The measured XRD pattern shown in Figure 3.3 supports the HgTe crystalline formation with three diffraction peaks

detected to correspond with 111, 220 and 311 planes of zinc-blend phase. This coincides with other reports of HgTe nanocrystals and confirms their cubic zinc blend structure. [92] [194] It is also worth mentioning, similar to the HgSe XRD pattern (Figure 2.7) in Chapter 2, the reflection at *ca.* 20 °2Θ was due to the glass slide used to hold the sample. Furthermore, the small spike at *ca.* 30 °2Θ was attributed to impurities present within the sample and can be corrected with additional purification.

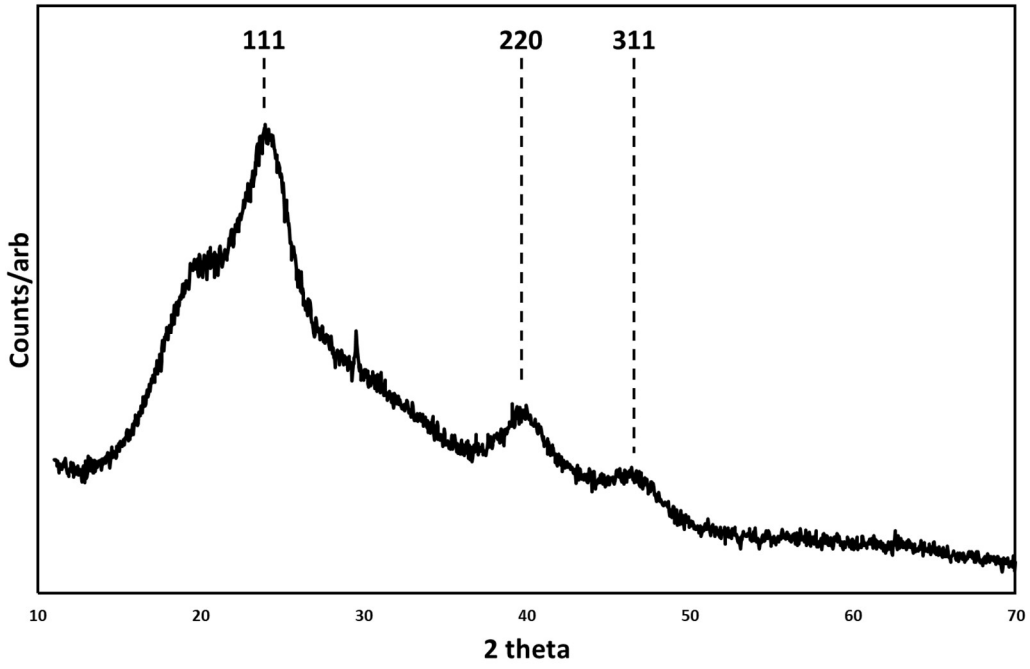

Figure 3. 3 - X-ray diffraction pattern (XRD) of zinc blende HgTe particles prepared at room temperature and associated Miller indices.

By using scanning transmission electron microscope (STEM) and energy dispersive X-ray analyser (EDX) imaging shown in Figure 3.4, the elemental identification and quantitative compositional information were analysed. This calculated a distribution of the Hg and Te to be *ca.* 48.59% and *ca.* 51.41% respectively. The even distribution within the sample is a clear indication of the successful bonding between Te and Hg after nucleation, from injecting the precursor into the base solution, resulting in the observed crystal structure.

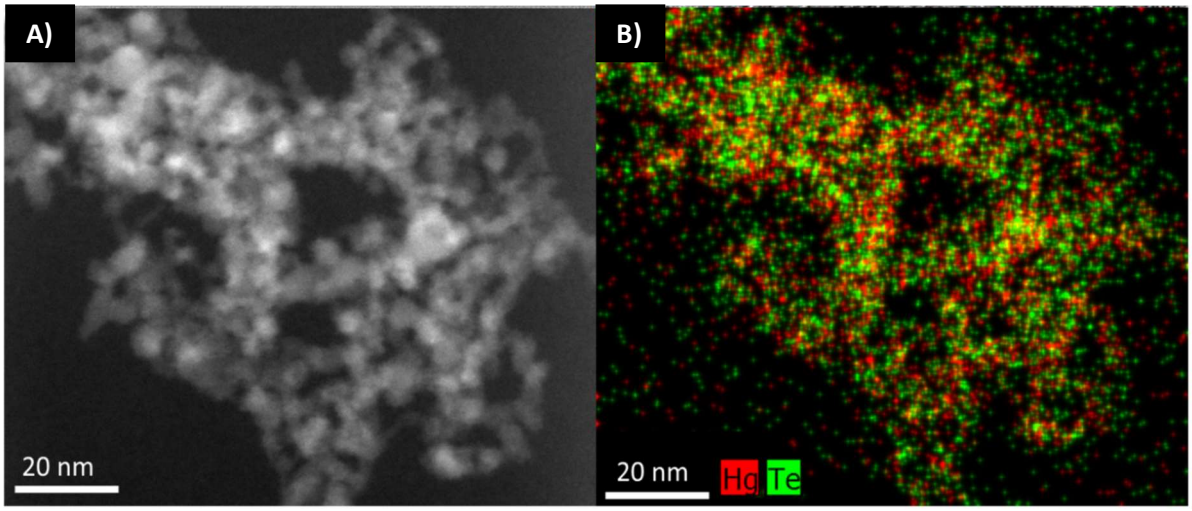

Figure 3. 4 - STEM A) High-angle annular dark-field imaging (HAADF) STEM image of QDs. Scale bars 20 nm; B) STEM-EDX elemental map showing even distributions of Hg and Te. Scale bars = 20 nm.

3.4 Optical analysis

As previously stated, the growth process of HgTe nanoparticles is rapid, thus at room temperature aggressive growth could take place. The sudden temperature reduction using liquid nitrogen is a way to help prevent this from occurring, resulting in nucleation after precursor injection, followed by immediate quenching. The slow warming of the solution to room temperature resulted in the slow growth of the nuclei to nanoparticles.

The initial optical absorption and emission data for the HgTe quantum dot samples are shown in Figure 3.5. This was taken after the samples were purified using size-selective precipitation and dispersed in toluene. Both absorption spectra (Figure 3.5a,b) are from the same samples with different concentration, hence the increase in their maxima.

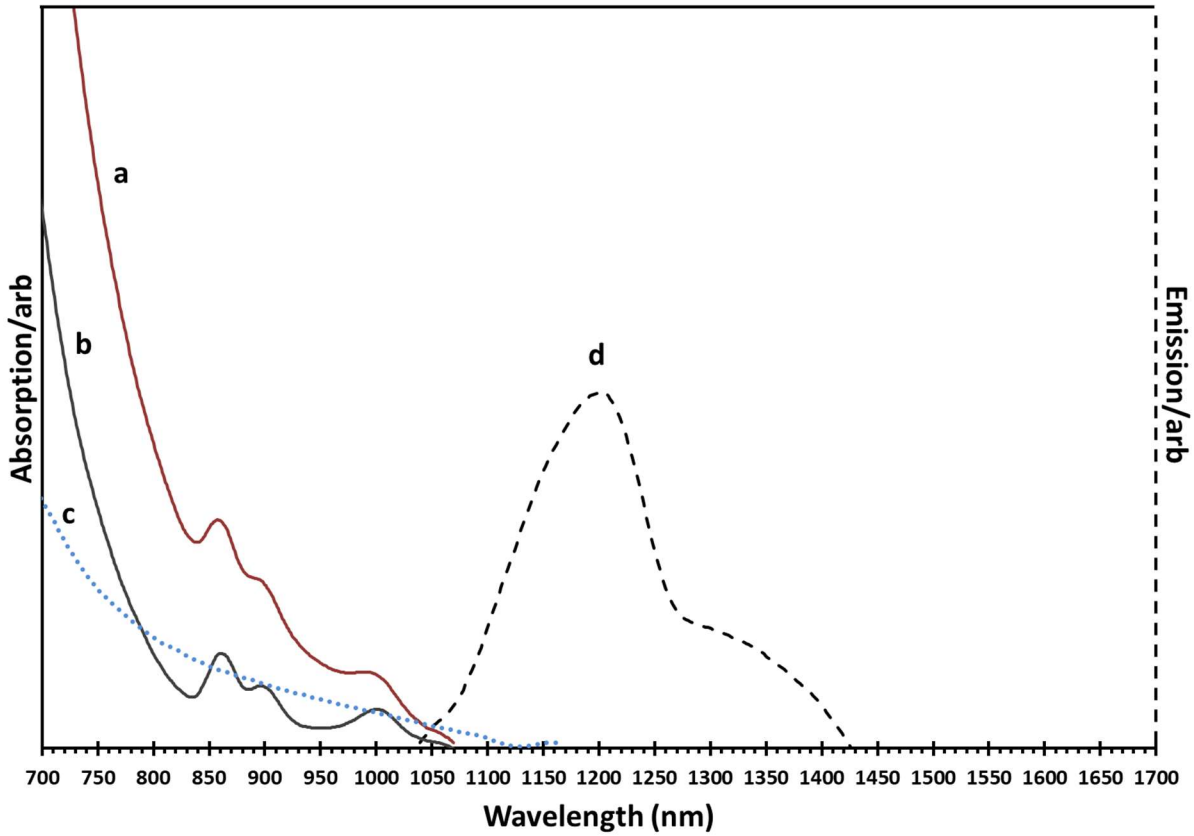

Figure 3. 5 - Absorption and emission spectra of HgTe nanoparticles synthesised at room temperature injection/freezing - a) absorption spectra for high concentrated sample; b) absorption spectra for normal concentration sample; c) sample tested after one-week; d) emission from normal concentrated sample.

An interesting observation is the presence of multiple excitonic features at *ca.* 860nm (1.44 eV), *ca.* 900nm (1.38 eV) and *ca.* 1000nm (1.24 eV). This could be caused by various factors. The obvious explanation would be the emergence of multiple quantum-confined energy levels, as observed in other QD systems when particles are below the excitonic diameter. Other explanations include the possibility of a wide range of multiple sized HgTe nanoparticles within the sample examined, each presenting a different absorption feature. Rapid particle growth could have been initiated before liquid nitrogen was introduced to the system, quenching the growth process. This could result in the particles forming of different sizes and effecting the monodispersity of the sample However, this is unlikely as size-

selective precipitation was used to purify the HgTe samples after reaction completion. As this technique is used to separate smaller particles from larger one, the emergence of multiple absorption peaks from one sample is likely due to an inherent optoelectronic feature of the resulting nanoparticles, or possibly absorption features in the ionic liquid which had not been sufficiently removed.

The same sample was retested after a week, resulting in a noticeable disappearance of all exciton features as shown in Figure 3.5c. This was expected, as HgTe samples are known to oxidise and precipitate out of the organic solvent after several days. [119] The emission spectra shown in Figure 3.5d were shifted from the band edge with a maxima at *ca.* 1200nm (1.03 eV) and a FWHM of *ca.* 145nm. The PL also showed an interesting feature at *ca.* 1260 (0.98 eV) as the spectrum became broader. This could be caused by the size variation within the samples. The emission quantum yield was calculated using the integrating sphere [35] method and was approximately 5%.

Samples synthesised using the same method (a rapid temperature reduction by means of liquid nitrogen straight after the precursor injection) without using the size-selective technique had optical properties as shown in Figure 3.6, provide a single excitonic feature at *ca.* 800nm (1.55 eV) with an onset absorption at *ca.* 1150nm (1.08 eV). The emission spectra, again Stokes shifted from the excitonic feature, has a maxima at *ca.* 1150nm (1.08 eV) with a higher FWHM of *ca.* 276nm, when compared to the size selected samples. However, it is noted that the PL spectra is similar to samples shown in Figure 3.5d, taking into consideration some size variation between the particles. The quantum yield for this HgTe samples was calculated to be 9%, higher than the previously tested sample.

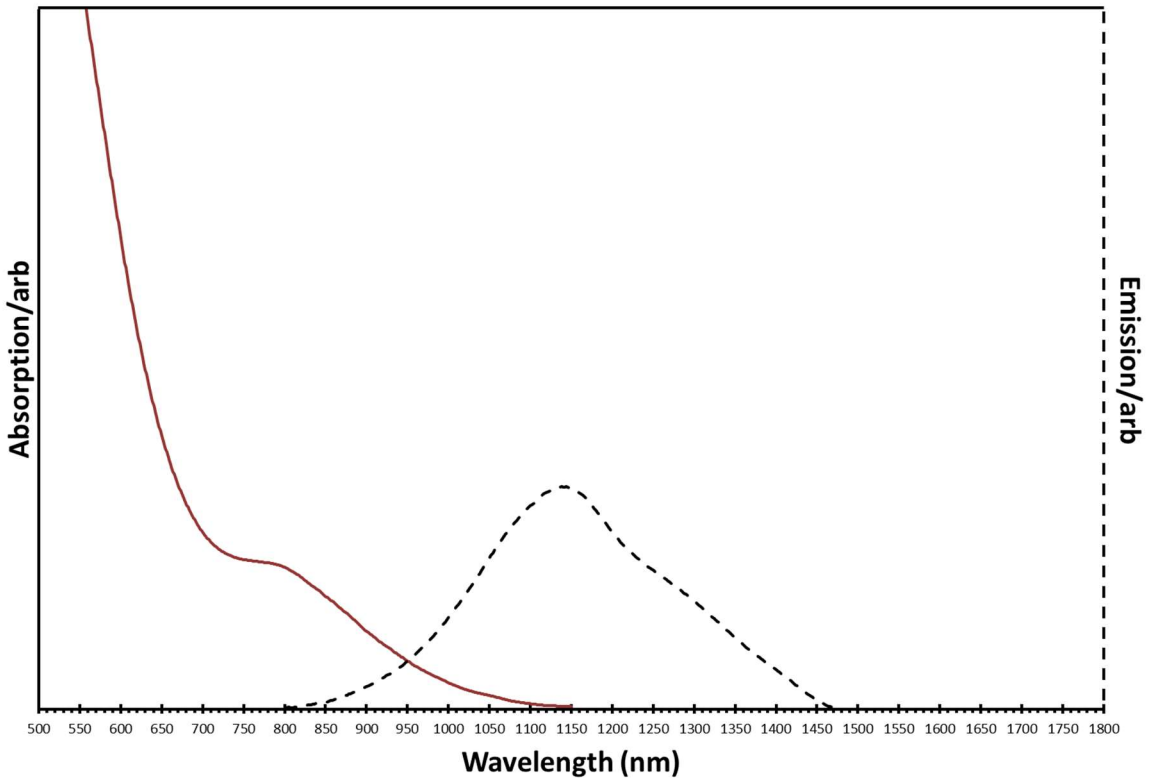

Figure 3. 6 - Absorption and emission spectra of HgTe nanoparticles synthesised at room temperature injection/freezing without size selective purification.

3.5 Conclusion

Taking into consideration the growing popularity of HgTe nanoparticles, in this chapter, a simple synthetic pathway has been introduced that eliminated the used of TOP and TOPO from the reaction pathway. The use of an ionic liquid (trihexyl tetradecyl phosphonium bis(2,4,4-trimethylpentyl)phosphinate) has proven to be effective as a substitute to TOP. Similar to the previous chapter, oleic acid has again been demonstrated as an effective capping agent, passivating the nanoparticle surface and supplying the crystals with ligands as a means to disperse in organic solvents.

The TEM images taken from the HgTe sample indicate particle monodispersity with a narrow size distribution of 5 nm ± 0.7 nm. The HRTEM images show a distinct crystal

lattice structure associated with HgTe nanoparticles. This was confirmed using XRD analysis, which supported the cubic zinc blend structure of the HgTe quantum dots. Further analysis using HAADF and STEM imaging revealed a better understanding of the Hg and Te distribution within the sample, showing an equal spread of both elements in the crystal structure, indicating a successful reaction, complimented by the sudden temperature reduction during the reaction process. Hence, the use of liquid nitrogen to prevent aggressive particle growth has been successful.

The synthesised HgTe nanoparticles exhibited a clear excitonic feature in the absorption spectra and showed a clear Stokes shifted emission peak. Size-selective purification of the particles resulted in the emergence of multiple peaks in the absorption profiles, possibly from size quantisation effects, demonstrated by separating smaller particles from its larger counterparts. These results were supported by the second sample not undergoing the size-selective process, resulting in a single but broader absorption curve with a Stokes shifted emission that consisted of a higher FWHM value. The quantum efficiency of this sample also showed slight improvement; however, this could be linked to the size-selective precipitation process damaging the particle surface by repeated exposure to a solvent system which stripped ligands from the surface, introducing non-radiative recombination pathways.

Overall, the results shown in this chapter provide evidence that HgTe nanoparticles have the potential to be synthesised using cheaper and less toxic routes with similar resulting morphologies and optical properties that provide acceptable quantum efficiencies. Further developments could include deposition of a shell around the surface of the quantum dot as a means to improve surface defects before passivation. This core-shell structure of the nanoparticles has been proven to improve their colloidal and optical properties. [195]

The primary focus in the next chapter will be on synthesising HgTe quantum dots in a biological environment, illustrating how these nanoparticles can grow inside living plants. The method of synthesis will be primarily aqueous and will use the plants' natural growth process to support the developments of the HgTe nanocrystals.

Chapter 4:

Biosynthesis of HgTe Nanoparticles

4.1 Introduction:

The emergence of the inert-atmosphere organometallic route to quantum dots described in this thesis is based on a landmark method to make most semiconductors on the nanoscale. [24] The optimisation of reaction conditions allowed the growth of highly structured materials with controllable electronic and optical properties using relatively simple synthesis techniques. Simultaneously, aqueous routes towards colloidal semiconductors emerged yielding high-quality thiol-capped CdTe quantum dots prepared without the need for a further inorganic shell. [59] Both these routes gave highly luminescent nanomaterials in differing solvent and chemical environments.

In the previous two chapters, both HgSe and HgTe nanocrystals were synthesised using inorganic precursors and organic solvents, eliminating the need for TOP and TOPO from the reaction process. This modification substantiated the formation of these colloidal quantum dots at room temperature, using simple reduced toxic routes by controlling the nucleation and growth process. However, the need to further simplify these synthetic pathways (which utilise inert atmospheres and some degree of heating) has led to the emergence of biosynthesis, combining aqueous colloidal chemistry and existing natural biological processes to produce nanostructured solid-state materials. [196] There has been previously reported synthesis of CdTe quantum dots in the chloragogenous cells of a live worm, exploiting a natural reaction known as mutual antagonism to produce the nanomaterials as a by-product against exposure to heavy metals. [197] Mutual antagonism has been known to toxicologists since the 1960s, [198] and has been evoked to explain the formation of inorganic granules in a variety of living animals after exposure to mercury and selenium compounds. [199] Although well-known to toxicologists, few materials scientists are aware of the biological process where two precursors react to form a less-toxic species (which coincidentally happens to be a semiconductor), analogous to numerous reactions in

materials chemistry. In the case of mercury exposure, a large number of metazoans (especially higher trophic marine animals) respond to such a threat by reacting the toxic metal ion with selenium and selenoprotein P, producing tiemannite (HgSe) inorganic granules, thereby locking-in the toxic elements in a relatively non-toxic form. [200] [201]

Mutual antagonism has also been reproduced in plants by the addition of a chalcogen precursor with the toxic metal cation, mimicking the formation of tiemannite granules in large animals [202] [203]. This process has the advantage of being easier to manipulate into a routine synthetic procedure for material synthesis. As mentioned in the earlier chapters, whilst HgSe is a known narrow bandgap semiconductor, the optical properties are inferior to the related HgTe in quantum dot form [9], notably when capped with a thiol species, in a similar manner to CdTe previously explained. [59]

In this chapter, the first direct production of technologically relevant infra-red emitting semiconductor HgTe quantum dots will be demonstrated, via mutual antagonism in living plants. Exposure of common *Allium fistulosum* to mercury and tellurium salts under ambient conditions resulted in the expulsion of crystalline, non-passivated HgTe quantum dots that exhibited emissive characteristics in the near-infrared spectral region, a wavelength range that is important in telecommunications and solar energy conversion.

4.2 Synthesis methodology:

In a typical reaction, *Allium fistulosum* (common spring onion) were obtained from commercial sources and grown for a further month in deionised water and ambient conditions. To one of the plant's growth solutions, equimolar amounts of $Hg(O_2CCH_3)_2$ and Na_2TeO_3 were added in water. The plants were then allowed to grow for a further seven days at which point the plants were removed from the growth solution. The roots of the plant which had been exposed to the precursors had a black coating, unlike control samples which showed no evidence of solid-state material growth (Figure 4.1). The black material could then be mechanically removed using a spatula, and dispersed in water with sonication, forming a suspension, or left *in situ* on the plant root. It should be noted, as these nanoparticles have not been capped with thiols, they would not be able to dissolve in organic solvents on their own.

Figure 4. 1 - Photo of *Allium Fistulosum* roots; A) Root growth control with no exposure to precursors; B) Root after 7 days exposure to precursors.

4.3 Structural analysis:

Electron microscopy of the dispersed samples showed polydispersed nanoparticles, up to 20 nm in diameter (Figure 4.2A). High-resolution transmission electron microscopy (HRTEM) again showed discrete non-spherical, single crystal particles with distinct facets (Figure 4.2B) and the Fourier transform confirmed the expected reflections consistent with HgTe oriented along the [001] zone axis (Figure 4.2C). The non-spherical shape of these nanoparticles agrees with the HgTe samples reported in chapter 3, in addition to other reports of Hg chalcogenide quantum dots, where a variety of morphologies is routinely reported by varying the synthesis temperature, which is usually significantly lower than other II-VI semiconductors. This has been attributed to the positive redox potential for Hg^{2+}, which makes the reduction step of the group II precursor favourable. [12]

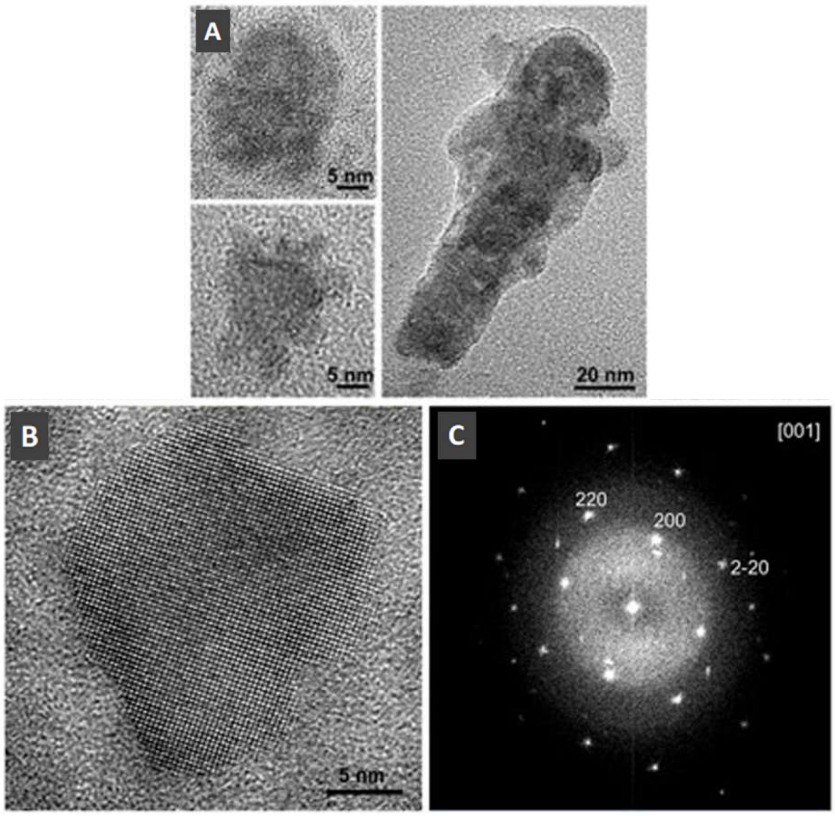

Figure 4. 2 - (A) A selection of transmission electron microscope images of HgTe particles removed from plant root, (B) High resolution transmission electron microscope image of a HgTe nanocrystal, (C) Fourier transform of the image in (B) showing reflections consistent with HgTe oriented along the [001] zone axis.

Atomic resolution high-angle annular dark-field (HAADF) scanning transmission electron microscopy (STEM) of the sample showed non-spherical, single crystal particles with multiple twinning planes, the identity of which again was confirmed by indexing the measured d-spacings to the lattice spacings of mercury telluride (HgTe) (Figure 4.3).

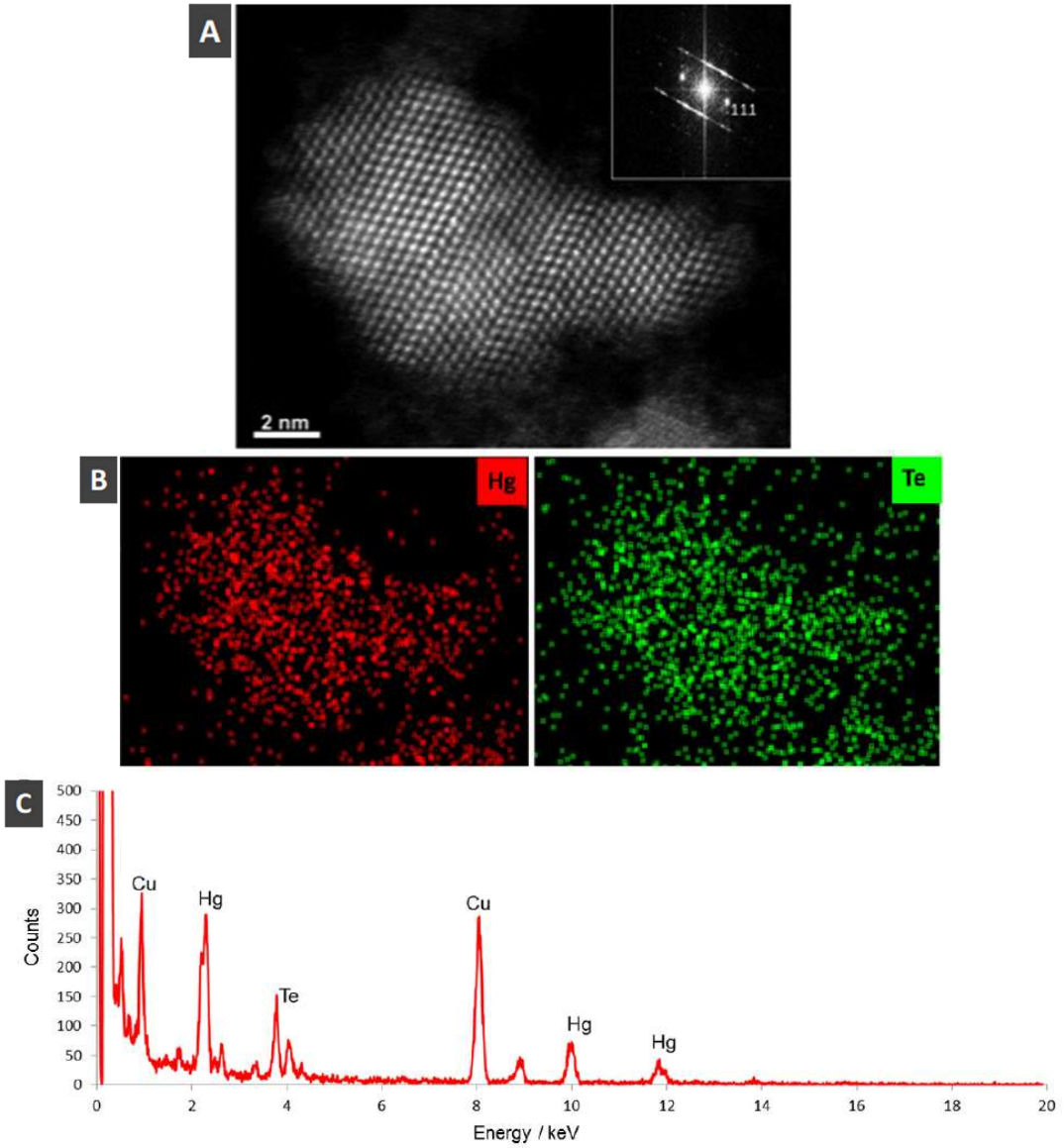

Figure 4. 3 - (A) Atomic resolution high angle annular dark field (HAADF) scanning transmission electron microscope (STEM) image of a single highly twinned HgTe quantum dot. Inset; Fourier transforms of the images clearly showing {111} planes of HgTe. (B) EDX spectrum images of HgTe nanocrystal in the area in (A) showing colocalisation of Hg and Te. (C) EDX spectra extracted from the full spectrum image in (B), EDX quantification reveals a close to stoichiometric composition for HgTe.

In some cases, several crystals approximately 5 nm in diameter appeared to have aggregated, consistent with materials with no surface capping agents (Figure 4.4). Energy-dispersive X-ray spectroscopy (EDXS) analysis of individual particles showed the presence of mainly Hg and Te in ratios of approximately 1:1, surprisingly with no associated carbon or sulfur (Figure 4.4C) which suggested the absence of a surface passivating ligand.

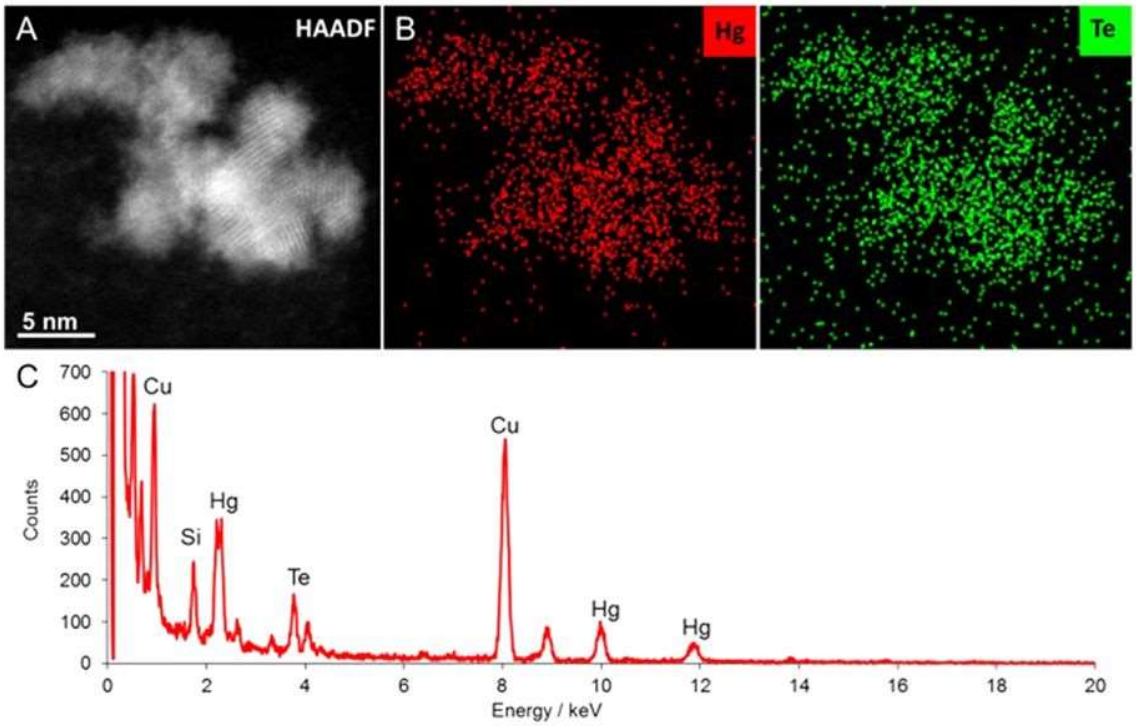

Figure 4. 4 - (A) High angle annular dark field scanning transmission electron microscope images of HgTe quantum dots. (B) Energy dispersive X-ray (EDX) spectrum image of area in (A) showing colocalisation of Hg and Te. (C) EDX spectra extracted from the full spectrum image in (B), EDX quantification reveals a close to stoichiometric composition for HgTe (48 at. % Hg:52 at. % Te).

This is unlike the previously reported CdTe biosynthesis which showed evidence of a small-molecule thiol-based capping agent. [197] The presence of a thiol capping agent is beneficial in some nanoscale semiconductors, notably CdTe and HgTe, where the coordinating functional group is the basis for the observed enhanced emission due to the alignment of energy levels of both the surface ligand and semiconductor leading to blocked

hole trapping states. [58] [204] Whilst a surface capping layer is essential for specific applications such as biological imaging, it does, however, present a potential barrier for charge carriers. As explained in the previous chapter, other applications, such as solar energy conversion, would benefit from the absence of a passivating layer to remove any obstacle to charge carrier separation, or to provide a clean surface to attach a specifically engineered ligand. [205]

4.4 Biosynthesis reaction process:

An electron microscope investigation into the biological processes in the plant with regards to where the reactions occurred was also conducted (Figure 4.5). The *Allium* root was examined after 7 days exposure to the precursors, specifically the sections localised through the apical meristem, the elongation zone and the basal zone just beneath the bulb crown where the roots looked particularly blackened. Inclusions were primarily observed in the cortex at the division zones near the meristem. In the sections within the elongation zone, the inclusions appeared to be mainly inside the large central vacuole of the cortical cells. The presence of inorganic inclusions was also observed on the cell wall of the roots in sections near the crown. EDXS analysis of the inclusions identified Hg although Te was only marginally detected in contrast to the analysis of the particles dispersed in the solution described above. This was explained by the presence of uranium peaks, associated with the uranyl acetate stain introduced during processing to enhance the TEM image contrast, which overlapped with the tellurium signal.

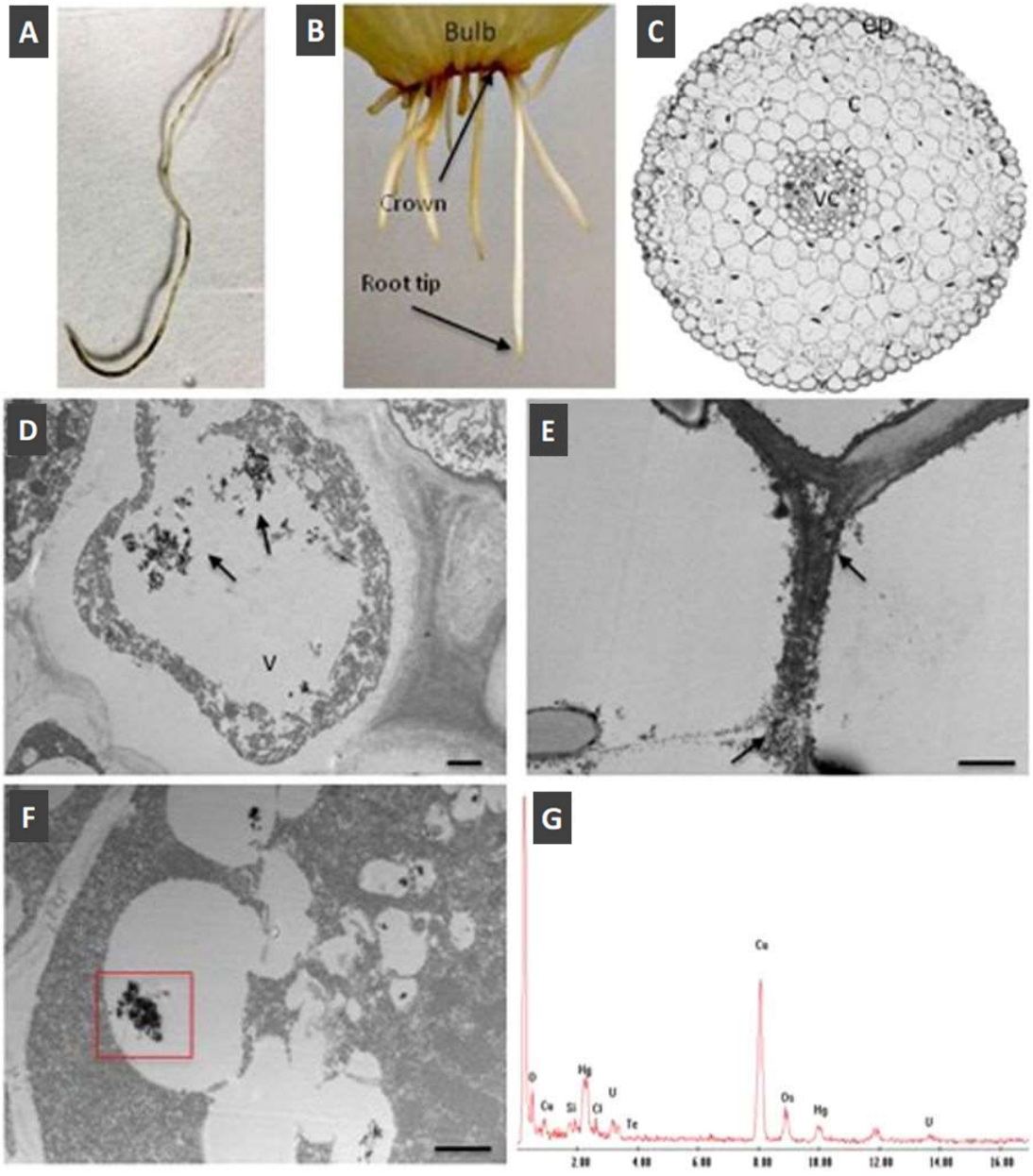

Figure 4. 5 - Hg/Te inclusion localization within the root tissues. (A) Representative image of a root exposed to Hg/Te salts. Blackened areas are observed all along the root, being more pronounced near the root tip and at the basal zone of the root; (B) Samples were collected near the root tip and just below the bulb crown; (C). Cross-section of main root of *Allium Fistulosum*; epidermis (ep), cortex (c) and vascular cylinder (vc); (D,E) Electron micrograph showing inclusions (arrows) in the central vacuole (v) of a cortical cell in D and within the cell wall in (E–G) Aggregates accumulate in the vacuole (red box in (F) were analysed by EDXS to confirm the presence of Hg and Te as shown in the spectrum (G). All scale bars:1 μm.

Whilst the reaction is based upon the aqueous route with regards to the choice of target material and precursors, this synthesis is notably different and can be considered a 'green' alternative for a number of reasons; the actual mechanism suggested here (mutual antagonism) is a natural process that has evolved in plants and animals to specifically reduce the impact of heavy metals. No organic solvents, capping agents or extraneous precursors were utilised unlike bench-based organometallic routes, nor was heating required or the presence of inert gases, all of which require processing and the expenditure of resources. The mechanisms involved in particle formation were clearly driven by the inherent biological processes in the plant, such as the reduction of the Te^{IV} species to Te^{II}, which is essential to form the materials reported. Similar processes have been highlighted in the plant-based reduction of arsenate species to arsenate by enzymes. [206] The exact mechanism behind the formation of HgTe quantum dots is unclear, however, the potential use of phytochemicals within the root could be involved in the reduction of Te and Hg from Na_2TeO_3 and $Hg(O_2CCH_3)_2$. Furthermore, HgSe granules have been noted in the literature, their formation in marine animals have in most cases been linked to selenoprotein P, which is not present in the plant used in this study. Likewise, the mechanism suggested in previous work carried out on CdTe synthesis in earthworms is unlikely to be applicable. [197] Studies by Caruso [202] on the formation of tiemannite in *Allium* highlighted numerous possible mechanisms due to the observation of Hg-Se, Hg-only and Se-only regions in the plant, with the conversion of Na_2SeO_3 to methylselenocysteine being a predominant reaction in the reduction of selenium toxicity. Whilst there are few reports on tellurium metabolites in plants, *Te*-methyltellurocysteine oxide has been observed as the major metabolic species from the exposure of *Allium sativum* to Na_2TeO_4. *Te*-methyltellurocysteine oxide was further reported to degrade to either methyltellurol or methyltellurous acid, which was then sequestered by cysteine giving *S*-methyltellurylsulfide. [207] Assuming a similar reaction in *Allium*

fistulosum, which of these metabolites is the actual tellurium precursor is at present unknown although methyltellurol has previously been reported as a precursor in the preparation of CdTe and HgCdTe thin films by chemical vapour deposition. [208] It is also worthy to note that alkyltellurols (RTeH; R = alkyl) have been shown to react with group II metal species to give the family of compound $M(TeR)_2$ (M = Cd, Hg, Zn; R = alkyl group), of which $Hg(TeBu)_2$ has been shown to be an effective room-temperature, photolytic precursor to HgTe nanoparticles. [209]

4.5 Optical characteristics

As a means to determine the quantum confinement effects, the optical properties of the particles were examined. Previously reports have shown, thiol-capped HgTe prepared by aqueous routes under an inert atmosphere have displayed broad, strong emission in the near-infrared region, between 800–1400 nm [58], with the onset of absorption appearing slightly blue-shifted to the emission maxima, usually without a well-defined excitonic peak. This was demonstrated in the work carried out in Chapter 2 which presented HgTe quantum dots with emission readings at *ca.* 1150 nm and *ca.* 1200 nm. In the work reported here, both the solution (deionised water) of dispersed particles and the roots were examined (which included the biosynthesised particles themselves). The absorption of the HgTe solution reported here showed a broad near-infrared band edge containing a feature consistent with an excitonic peak at *ca.* 1140 nm (Figure 4.6a) that was clearly resolved in the derivative spectra. When the solution was excited (λexc. = 812 nm), broad near-IR emission was observed (Figure 4.6b) extending from *ca.* 1000–1375 nm. The reduction in emission intensity at *ca.* 1175 nm and the lack of any measurable emission beyond ~1375 nm is a result of the strong absorption of the emission by the aqueous solution. Similar multi-featured emission spectra have been observed previously and are common for HgTe prepared

in aqueous solution. [192] The emission reported here was substantially weaker than the thiol-capped HgTe nanoparticles prepared in solution (quantum yield below 1%), however, this is unsurprising due to the absence of a thiolated capping agent, whilst the observation of any emission from an uncapped HgTe quantum dot prepared in air is in itself very rare and remarkable.

Photoluminescence from the solid nanoparticles still attached to the root (Figure 4.7) was also observed after direct excitation at 812 nm, thus providing the emission of the HgTe quantum dots in the absence of water absorption. This reveals the full spectral range of the emission obtained from the HgTe quantum dots (~900 nm to 1675 nm), which significantly included the wavelengths of technological importance to telecommunications (Figure 4.6b). The higher energy emission (below 1000 nm) in these spectra originated from the laser diode excitation source as did the narrow peak at 1624 nm (second-order grating diffraction of the source).

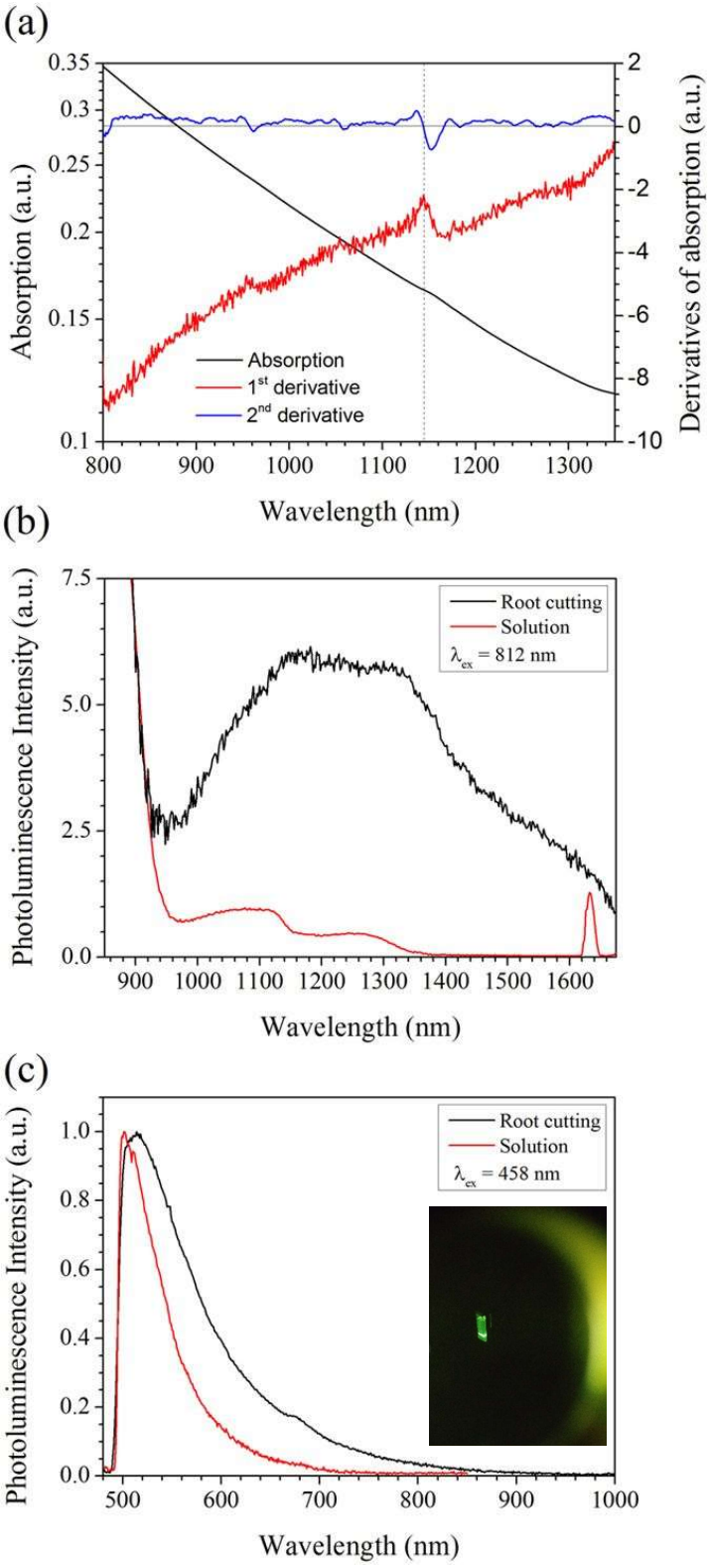

Figure 4.12 - Optical properties of biosynthesised particles. (a) Absorption spectrum of an aqueous suspension of HgTe and derivative spectra resolving an excitonic absorption peak at 1140 nm. (b) Photoluminescence spectra of an aqueous suspension of HgTe and a root cutting containing solid HgTe product excited at 812 nm revealing broad near-infrared emission. (c) Photoluminescence spectra of an aqueous suspension of HgTe and a rout cutting containing solid HgTe product excited at 458 nm displaying strong green emission attributed to chlorophyll (sample shown on the right).

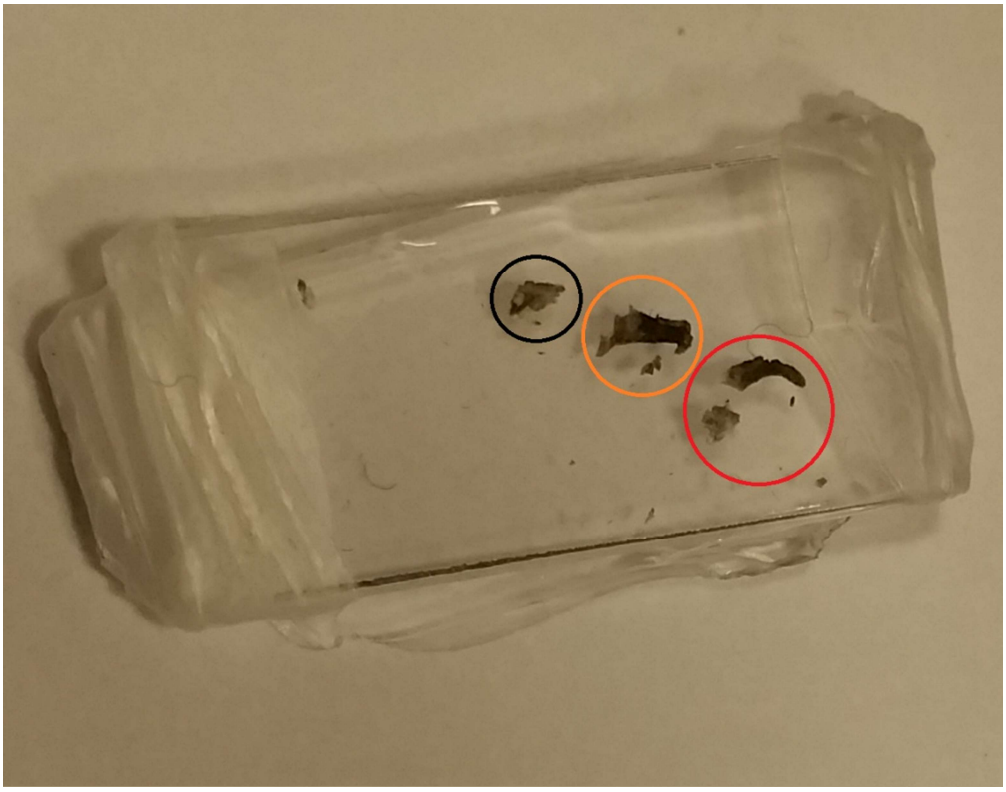

Figure 4.7 – Root samples with HgTe nanoparticles attached; (Black circle) Sample excited at both 458 nm and 808 nm with very little to no emission signal; (Orange circle) Excited at 458 nm with a bright green emission (Figure 4.6c) and a weak emission signal when excited at 808 nm; (Red circle) Excited at 808 nm with the strongest observed signal as shown in Figure 4.6b.

Excitation of either the solution or plant root using 458 nm resulted in bright green emission attributable to chlorophyll, peaking at *ca.* 520 nm, which was significantly narrowed in the solution (Figure 4.6c). No emission was observed from the HgTe quantum dots under this excitation wavelength indicating separation of the emitting chromophore from the HgTe and thus preventing any energy transfer processes from taking place (e.g. Förster energy transfer). Though the HgTe quantum dots were able to absorb the chromophore emission conventionally, their concentration was too weak to observe any re-emission in the near-infrared.

4.6 Conclusion:

Chemical synthesis strategies for the production of nanoparticles are continuously being explored as a mean of finding new and efficient ways to produce these types of materials. As explained in the previous chapters, HgTe nanocrystals are one of the most demanding types of group II-VI materials dues to their near-infrared emission potential. Hence, their production using simple and cost-effective ways has always been encouraged.

The synthetic technique used in the previous chapter introduced a simple reaction methodology using oleic acid and mercury(I) acetate, resulting in the production of colloidal HgTe quantum dots that were able to distribute in organic solvents, i.e. toluene. This synthetic process eliminated the need to use TOP and TOPO as stabilising and reducing agents, promoting the use of less toxic chemicals within the reaction. This motivation inspires work to be carried out towards exploring newer and more environmentally friendly strategies in obtaining these nanoparticles.

The concept of using biological systems as a means to synthesise quantum dots has the potential to provide an economically viable pathway due to the lowered cost of used chemicals. In addition, by allowing the synthesis of nanoparticles within a biological environment this can potentially help narrow the gap between the production and use of quantum dots in healthcare diagnosis and nano-pharmaceuticals.

In this chapter, by using the natural growth process of *Allium fistulosum*, HgTe nanoparticles were prepared via a mutual antagonistic reaction occurring in the living plant. The exact internal reaction taking place is uncertain, however, the presence of phytochemicals within the root of the plant could potentially allow the reduction of Te and subsequent reaction with Hg^{2+} as a way to form highly crystalline HgTe structures. These newly obtained quantum dots were able to emit in the near-infrared range (900 nm – 1675

nm) and consisted of single crystallite particles varying between 5 and 20 nm in diameter with no native organic capping agents.

This simple synthesis method may open up other simple, effective pathways to emissive nanomaterials with interesting optical and electronic properties. Furthermore, work could be carried out as a means to stabilise these biosynthesised nanoparticles by introducing a potential capping agent, allowing them to be dissolved in solvents.

Chapter 5:

Experimental

5.1 Chemicals:

All reagents and materials were obtained from commercial sources and used as received unless otherwise noted. The following are all chemicals used in the reaction procedures:

Mercury(II) acetate (97 %, Sigma-Aldrich), selenium powder (99.5 %, Sigma-Aldrich), tellurium powder (99.8 %, Sigma-Aldrich), sodium tellurite (99%, Sigma-Aldrich), sodium borohydride (99%, Sigma-Aldrich), technical grade oleic acid (90 %, Sigma-Aldrich), Tetradecyltrihexylphosphonium bis(2,4,4-trimethylpentyl)phosphinate (90%, Sigma-Aldrich), technical grade 1-octadecene (90 %, Sigma-Aldrich), toluene (BDH), acetone (BDH), liquid nitrogen (KCL labs), deionised water (18.2 MΩ, KCL labs), Baby Bio Roota liquid rooting hormone 100ml (Amazon).

5.2 Preparation of solvents and air sensitive compounds:

Solvents for use with air stable chemicals were used as received. Toluene was refluxed under over sodium for 1 hour under a nitrogen atmosphere and then distilled. Octadecene was degassed inside a two-neck Schlenk flask under vacuum at 100 ºC for one hour and kept under nitrogen atmosphere before being used. Oleic acid was stored inside a conventional fridge to prevent oxidation.

Air-sensitive reagents were handled as described by Shriver and Dresden. [210] All reactions were carried out under a nitrogen atmosphere using a Schlenk line consisting of four vacuum and nitrogen arms. Schlenk type glassware was used when connected to the manifolds using rubber pressure tubing. The nitrogen and vacuum were able to be selected using a valve which either allowed nitrogen or suction through the tubes. A rotary oil pump maintained the vacuum which was powered using a mains switch with nitrogen being supplied by a cylinder connected directly to the nitrogen manifold. A fume cupboard was

used to manipulate and measure solid chemicals in suitable glassware. Liquid air-sensitive chemicals were delivered by cannula or by injection from glass syringes to Schlenk flasks securely fitted with rubber septa.

Purified colloidal nanoparticles in aqueous solution were stored in vials inside a conventional fridge for immediate testing or kept inside a fume cupboard under nitrogen atmosphere for future use.

5.3 Preparation of Precursors:

5.3.1 Preparation of Hg and OA precursor:

Mercury(II) acetate (0.44 g, 1.4×10^{-3} moles) was dissolved in 20 ml of oleic acid inside a 100 ml two-neck Schlenk flask and heated to approximately 90 ºC whilst stirring to effect dissolution, then cooled to room temperature. The Hg precursor solution was then heated (if required) to the desired synthesis temperature.

Experiments were also performed by keeping the mercury(II) acetate and OA mixture under vacuum for an extended period, in this case, two hours, to remove any excess build-up of acetic acid known to cause aggregation of the nanoparticles. [34]

5.3.2 Preparation of Se precursor:

Se-ODE was prepared inside a 100ml two-neck Schlenk flask by adding selenium powder (0.277 g, 3.5×10^{-3} moles) to 35 ml of purified degassed ODE solution under nitrogen (0.1 M solution). The mixture was stirred and heated to 270 ºC for approximately 1 hour to fully dissolve the selenium powder, before being cooled to room temperature. The solution turned to a red/orange colour when heated to 270 ºC before changing into light green after reaching room temperature. The temperature was monitored using a digital thermometer inserted inside the flask through a rubber septum.

5.3.3 Preparation of Te precursor:

The Te precursor was prepared inside a 100ml two-neck Schlenk flask by adding tellurium power (0.1915 g, 1.5×10^{-3} moles) and sodium borohydride (0.0598 g, 1.6×10^{-3} moles) to 20 ml of purified degassed ODE and 11ml of tetradecyltrihexylphosphonium bis(2,4,4-trimethylpentyl)phosphinate ionic liquid (0.1 M solution). The mixture was stirred and heated to 220 ºC for approximately 1 hour to fully dissolve the selenium powder, before being cooled to room temperature. The solution turned to a dark purple colour when heated to 220 ºC and stayed purple after cooling to room temperature Figure 5.1. It is worth noting that exposure to air for more than 1 min turned the precursor solution to dark green, causing Te to precipitate out of the solution. When this happened, the precursor solution was vacuumed for another hour and reheated to 220 ºC under nitrogen. The temperature was monitored using a digital thermometer inserted inside the flask through a rubber septum.

Figure 5. 1 - Te precursor turning purple after heating to 220 ºC and back to room temperature.

5.4 Chemical Synthesis of nanoparticles:

5.4.1 Synthesis of colloidal HgSe nanoparticles:

In a typical HgSe reaction, the preparation of the Hg and OA precursor was followed by injection of 13 ml of the 0.1 M Se precursor solution (1.3×10^{-3} moles) using a glass syringe. The initial reaction was kept at room temperature with no changes made during the injection and growth phases.

With the room temperature reaction, no initial colouration was observed upon precursor injection. However, after 5 minutes stirring, the colour started to change, becoming distinctly yellow after 20 minutes, orange after 40 minutes, brown at 60 minutes and eventually turning deep black by 90 minutes (Figure 5.2).

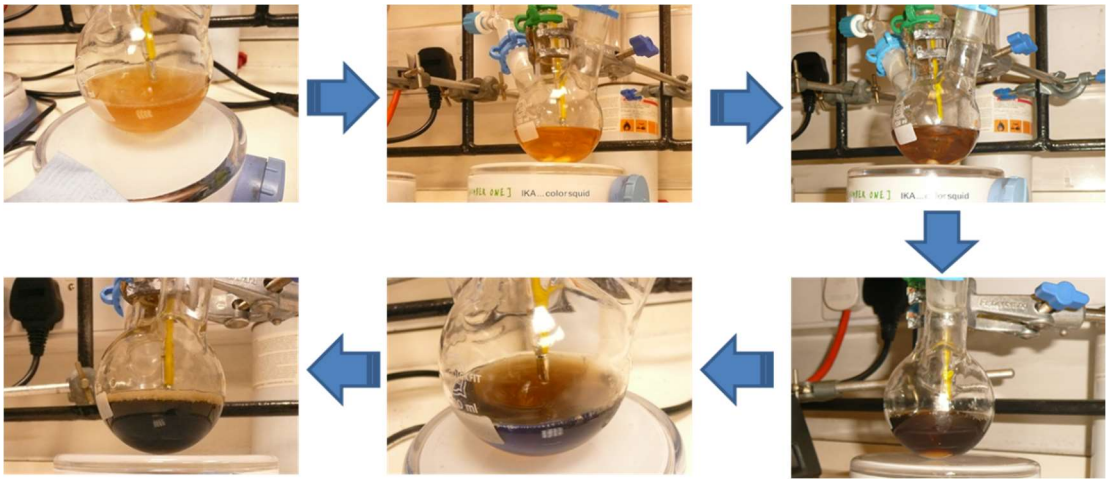

Figure 5. 2 - Formation of HgSe Quantum Dots (Reaction Time: ~ 90min)

The reaction conditions were varied between two additional protocols; 100 ºC injection and growth and room temperature injection and growth followed by immediate freezing in liquid nitrogen and gradual warming to room temperature. The observed colour change was much faster at 100 ºC becoming black in just 10 minutes, whereas the growth from a frozen matrix required 8 hours.

It is worth noting that liquid nitrogen was poured from a cryogenic storage dewar to a low form glass dewar for handling and freezing of the reaction flask. All necessary hazard precautions were taken during this process.

5.4.2 Synthesis of colloidal HgTe nanoparticles:

In a typical HgTe reaction, the preparation of the Hg and OA precursor was followed by injection of 13 ml of the 0.1 M Te precursor solution (1.3×10^{-3} moles) using a glass syringe. The injection was carried out at room temperature under nitrogen atmosphere, followed by immediate freezing in liquid nitrogen using a low form glass dewar and gradual warming to room temperature. After growth was completed, the resulting solution colour was found to be black/dark brown after *ca.* 5 hours.

5.5 Nanoparticles purification:

After particle growth, acetone was added to the solution, followed by centrifugation for 10 minutes resulting in the precipitation of a black solid. Acetone was used as it is a more polar solvent than methanol and increasing the overall polarity of the solution causes larger particles/aggregates to precipitate out as they are less stable. By adding toluene, followed by centrifuging for a further 2 minutes and filtration, a black solution was obtained containing the nanoparticles dispersed in the organic solvent. It is worth noting that the stability of the colloidal particles in the solvent varied between HgSe and HgTe, with HgSe samples lasting for *ca.* one month before any precipitation was observed and HgTe samples precipitating after only one week. Figure 5.3 shows a flowchart representation for different steps taken during the precipitation process for HgSe nanoparticles dissolved in toluene.

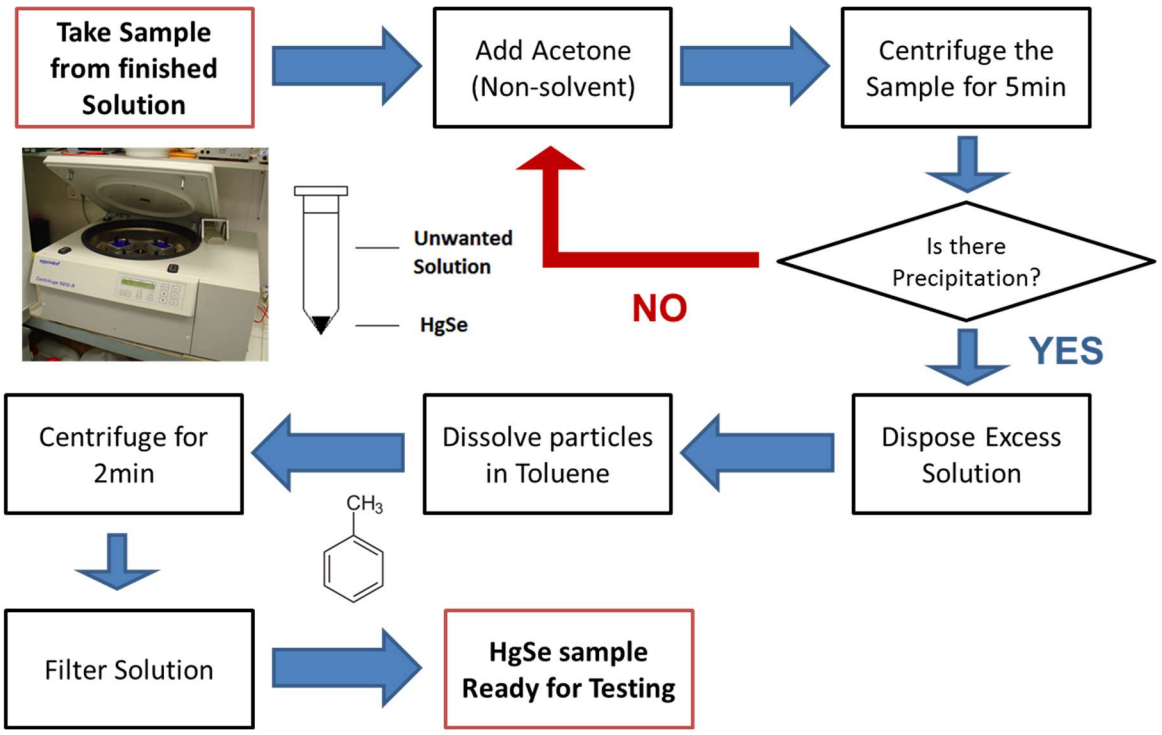

Figure 5. 3 - Flowchart showing the precipitation process for HgSe QDs.

5.5.1 Size-selective purification:

As a means to improve monodispersity within the test samples, size-selective precipitation was carried out. This process was undertaken for both HgSe and the HgTe QDs using acetone.

By adding small amounts of acetone to the reacted solution, larger particles will start to precipitate first with the smaller ones still dissolved in solutions. After a few precipitations, it was found that no more precipitates formed, suggesting the sample was monodispersed and the particles were of a small size. The following flowchart in Figure 5.4 is a modified version of the previous HgSe precipitation technique (Figure 5.3) representing the size-selective precipitation process.

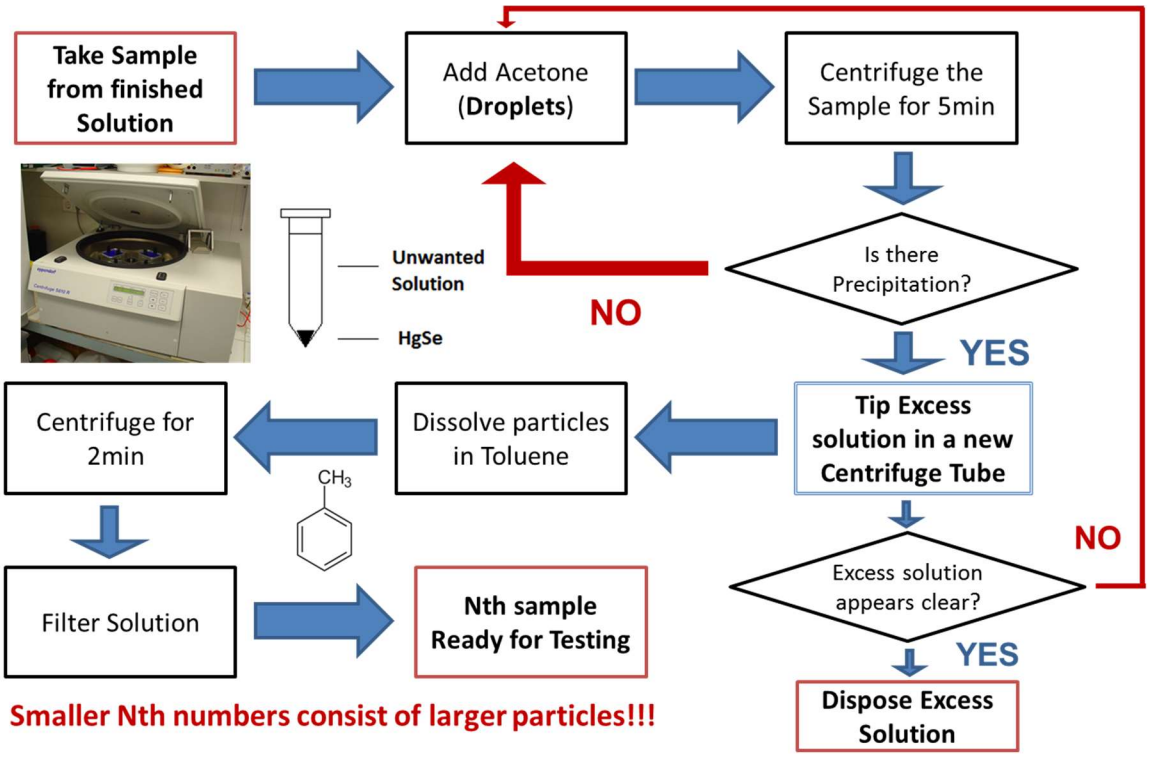

Figure 5. 4 - Flowchart showing the size selective precipitation process.

5.6 Biosynthesis of HgSe nanoparticles using *Allium fistulosum*:

Allium fistulosum were sourced from a local supermarket and soaked in an aqueous rooting hormone solution of 0.0894% w/w 1% naphthylacetic acid as sodium salt (Baby Bio Roota) for one hour. The plants were then bedded in perlite soil and immersed in deionised water in ambient conditions for 4 weeks (2 plants in 500 ml deionised water (18.2 MΩ), with approximately 2 inches of bulb covered by water). After 4 weeks, the plants exhibited clear growth of leaves and roots. Equimolar amounts of precursors (6.3×10^{-5} moles each of $Hg(O_2CCH_3)_2$ and Na_2TeO_3 were added to the water. Following precursors supplementation, the roots were harvested after a further 7-day growth. The resulting inorganic materials could be removed mechanically from the bulbs or were left in place for further investigation.

5.7 Structural measurements and instrumentations:

5.7.1 Transmission electron microscopy (TEM, HRTEM):

Transmission electron microscope (TEM) images for the colloidal HgSe and HgTe nanoparticles were obtained using a TECNAI 20 microscope at 200 kV at the Centre for Ultrastructural Imaging, Guy's campus, KCL. High-resolution images (HRTEM) and selected area electron diffraction patterns for the HgSe samples were collected at the University of Leeds EPSRC Nanoscience and Nanotechnology Research Equipment Facility, using a FEI Tecnai F20 200kv FEGTEM fitted with a Gatan Orius SC600 CCD camera and an Oxford Instruments 80mm2 X-Max SDD EDX detector. The HRTEM for the chemically synthesised colloidal HgTe nanoparticles were collected at the University of Manchester, School of Materials using a Titan 200 kV system. All TEM samples were prepared by dropping a very low concentred toluene distributed nanoparticle solution on to a carbon film TEM grid.

For the TEM analysis of the HgTe quantum dots that were biosynthesised using *Allium fistulosum*, roots were fixed overnight with 4% (w/v) paraformaldehyde, 2% (v/v) glutaraldehyde in 0.05 M phosphate buffer (pH 7.2). After fixation root samples were washed with buffer, incubated in 1% tannic acid for 30 min and post-fixed in 1% (w/v) osmium tetroxide in 0.05 M phosphate buffer (pH 7.2) for 1 hour. Samples were then en-bloc stained with 1% aqueous uranyl acetate overnight at 4 ºC followed by thorough washing before being dehydrated through a graded ethanol series. Root samples were equilibrated with propylene oxide before infiltration with SPURR resin (TAAB) and polymerised at 70 °C for 24 hours. Semithin sections (0.5 μ m) were cut using a Reichert-Jung Ultracut E ultramicrotome and stained with toluidine blue to assess general features. Ultrathin sections (50–70 nm) were also prepared, mounted on 150 mesh copper grids and contrasted using uranyl acetate and lead citrate. Samples were examined on a FEI Tecnai 12 transmission

microscope operated at 120 kV. Images were acquired with an AMT 16000 M camera. EDS was used to confirm the elemental composition of NP.

5.7.2 Scanning transmission electron microscopy (STEM):

STEM imaging was performed using a probe corrected Titan G2 80–200 (S)TEM microscope operated at 200 kV with a beam current of 200 pA and a convergence semi-angle of 18.5 mrad. HAADF imaging was performed with an inner collection semi-angle of 54 mrad. EDXS spectrum images of size 512 × 512 pixels were acquired using the Titan's Super-X four silicon drift detector system with a 30 us dwell time and a total acquisition time of ~5 minutes. EDXS data was acquired and processed using Bruker Esprit software with quantification performed using the Cliff-Lorimer approach without absorption correction. STEM images were acquired using FEI TIA software and processed using the Image-J software.

5.7.3 Serial Block face imaging from biosynthesised HgTe:

Root samples were fixed, washed and incubated in tannic acid as above. The rest of the protocol was modified to ensure the samples were heavily stained with heavy metals to guaranty the high contrasts and electron conductivity required for serial block face imaging in the scanning electron microscope. Therefore, root pieces were further fixed in 1.5% potassium ferrocyanide: 2% osmium tetroxide in 0.1 M phosphate buffer for 1 h at 4 ºC. Tissue was then thoroughly rinsed in distilled water and incubated in 1% aqueous thiocarbohydrazide for 4 min. After further rinsing, the samples were treated with 2% aqueous osmium tetroxide for 30 min, rinsed and en-bloc stained in 1% uranyl acetate overnight at 4 ºC. To further enhance contrasts in the samples, one last treatment with Walton's Lead solution was carried out for 30 min at 60 ºC, before proceeding to dehydration

in an ethanol series and infiltration with Durcupan ACM resin (Sigma). After embedding and curing, tissue blocks were mounted on Gatan 3View aluminum pins using conductive glue (CircuitWorks Conductive Epoxy) and trimmed accordingly. Before sectioning/imaging, samples were gold coated to increase electron conductivity. The specimens were then placed inside a Jeol field emission scanning electron microscope (JSM-7100F) equipped with a 3View 2XP system (Gatan). For this particular experiment, sections thickness was set at 40 nm (Z resolution). Samples were imaged at 1 kV under high vacuum using a 4096 × 4096 scan rate, which gave a final pixel size of 45 nm.

5.7.4 X-Ray powder diffraction (XRD):

X-ray diffraction (XRD) measurements were carried out on nanoparticles using a Bruker AXS D8 diffractometer. The XRD samples were prepared by pipetting a highly concentrated nanoparticle solution in toluene drop-wise on a small piece of glass slide with a surface area of 10 mm x 10 mm until an estimated 1mm thick solid layer was formed.

5.8 Optical spectroscopy and instrumentations:

5.8.1 Absorption spectroscopy:

The absorption spectroscopy measurements for the colloidal HgSe and HgTe quantum dots created using inorganic methods were obtained using a Hitachi U-4100 spectrophotometer. The samples were tested in cuvettes containing toluene, which was used as the baseline measurement.

The absorption spectra for the biosynthesised HgTe quantum dots were obtained using a Varian Cary 3000 spectrophotometer after the nanoparticles were suspended in water.

5.8.2 Photoluminescence spectroscopy (PL):

The emission spectra for the colloidal HgSe and HgTe quantum dots created using inorganic colloidal methods, were recorded using an 808 nm excitation laser and a Newport InGaAs 818-IG detector. Similar to the absorption measurements, the samples were distributed in toluene inside cuvettes during the tests.

For the HgTe quantum dots that were biosynthesised using *Allium fistulosum*, the photoluminescence spectra were obtained using 812 nm laser diode (Thorlabs) or 457 nm Ar-ion (Coherent) sources. The emission was collected and dispersed in a Bentham TMc300 monochromator (600 g/mm or 1200 g/mm grating) and detected using lock-in amplification (Signal Recovery SR7265) and an InGaAs detector (Newport 818-IG) or Si detector (Newport 818-SL). Emission spectra have been corrected for the system response.

4.8.3 Quantum yield measurements:

An 808 nm excitation laser and a Newport InGaAs 818-IG detector was used along with an integrating sphere to obtain the quantum yield of the nanoparticles. [35] This was the same setup used to measure the photoluminescence of the colloidal HgSe and HgTe nanoparticles. As a means to calculate the QY, the following procedure was used in combination the measurements taken from the integrating sphere experiment. It is worth mentioning that the QY was not measured for the biosynthesised HgTe nanoparticles obtained using *Allium fistulosum*, due to the low signal strength observed from the photoluminescence measurements.

As an overview, QY can be defined as the absolute quantum efficiency for the PL of a given sample, hence the ratio between the light absorbed and the light emitted by the QDs. This external radiative efficiency **n** can be represented by Equation 5.1.

$$\mathbf{n} = \frac{\text{number of photons emitted}}{\text{number of photons absorbed}} \quad \textbf{(5. 1)}$$

As the absorption energy is the total energy of the non-radiative (k_{nr}) and radiative (k_r) recombination rates, the QY can also be represented by the Equation 5.2.

$$\mathbf{n} = \frac{k_r}{(k_{nr} + k_r)} \quad \textbf{(5. 2)}$$

An integrated sphere is a hollow sphere which has its inner surface coated with a diffusely reflecting material (typically barium sulfate). When a light source is placed in an ideal integrated sphere, the light is redistributed isotropically over the interior surface of the sphere regardless of the angular dependency of the emission. The basic experimental setup consists of three stages (Figure 5.5a,b,c). These stages will compare the number of output photons with the initial input light sent through the sphere taking into consideration both the amount of absorbed and unabsorbed light by the sample. Figure 5.5a shows the setup of the first measurement taken from the sphere with no sample placed inside. If **L** is the amount of unabsorbed light, the output light measured (**La**) would be equal to the input light sent through the sphere via the 808 nm laser. For the second stage (Figure 5.5b), the sample is placed inside the sphere with the incident laser directed on to the sphere wall. In this scenario, the sample will absorb a fraction **μ** of the light reflected from the surface of the sphere emitting a PL of **Pb**. Taking into consideration the initial incident light is the same in both **a** and **b** stages, the total unabsorbed light in this stage **Lb** can be represented by Equation 5.3.

$$\mathbf{Lb} = \mathbf{La}\,(\mathbf{1} - \mu) \quad \textbf{(5. 3)}$$

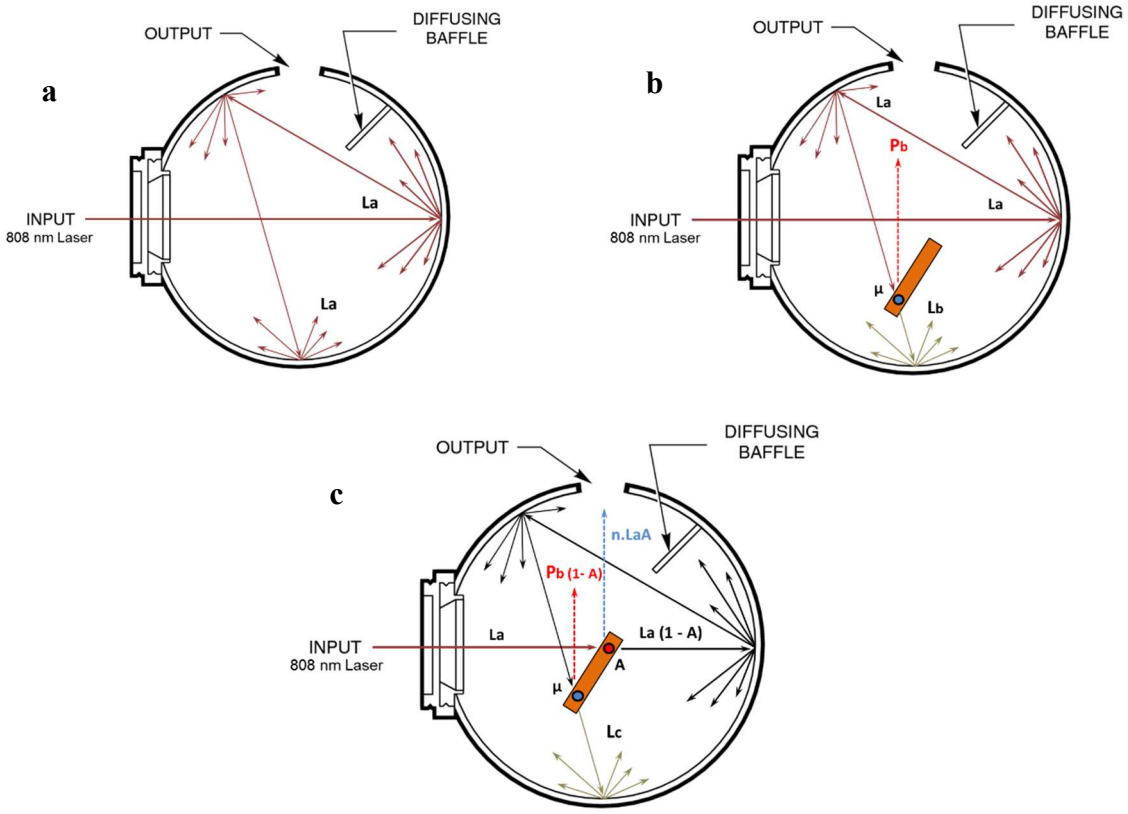

Figure 5. 5 - Integrated sphere setup showing all three experimental stages. a) No sample present in sphere b) Sample indirectly excited by the laser c) Sample in direct contact with the excitation laser.

The final stage shown in Figure 5.5c is similar to the second, except that the collimated laser beam is directed on to the sample, with the light reflected from the surface of the sample being directed onto the sphere wall and not back through the entrance hole. In this scenario, the sample absorbs light in two instances. The first being the fraction of absorption from the incident laser **A** and the second being the fraction **μ** of scattered light from the sphere surface. Hence, the total quantity of unabsorbed light **Lc** can be represented by Equation 5.4.

$$\mathbf{Lc} = \mathbf{La}\,(\mathbf{1} - \mu)(1 - \mathbf{A}) \qquad \textbf{(5. 4)}$$

Whereby using Equation 5.3 the fraction of absorbed incident light **A** can be obtained (Equation 5.5).

$$\mathbf{A} = 1 - \left(\frac{\mathbf{Lc}}{\mathbf{Lb}}\right) \tag{5. 5}$$

Furthermore, the initial emitted light from the sample could be characterised as **n.LaA** with **n** being the QY as mentioned in Equation 5.1. By representing the total emitted light from the sample in the third stage to be **Pc**, Equation 5.6 can be deduced combining the emission from both the incident and the scattered beams.

$$\mathbf{Pc} = \mathbf{Pb}(1 - \mathbf{A}) + \mathbf{n}.\mathbf{LaA} \tag{5. 6}$$

Hence using this to acquire Equation 5.7 for obtaining the quantum yield value.

$$\mathbf{n} = \frac{\mathbf{Pc} - \mathbf{Pb}(\mathbf{1} - \mathbf{A})}{\mathbf{LaA}} \tag{5. 7}$$

Where **Pb (1 - A)** is the total emission from the second stage of measurements (Figure 5.5b) effected by the initial fraction of absorption **A**.

As an example, the quantum yield of the colloidal HgSe QDs from Chapter 2 was obtained using Equations 5.5 and Equations 5.7 with the data gathered from all three experimental stages, resulting in the QY being calculated to be approximately 4 %, with a maximum of 7 %. These results were consistent regardless of the HgSe samples used and where not effected by the difference in concentration. Figure 5.6 represents the readings taken from the unabsorbed light exiting the sphere in all three experimental stages, with Figure 5.7 showing the emission from the HgSe sample when indirectly (**Pb**) and directly (**Pc**) excited by the laser.

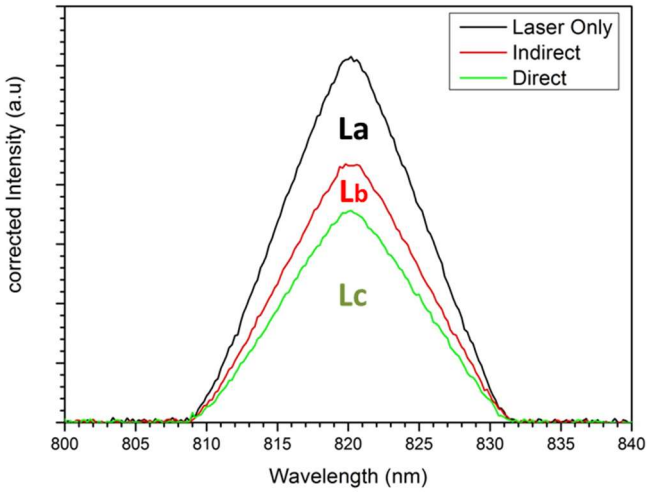

Figure 5. 6 - Output laser reading in all three experimental stages.

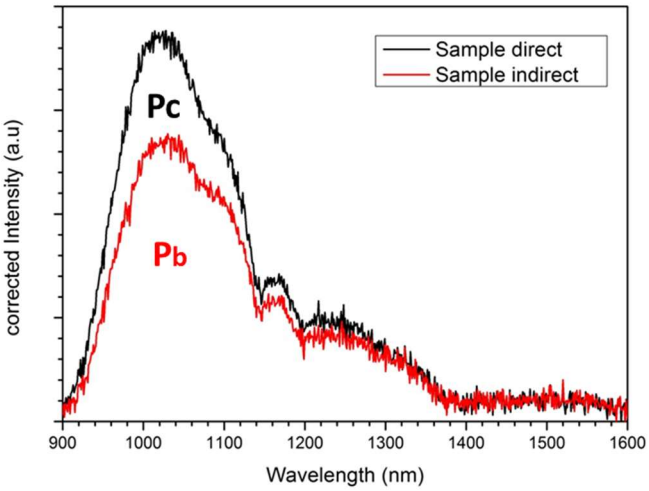

Figure 5. 7 - The direct and indirect emission reading taken from the sphere

An unavoidable problem with using the integrated sphere technique is the sample having a reabsorption effect. This happens when a fraction of the photons emitted are reabsorbed back into the sample resulting in lower detected emission. This can have a significant consequence with poorly monodispersed samples due to the HgSe QDs absorbing light at a wider range of wavelengths within the NIR region. The size-selective precipitation technique was used as a means of reducing this effect.

Chapter 6:

Conclusions and Further Work

6.1 Conclusions:

The development of new methodologies towards the production of near-infrared quantum dots has always been of interest due to the vast potential range of applications, such as communication technology, solar cells and medical diagnostic industries. Hence, introducing simple and cost-effective routes in obtaining these materials provides confirmation that nanoparticles can be obtained and manipulated as an approach to allow mass production to consequently satisfying the required field of use.

This thesis explained how mercury chalcogenide nanoparticles could be synthesised at room temperature using both inorganic colloidal and biological methods, with a primary focus on HgTe and HgSe. The inorganic colloidal routes introduced here do not include TOP and TOPO, which are commonly used capping agents in the production of colloidal nanoparticles. As an alternative, oleic acid is used as the primary passivating agent, primarily due to its reduced toxicity (for example, it is present in olive oil) which in turn encourages cost efficiency and reduced negative environmental effects.

Colloidal HgSe and HgTe nanocrystals were synthesised at room temperature with post precursor injection freezing using liquid nitrogen. The rapid temperature reduction was implemented as a means to encourage nucleation without rapid growth, hence controlling the particle size and monodispersity. The HgSe particles were also synthesised without using post freezing and at 100°C. This was carried out to understand the differences in morphologies and optical characteristics between the obtained particles. As a result, it was concluded that the introduction of liquid nitrogen after the precursor injection has a positive effect towards the formation of nanoparticles with better monodispersity (Figure 2.3) and improved optical properties, which were shown from the acquired quantum efficiencies. The measured optical features also showed a clear red-shift in both absorption and emission spectra (Figure 2.8), from low temperature to the 100 °C synthesis, which resulted in a rapid

nanoparticle growth shown in the TEM images (Figure 2.6). Additionally, by slowing down the reaction rate via liquid nitrogen absorption, spectra readings were able to be taken at intervals in real-time as a means to observe the formation of the quantum dots during nucleation (Figure 2.2).

Purified post freeing samples observed under TEM after 6 months showed a hollow structure which could indicate the formation of Kirkendall voids supported by the Kirkendall effect (Figure 2.5). [179] The hollow central structure was also somewhat visible in the HgSe nanoparticles synthesised at room temperature without post freezing, however as the samples had significant aggregation in comparison to the post freezing particles, this was not clearly observed. Furthermore, the HRTEM images taken from the freshly prepared, post freezing, cubic nanocrystals (Figure 2.4) showed a lighter central structure, indicating a potential weakness in the structural integrity present in the middle of the particles. This is the initial stage which may lead to the formation of a Kirkendall void, however, further studies are necessary to confirm this.

A similar post freezing technique was used to synthesis HgTe nanoparticles with the addition of trihexyl-tetradecyl-phosphonium phosphinate ionic liquid and sodium borohydride to help reduce the tellurium, resulting in the formation of a stable precursor. Similar to the HgSe nanoparticles, the structural and optical properties were examined with results showing increased aggregation, potentially due to nanoparticle surface defects, possibly caused by the rapid room temperature growth known to occur with Hg nanocrystals (Figure 3.1). [12] [128] However, sample monodispersity was well defined within the tested samples including optical and absorption levels clearly manifesting in near-infrared wavelengths (Figure 3.5). It is worth noting that aggregation in nanocrystals is somewhat encouraged in the production of solar cells and light-sensitive devices. This is due to the

natural flow of charge within the material, consequently resulting in an effective cost saving solution, as the material does not need to be re-treated for this capability.

It is worth mentioning that further STEM utilisation would be advantageous towards obtaining atomic structural composition within the nanoparticles. In the last decade, annular dark-field (ADF) STEM imaging has been used extensively due to its strong reliance on scattering signal intensity on atomic numbers. Hence, known as Z-contrast imaging, this technique heavily depends on the detection of incoherently scattered electrons passing through the sample. [211]

Conventional HRTEM is known to be a high coherent mode of imaging, which relies on the illumination of an electron transparent sample with a coherent plane wave. The propagating electrons create diffraction pattern which in turn, are picked up using a bright field (BF) detector for phase-contrast imaging. Moreover, traditional TEM machines also require the formation of diffraction patters with both systems using coherent sample illumination to allow constructive and destructive interference to occur. [211] However, this can cause contrast-reversal effects within the image, with certain structures appearing dark even though this should not be the case. Intense contrast-reversal can also be apparent as the sample thickness is changed during analysis. This is mainly due to the backscattering of electrons into the samples, causing strong interference effects. [211] Consequently, the use of specialised annular detectors that only collect scattered electrons at higher angles, also known as high angler annular dark-field (HAADF), have the potential to show higher atomic number (Z) contrast. This eliminates the majority of the interference effects due to the incoherent nature of the electron wave-functions, resulting in a clear structural interpretation of the image, as shown in Figure 3.4A. This method combined with STEM-EDX elemental mapping provided a clear indication of an even Hg and Te distribution within the samples

(Figure 3.4B). In addition to this, the XRD spectra (Figure 3.3) supported the cubic structure of the nanocrystals, which was observed in the TEM images (Figure 3.2).

Despite having superior Z-contrast resolution, HAADF does have some limitations which should be highlighted. Notably, as the high scattering angle signal intensity is correlated to the atomic number of the material within the sample, high-mass non-crystalline areas could display a similar contrast as high-mass areas with high crystallinity, making it challenging to distinguish between them. Therefore, any sample undertaking HAADF analysis should be purified and cleaned extensively during the preparation process in comparison to regular TEM imaging. Furthermore, STEM imaging does suffer from localised sample limitations, as the atomic scale information within a small area of investigation may not represent the whole sample equally. [212] Additionally, after prolonged periods, the focal area can be vulnerable to the impact of focused high energy electrons propagating through the nanoparticle sample, causing structural manipulation and damage by evaporation, or even melting during analysis, which in turn can result in information inaccuracies. However, regardless of these factors, HAADF within STEM imaging has become very popular in the field of nanoparticle characterisation and can provide vital sub-particles and atomic structural resolution information about the nanomaterial, [212] thus should be considered for future HgTe and HgSe investigations.

As mentioned in Chapter 3, the popularity of HgTe nanoparticles comes from their highly tunable absorption characteristics in the NIR spectrum range. Moreover, HgTe nanocrystals are one of the more mature materials to be used in optoelectronic systems, which is attributable to their good charge transport properties, which is advantageous for the design of phototransistors. [213] This critical characteristic, combined with their absorption tunability increases the demand for efficient and cost-effective production of HgTe nanoparticles. Hence, in the interest of satisfying this requirement, Chapter 4 demonstrated

a biosynthesis methodology towards obtaining infrared emitting HgTe quantum dots in a living plant *via* a mutual antagonistic reaction taking place in the plant's natural growth process. This consisted of exposing common *Allium fistulosum* to both mercury and tellurium salts under ambient conditions. This resulted in the expulsion of crystalline, non-passivated HgTe quantum dots that exhibited emissive characteristics in the NIR

spectral region. Due to the absence of a stabilising agent, the uncapped nanoparticles displayed significant aggregation when observed using TEM imaging (Figure 4.4). As previously mentioned, this would be beneficial for removing any obstacles that could prevent the mobility of charge carried within the samples, however, the deficiency of surface ligands does negatively influence the emission as the untreated defects on the semiconductor surface can cause charge carrier traps. This is a critical factor for specific applications such as biological imaging, as it reduces the optical efficiency of the quantum dots.

Despite the lack of a thiolated capping agent, the HgTe nanoparticles did exhibit emission in the near-infrared (Figure 4.6), which included the wavelengths associated with telecommunications. This is valuable evidence to support the reason behind the strong reputation HgTe nanoparticles have as excellent contenders in providing signals in the NIR spectral region, regardless of using any form of stabilising agent.

The demonstrations described in this thesis focus on simple methodologies for obtaining mercury chalcogenide quantum dots using both inorganic colloidal and biological techniques. This hopes to provide further encouragement and support towards opening up other, less toxic and cost-effective pathways beneficial to achieving high-quality nanomaterials that can display interesting optical, structural and electronic attributes.

6.2 Further work:

The work presented in this thesis provides the potential for further analysis of various aspects of the proposed ideas. The study of metal-based quantum dots is consistently moving forward due to their vast application capabilities from medical to electrical and energy industries, hence any contribution paves the way for future possibilities.

The focus of this thesis was to propose simple routes towards the synthesis of HgSe and HgTe nanoparticles with various optical capabilities. These aqueous and biological methodologies provide evidence supporting the simplistic approach of mercury chalcogenide nanoparticle production. However, the outlined ideas provide the prospective for further investigations.

6.2.1 Core-Shell capping of HgSe and HgTe quantum dots

A significant problem facing the production of mercury chalcogenide QDs is the rapid aging of the nanoparticles. Freshly prepared HgSe and HgTe QDs ideally require the best quantum yield, with the PL gradually moving towards longer wavelengths over time followed by a sudden drop in QY after about two weeks. [90] This effect has been known to be more rapid during heating of the nanocrystals, with the efficiency dropping within minutes at 100 ºC. [90] This sudden drop in efficiency is a genuine concern for the long term stability and use of these materials in various applications.

One possible way of overcoming this issue is by capping the nanocrystal surface with a higher bandgap inorganic layer. A wider bandgap shell has the potential to provide the passivation of active surface states of the core nanocrystal, eliminating any surface degradation which can result in unwanted non-radiative recombination. [43] Nanoparticles with core-shell structures are known to have enhanced radiative recombination with higher QY and PL levels in comparison to their bare organically passivated core. Hence by adding

a shell, a much more stable material with higher tolerance is formed and the ageing process is significantly reduced. Examples of various core/shell structures include HgTe/CdS [90], HgTe/CdTe [44], CdSe/HgSe [43], CdSe/HgS [47] and CdSe/ZnS [46] with reports of quantum yields of up to 98% for CdSe/ZnS materials, depending on the ZnS shell thickness. [47] It is hence advisable to attempt capping the HgSe and HgTe nanocrystals with a layer of CdSe and CdTe to produce a stable core/shell heterostructure, with the aim of improving the materials fluorescence properties.

Furthermore, capping the HgSe and HgTe nanoparticles with organic protein shells could reduce their toxicity levels, increasing their potential use in medical imaging and diagnostic applications such as biomarkers and disease analysis. [214]

Moreover, cytotoxicity tests using toxicology assessment could be carried out after surface capping with the aim to analyse possible adverse effects towards living cells. Similar studies have been performed using yeast cells and CdTe quantum dots with effective results. [215] Additionally, silica-coated CdTe quantum dots have also been tested for toxicity in live mice with positive results, thus indicating that a similar technique could be used on HgSe and HgTe nanoparticles with comparable results. [216]

6.2.1 Improvements in HgTe nanoparticle aggregation

As previously mentioned in Chapter 3, HgTe nanoparticle precursors are known to be highly reactive during RT synthesis, hence triggering sudden particle aggregation as seen in the TEM images (Figure 3.1). This effect was seen even after the introduction of liquid nitrogen to the reaction process, indicating rapid particle growth directly before growth temperature reduction. The HgSe nanoparticles, seen in Chapter 1, however, did not exhibit this problem at room temperature, which could be due to the Hg and OA precursor being kept under vacuum for a prolonged period of time before injection of the Se precursor to

remove the excess build-up of acetic acid during the formation of mercury oleate. Never-the-less, this technique was also implemented when synthesising the HgTe nanoparticles.

Even though nanoparticle aggregation is encouraged for solar device applications, due to their charge transfer capabilities, mentioned in Chapter 3, one way of potentially improving this would be to reduce the Hg precursor temperature before Te injection is applied. This will provide a low baseline temperature before the initiation of the reaction. This small adjustment with the addition of a further nanoparticle shell capping would have a positive effect on the separation between the particles, resulting in reduced visible aggregation.

6.2.3 Biosynthesis nanoparticle capping

One of the interesting aspects of using a mutual antagonistic reaction in *Allium Fistulosum*, explained in Chapter 4, is the natural occurrence caused by the plant's growth which in turn produces the nanoparticles as a by-product. This could be interpreted as a form of a defence mechanism by the organism against potentially toxic compounds, hence manipulating mercury acetate and sodium tellurite salts in an internal reduction process to form less toxic HgTe particles. Further studies could be made towards the understanding of the internal reaction mechanism and the potential addition of a stabilising agent to prevent particle aggregation. The observed optical effects from the obtained HgTe nanoparticles is remarkable, even without any form of capping agent, nonetheless, this could be improved by allowing ligands or protein shells to passivate the nanoparticle surface as a means of correcting surface defects causing trapped electron holes.

In addition, the same experimental procedure can be carried out using sodium selenite (Na_2SeO_3) as a means of obtaining HgSe nanocrystals that could have similar optical characteristics. Similarly, cadmium acetate $Cd(CH_3CO_2)_2$ could be used in replacement of

mercury acetate $Hg(O_2CCH_3)_2$, to biosynthesis CdTe or CdSe nanocrystals with potential optical capabilities.

6.2.4 Additional thoughts

By taking into account the previous areas proposed for further analysis, additional work could be carried out in various areas of this project as a means to provide further information towards the following details:

1) The formation of Te precursor in ionic liquid

The Te precursor produced in Chapter 3 combined Te with a reduction agent and IL, resulting in an interesting purple solution shown in Figure 5.1. This colour change occurred after heating the precursor to 220°C, very similar to the Se-ODE precursor produced in Chapter 2, where the solution changed into a red/orange colour before turning to light green at room temperature. Yet, it is worth noting that the Te precursor consistently remained purple after reaching room temperature as long as it was kept under a nitrogen atmosphere. Studying this process and the mechanism for the observed colour change could provide a better understanding towards further improving the quality of precursor production. We still do not understand the nature of this precursor and further studies into the exact identification of this product would benefit other synthetic chemists.

2) The formation of hollow nanoparticles

The observations made in the TEM images (Figure 2.5) in Chapter 2, identified the formations of voids which could be linked to the studies relating to nano Kirkendall effects influenced by outward and inward atomic diffusion of the crystal structure. [179]

The presence of hollow Kirkendall voids were observed during TEM viewings of HgSe samples after a 6-month period. This was followed by the increased aggregation and loss of nanoparticle ligands due to the observed precipitation within organic solution. It is

worth noting that the formation of the vacancies does not necessarily indicate Kirkendall voids, however, studies have shown that the difference in diffusivity of two heterogeneous solids within a nanostructure could influence this effect. [179] Furthermore, it has been suggested that the hollow nanocrystals are mainly formed from colloidal synthesised routes due to nanoparticle oxidation in organic solutions. [179]

Although the Kirkendall effects have been observed in numerous core-shell structures, due to the difference in diffusion rates between the core material and shell, less is known on how shaped nanocrystals behave during the Kirkendall process. Even so, this could pave the way for the production of quantum dots with various morphologies that can potentially be used for drug delivery, energy devices and various other applications. [217]

Appendix

List of Author's Publications

1) **Title: "**The room temperature phosphine-free synthesis of near-infrared emitting HgSe quantum dots."

Source: *Journal of Materials Chemistry C*, Feb 2014, vol 2, pp 2107–2111

Abstract: Luminescent mercury selenide (HgSe) quantum dots have been synthesised by a phosphine-free method using oleic acid as a capping agent. The modification of experimental conditions such as temperature resulted in particles of various sizes (15–100 nm) and morphologies not previously seen in HgSe, with emission tunable between 1000 nm and 1350 nm.

2) **Title: "**The biosynthesis of infrared-emitting quantum dots in allium fistulosum."

Source: *Scientific Reports*, Feb 2016, **6**, article number: 20480

Abstract: The development of simple routes to emissive solid-state materials is of paramount interest, and in this report, we describe the biosynthesis of infrared emitting quantum dots in a living plant via a mutual antagonistic reaction. Exposure of common Allium fistulosum to mercury and tellurium salts under ambient conditions resulted in the expulsion of crystalline, non-passivated HgTe quantum dots that exhibited emissive characteristics in the near-infrared spectral region, a wavelength range that is important in telecommunications and solar energy conversion.

3) **Title: "**Synthetic routes to mercury chalcogenide quantum dots."

Source: *Journal of Materials Chemistry C*, Apr 2018, vol 6, pp 5097--5112

Abstract: Mercury chalcogenides are a relatively unexplored family of semiconductor quantum dots despite having novel optical properties that have potential applications in solar energy conversion, optical amplification and even biological imaging. In this review, we explore the synthetic chemistry behind the preparation of these materials and their resulting optical characteristics.

References

[1] S. Ameen, M. S. Akhtar and H.-S. Shin, Eds., *Nanostructures*, *InTech*., 2017, Chap. **1**, 1-7.

[2] G. Ramalingam, P. Kathirgamanathan, G. Ravi, T. Elangovan, B. A. Kumar, N. Manivannan and K. Kasinathan, *Quan. Dot. - Fund. and Appli*., *InTech*., 2020, Quan. Conf. Eff. of 2D Nano., 1-11.

[3] T. Torchynska and Y. Vorobiev, G. Gargiulo and A. McEwan, Eds., *Adv. Biomed. Eng.*, *InTech.*, 2011, Chap. **9**, 143-182.

[4] Ç. Allahverdi and M. H. Yükselici, *New J. Phys*., 2008, **10**, 1-9.

[5] O. V. Buganov, D. H. Nguyen, S. A. Tikhomirov and A. A. Onuschenko, *Adv. Nat. Sci.: Nanosci. Nanotechnol.*, 2011, **2**, 1-5.

[6] Y. C. Wang, C. T. Yuan, Y. C. Yang, M. C. Wu, J. Tang and M. H. Shih, *Nano Rev.*, 2011, **2**, 1-5.

[7] H. Chang, Z. Sun, K. Y. Ho, X. Tao, F. Yan, W. M. Kwok and Z. Zheng, *Nanoscale*, 2011, **3**, 258-264.

[8] P. M. Allen, W. Liu, V. P. Chauhan, J. Lee, A. Y. Ting, D. Fukumura, R. K. Jain and M. G. Bawendi, *J. Am. Chem. Soc.*, 2010, **132**, 470-471.

[9] M. T. Harrison, S. V. Kershaw and M. G. Burt, *Pure Appl. Chem.*, 2000, **72**, 295-307.

[10] R. Saran, M. N. Nordin, and R. J. Curry, *Adv. Funct. Mater.* 2013, **23**, 4149-4155.

[11] S. Keuleyan, E. Lhuillier, P. Guyot-Sionnest and V. Brajuskovic, *Nat. Photonics*, 2011, **5**, 489-493.

[12] P. Howes, M. Green, C. Johnston and A. Crossley, *J. Mater. Chem.*, 2008, **18**, 3474-3480.

[13] L. Qian, Y. Zheng, J. Xue and P. H. Holloway, *Nat. Photonics*, 2011, **5**, 543-548.

[14] J. Wang, Y. Lu, F. Peng, Y. Zhong, Y. Zhou, X. Jiang, Y. Su and Y. He, *Biomater*., 2013, **34**, 9509-9518.

[15] D. Geibler, L. J. Charbonniere, R. F. Ziessel, N. G. Butlin, H. G. Lohmannsroben and N. Hildebrandt, *Angew. Chem. Int. Ed.*, 2010, **49**, 139-1401.

[16] M. Han, X. Gao, J. Z. Su and S. Nie, *Nat*. *Biotech*., 2001, **19**, 631-635.

[17] C. E. Probst, P. Zrazhevskiy, V. Bagalkot and X. Gao, *Adv. Drug Del. Rev.*, 2013, **65**, 703-718.

[18] E. H. Sargent, Nat. *Photonics*, 2012, **6**. 133-135.

[19] P. V. Kamat and J. Phys. *Chem. Lett.*, 2013, **4**, 908-918.

[20] D. Bozyigit and V. Wood, *MRS Bull.*, 2013, **38**, 731 – 736.

[21] B. S. Mashford, M. Stevenson, Z. Popovic, C. Hamilton, Z. Zhou, C. Breen, J. Steckel, V. Bulovic, M. Bawendi and S. Coe-Sullivan, *Nat. Photonics*, 2013, **7**, 407-412.

[22] C. Ippen, T. Greco, Y. Kim, J. Kim, M. S. Oh, C. J . Han and A. Wedel, *Org. Elec.*, 2014, **15**, 126-131.

[23] K. Bourzac, *Nature*, 2013, **493**, 283.

[24] C. B. Murray, D. J. Norris and M. G. Bawendi, *J. Am. Chem. Soc.*, 1993, **115**, 8706-8715.

[25] O. Chen, H. Wei, A. Maurice, M. Bawendi and P. Reiss, *MRS Bull*., 2013, **38**, 696 – 702.

[26] L. M. Wheeler, L. M. Levij and U. R. Kortshagen, J. Phys. *Chem. Lett.*, 2013, **4**, 3392−3396.

[27] A. L. Rogach, A. Eychmüller, S. G. Hickey and S. V. Kershaw, *Small*, 2007, **3**, 536.

[28] S. V. Kershaw, M. T. Harrsion and M. G. Burt, *Philos. Trans. R. Soc.*, *A*, 2003, **361**, 331.

[29] N. Orlowski, J. Augustin, Z. Golacki, C. Janowitz and R. Manzke, *Phys. Rev. B: Condens. Matter Mater. Phys.*, 2000, **61**, R5058.

[30] V. Rinnerbauer, K. Hingerl, M. Kovalenko and W. Heiss, *Appl. Phys. Lett*., 2006, **89**, 193114.

[31] K. U. Gawlik, L. Kipp, M. Skibowski, N. Orlowski and R. Manske, *Phys. Rev. Lett*., 1997, **78**, 3165.

[32] M. von Truchsess, A. Pfeuffer-Jeschke, C. R. Becker, G. Landwehr and E. Batke, Phys. Rev. B: Condens. *Matter Mater. Phys*., 2000, **61**, 1666.

[33] M. Green, P. Prince, M. Gardener and J. Steed, *Adv. Mater*., 2004, **16**, 994.

[34] A. Delin, Phys. Rev. B: Condens. *Matter Mater. Phys*., 2002, **65**, 153205.

[35] D. Durmett Torres, P. Banerjee, S. Pamidightantam and P. K. Jain, *Chem. Mater*., 2017, **29**, 6356.

[36] J. Li, C. He, L. Meng, H. Xiao, C. Tang, X. Wei, J. Kim, N. Kioussis, G. M. Stocks and J. Zhong, *Sci. Rep*., 2015, **5**, 14115.

[37] R. L. Wells, C. G. Pitt, A. T. McPhail, A. P. Purdy, S. Shafieezad and R. B. Hallcock, *Chem. Mater*., 1989, **1**, 4.

[38] M. D. Healy, P. E. Laibinis, P. D. Stupik and A. R. Barron, *Chem. Commun*., 1989, 359.

[39] C. B. Murray, S. Sun, W. Gaschler, H. Doyle, T. A. Betley and C. R. Kagan, *IBM J. Res. Dev*., 2001, **45**, 47.

[40] J. Q. Grim, L. Manna and I. Moreels, *Chem. Soc. Rev*., 2015, **44**, 5897.

[41] A. L. Efros, J. B. Delehanty, A. L. Huston, I. L. Medintz, M. Barbic and T. D. Harris, *Nat. Nanotechnol*., 2018, **13**, 278.

[42] S. M. Stuczynski, Y.-U. Kwon and M. L. Steigerwald, *J. Organomet. Chem*., 1993, **449**, 167.

[43] M. L. Steigerwald and C. R. Sprinkle, *J. Am. Chem. Soc.*, 1987, **109**, 7200.

[44] J. G. Brennan, T. Siegrist, P. J. Carroll, S. M. Stuczynski, P. Reynders, L. E. Brus and M. L. Steigerwald, *Chem. Mater*., 1990, **2**, 403.

[45] R. Carter, J. Sloan, A. I. Kirkland, R. R. Meyer, P. J. D. Lindan, G. Lin, M. L. H. Green, A. Vlandas, J. L. Hutchison and J. Harding, *Phys. Rev. Lett*., 2006, **96**, 215501.

[46] A. Eychmüller, A. Ha¨sselbarth and H. Weller, *J. Lumin*., 1992, **53**, 113.

[47] A. Ha¨sselbarth, A. Eychmüller, R. Eichberger, M. Giersig, A. Mews and H. Weller, *J. Phys. Chem*., 1993, **97**, 5333.

[48] A. Mews and A. Eychmüller, Ber. Bunsenges. *Phys. Chem*., 1998, **102**, 1343.

[49] A. Eychmüller, A. Mews and H. Weller, *Chem. Phys. Lett*., 1993, **208**, 59.

[50] D. Schooss, A. Mews, A. Eychmüller and H. Weller, Phys. Rev. B: Condens. *Matter Mater. Phys*., 1994, **49**, 17072.

[51] A. Mews, A. V. Kadavanich, U. Banin and A. P. Alivisatos, *Phys. Rev. B: Condens. Matter Mater. Phys*., 1996, **53**, R13242.

[52] A. Mews, A. Eychmüller, M. Giersig, D. Schooss and H. Weller, *J. Phys. Chem*., 1994, **98**, 934.

[53] A. T. Yeh, G. Cerullo, U. Banin, A. Mews, A. P. Alivisatos and C. V. Shank, Phys. *Rev. B: Condens. Matter Mater. Phys*., 1999, **59**, 4973.

[54] A. Mews, U. Banin, A. V. Kadanavich and A. P. Alivisatos, *Ber. Bunsenges. Phys. Chem*., 1997, **101**, 1621.

[55] H. E. Porteanu, E. Lifshitz, M. Pflughoefft, A. Eychmüller and H. Weller, *Phys. Status Solidi B*, 2001, **226**, 219.

[56] A. Ben-Moshe, A. O. Govorov and G. Markovich, Angew. *Chem*., *Int. Ed*., 2013, **52**, 1275.

[57] P.-P. Wang, S.-J. Yu and M. Ouyang, *J. Am. Chem. Soc.*, 2017, **139**, 6070.

[58] A. L. Rogach, S. V. Kershaw, M. G. Burt, M. T. Harrison, A. Kornowski, A. Eychmüller and H. Weller, *Adv. Mater*., 1999, **11**, 552.

[59] T. Rajh, O. I. Mićić and A. J. Nozik, *J. Phys. Chem.*, 1993, **97**, 11999.

[60] N. Gaponik, D. V. Talapin, A. L. Rogach, K. Hoppe, E. V. Shevchenko, A. Kornowski, A. Eychmüller and H. Weller, *J. Phys. Chem.* B, 2002, **106**, 7177.

[61] A. L. Rogach, T. Franzl, T. A. Klar, J. Feldmann, N. Gaponik, L. Lesnyak, A. Shavel, A. Eychmüller, Y. P. Rakovich and J. F. Donegan, *J. Phys. Chem.* C, 2007, **111**, 14628.

[62] V. Lesnyak, N. Gaponik and A. Eychmüller, *Chem. Soc. Rev*., 2013, **42**, 2905.

[63] M. T. Harrison, S. V. Kershaw, M. G. Burt, A. L. Rogach, A. Eychmüller and H. Weller, *J. Mater. Chem.*, 1999, **9**, 2721.

[64] Q. Wen, S. V. Kershaw, S. Kalytchuk, O. Zhovtiuk, C. Reckmeier, M. Vasilevskiy and A. L. Rogach, *ACS Nano*, 2016, **10**, 4301.

[65] M. V. Kovalenko, E. Kaufmann, D. Pachinger, J. Roither, M. Huber, J. Stangl, G. Hesser, F. Scha¨ffler and W. Heiss, *J. Am. Chem. Soc.*, 2006, **128**, 3516.

[66] L. M. Dennis and R. P. Anderson, *J. Am. Chem. Soc.*, 1914, **36**, 882.

[67] S. Richter, M. Steinhart, H. Hofmeister, M. Zacharias, U. Go¨sele, N. Gaponik, A. Eychmüller, A. L. Rogach, J. H. Wendorff, S. L. Schweizer, A. von Rhein and R. B. Wehrspohn, *Appl. Phys. Lett*., 2005, **87**, 142107.

[68] V. Rinnerbauer, K. Hingerl, M. Kovalenko and W. Heiss, *Appl. Phys. Lett*., 2006, **89**, 193114.

[69] A. Al-Otaify, S. V. Kershaw, S. Gupta, A. L. Rogach, G. Allan, C. Delerue and D. J. Binks, *Phys. Chem*. *Chem. Phys*., 2013, **15**, 16864.

[70] M. Chen, H. Yu, S. V. Kershaw, H. Xu, S. Gupta, F. Hetsch, A. L. Rogach and N. Zhao, *Adv. Funct. Mater*., 2014, **24**, 53.

[71] M. Chen, L. Shao, S. V. Kershaw, H. Yui, J. Wang, A. L. Rogach and N. Zhao, *ACS Nano*, 2014, **8**, 8208.

[72] S. Günes, H. Neugebauer, N. Serdar Sariciftci, J. Roither, M. Kovalenko, G. Pillwein and W. Heiss, *Adv. Funct. Mater*., 2006, **16**, 1095.

[73] H. Kim, K. Cho, H. Song, B. Min, J.-S. Lee, G.-T. Kim and S. Kim, *Appl. Phys. Lett.*, 2003, **83**, 4619.

[74] H. Kim, K. Cho, B. Park, J.-H. Kim, J. W. Lee, S. Kim, T. Noh and E. Jang, *Solid State Commun*., 2006, **137**, 315.

[75] P. Olk, B. C. Buchler, V. Sandoghdar, N. Gaponik, A. Eychmüller and A. L. Rogach, *Appl. Phys. Lett.*, 2004, **84**, 4732.

[76] A. L. Rogach, D. S. Koktysh, M. T. Harrison and N. A. Kotov, *Chem. Mater*., 2000, **12**, 1526.

[77] S. I. Shopova, G. Farca, A. T. Rosenberger, W. M. S. Wickramanayake and N. A. Kotov, *Appl. Phys. Lett.*, 2004, **85**, 6101.

[78] D. S. Koktysh, N. Gaponik, M. Reufer, J. Crewett, U. Scherf, A. Eychmüller, J. M. Lupton, A. L. Rogach and J. Feldmann, *ChemPhysChem*, 2004, **5**, 1435.

[79] N. Gaponik, D. V. Talapin, A. L. Rogach, A. Eychmüller and H. Weller, *Nano Lett*., 2002, **2**, 803.

[80] C. Wang, J. Roither, R. Kirschschlager, M. V. Kovalenko, M. Brehm, T. Fromherz, Q. Kan, P. Tan, J. Liu, H. Chen and W. Heiss, *Appl. Phys. Lett.*, 2009, **95**, 053107.

[81] E´. O'Connor, A. O'Riordan, H. Doyle, S. Moynihan, A. Cuddihy and G. Redmond, *Appl. Phys. Lett.*, 2005, **86**, 201114.

[82] J. Roither, M. V. Kovalenko, S. Pichler, T. Schwarzl and W. Heiss, *Appl. Phys. Lett.*, 2005, **86**, 241104.

[83] H. Kim, K. Cho, D.-W. Kim, H.-R. Lee and S. Kim, *Appl. Phys. Lett.*, 2006, **89**, 173107.

[84] M. A. K. Khan and F. Wang, Environ. *Toxicol. Chem*., 2009, **28**, 1567.

[85] J. Gailer, G. N. George, I. J. Pickering, S. Madden, R. G. Prince, E. Y. Yu, B. Denton, H. S. Younis and H. V. Aposhian, *Chem*. *Res*. *Toxicol*., 2000, **13**, 1135.

[86] M. A. K. Khan and F. Wang, *Chem. Res. Toxicol*., 2009, **22**, 1827.

[87] M. Green, S. J. Haigh, E. A. Lewis, L. Sandiford, M. Burkitt- Gray, R. Fleck, G. Vizcay-Barrena, L. Jensen, H. Mirzai, R. J. Curry and L.-*A.* Dailey, *Sci. Rep*., 2016, **6**, 20480.

[88] D. Bouzas-Ramos, M. Mene´ndez-Miranda, J. M. Costa- Ferna´ndez, J. R. Encinar and A. Sanz-Medel, *RSC Adv*., 2016, **6**, 19964.

[89] S. B. Qadri, M. Kuno, C. R. Feng and B. B. Rath, *Appl. Phys. Lett.*, 2003, **83**, 4011.

[90] K. A. Higginson, M. Kuno, J. Bonevich, S. B. Qadri, M. Yousuf and H. Mattoussi, *J. Phys. Chem. B*, 2002, **106**, 9982.

[91] M. Kuno, K. A. Higginson, S. B. Qadri, M. Yousuf, S. H. Lee, B. L. Davis and H. Mattoussi, *J. Phys. Chem. B*, 2003, **107**, 5758.

[92] M. T. Harrison, S. V. Kershaw, A. L. Rogach, A. Kornowski, A. Eychmüller and H. Weller, *Adv. Mater*., 2000, **12**, 123.

[93] W.-H. Zhang, J. Yang and J.-S. Yu, *J. Mater. Chem.*, 2012, **22**, 6383.

[94] D. A. Geier, P. G. King, B. S. Hooker, J. G. Do´rea, J. K. Kern, L. K. Sykes and M. R. Geier, *Clin. Chim. Acta*, 2015, **444**, 212.

[95] S. V. Kershaw, M. G. Burt, M. T. Harrison, A. L. Rogach, H. Weller and A. Eychmüller, *Appl. Phys. Lett.*, 1999, **75**, 1694.

[96] M. T. Harrison, S. V. Kershaw, M. G. Burt, A. Eychmüller, H. Weller and A. L. Rogach, *Mater. Sci. Eng*., *B*, 2000, **69–70**, 355.

[97] A. L. Rogach, M. T. Harrison, S. V. Kershaw, A. Kornowski, M. G. Burt, A. Eychmüller and H. Weller, *Phys. Status Solidi B*, 2001, **224**, 153.

[98] B. Tang, F. Yang, Y. Lin, L. Zhao, J. Ge and L. Cao, *Chem. Mater*., 2007, **19**, 1212.

[99] J. Yang, Y. Zhou, S. Zheng, X. Liu, X. Qiu, Z. Tang, R. Song, Y. He, C. W. Ahn and J. W. Kim, *Chem. Mater*., 2009, **21**, 3177.

[100] H. Sun, H. Zhang, J. Ju, J. Zhang, G. Qian, C. Wang, B. Yang and Z. Y. Wang, *Chem. Mater.*, 2008, **20**, 6764.

[101] Lesnyak, A. Lutich, N. Gaponik,M. Grabolle, A. Plotnikov, U. Resch-Genger and A. Eychmüller, *J. Mater. Chem.*, 2009, **19**, 9147.

[102] M. Grabolle, M. Spieles, V. Lesnyak, N. Gaponik, A. Eychmüller and U. Resch-Genger, *Anal. Chem*., 2009, **81**, 6285.

[103] S. Hatami, C. Wu¨rth, M. Kaiser, S. Leubner, S. Gabriel, L. Bahrig, V. Lesnyak, J. Pauli and N. Gaponik, *Nanoscale*, 2015, **7**, 133.

[104] S. Kalytchuk, M. Adam, O. Tomanec, R. Zborˇil, N. Gaponik and A. L. Rogach, *ACS Photonics*, 2017, **4**, 1459.

[105] S. Gupta, O. Zhovtiuk, A. Vaneski, Y.-C. Lin, W.-C. Chou, S. V. Kershaw and A. L. Rogach, *Part. Part. Syst. Charact*., 2013, **30**, 346.

[106] S. V. Kershaw, N. M. Abdelazim, Y. Zhao, A. S. Susha, O. Zhovtiuk, W. Y. Tang and A. L. Rogach, *Chem. Mater.*, 2017, **29**, 2756.

[107] Qian, C. Dong, J. Peng, X. Qiu, Y. Xu and J. Ren, *J. Phys. Chem.* C, 2007, **111**, 16852.

[108] H. Chen, Y. Wang, J. Xu, J. Ji, J. Zhang, Y. Hu and Y. Gu, *J. Fluoresc*., 2008, **18**, 801.

[109] H. Chen, L. Li, S. Cui, D. Mahounga, J. Zhang and Y. Gu, *J. Fluoresc*., 2011, **21**, 793.

[110] L. Liu, J. Zhang, X. Su and R. P. Mason*, J. Biomed. Nanotechnol*., 2008, **4,** 524.

[111] H. Chen, S. Cui, Z. Tu, J. Ji, J. Zhang and Y. Gu, *Photochem. Photobiol*., 2011, **87**, 72.

[112] J. M. Tsay, M. Pfulghoefft, L. A. Bentolila and S. Weiss, *J. Am. Chem. Soc.*, 2004, **126**, 1926.

[113] N. Y. Morgan, S. English, W. Chen, V. Chernomordik, A. Russo, P. D. Smith and A. Gandjbakhche, *Acad. Radiol*., 2005, **12**, 313.

[114] X. He, L. Gao and N. Ma, *Sci. Rep*., 2013, **3**, 2825.

[115] X. Liu, G. B. Braun, M. Qin, E. Ruoslahti and K. N. Sugahara, *Nat*. *Commun*., 2017, **8**, 343.

[116] M. G. Bawendi, A. R. Kortan, M. L. Steigerwald and L. E. Brus, *J. Chem. Phys*., 1989, **91**, 7282.

[117] E. Lhuillier, S. Keuleyan, H. Liu and P. Guyot-Sionnest, *Chem. Mater.*, 2013, **25**, 1272.

[118] C. B. Murray, PhD thesis, *MIT*, 1995.

[119] M. Green, G. Wakefield and P. J. Dobson, *J. Mater. Chem.*, 2003, **13**, 1076.

[120] L. Huang, R. A. Zingaro, E. A. Meyers and J. H. Reibenspies, *Heteroat. Chem*., 1996, **7**, 57.

[121] H. Liu, J. S. Owen and A. P. Alivisatos, *J. Am. Chem. Soc.*, 2007, **129**, 305.

[122] J. S. Steckel, B. K. H. Yen, D. C. Oertel and M. G. Bawendi, *J. Am. Chem. Soc.*, 2006, **128**, 13032.

[123] D. Yao, Y. Liu, W. Zhao, H. Wei, X. Luo, Z. Wu, C. Dong, H. Zhang and B. Yang, *Nanoscale*, 2013, **5**, 9593.

[124] X. W. Zhang and J. B. Xia, *J. Phys. D: Appl. Phys*., 2006, **39**, 1815.

[125] P. Guyot-Sionnest, 2011, private communication with M. A. Green.

[126] M.-O.M. Piepenbrock, T. Stirner, S. M. Kelly and M. O'Neill, *J. Am. Chem. Soc.*, 2006, **128**, 7087.

[127] Z. A. Peng and X. Peng, *J. Am. Chem. Soc.*, 2001, **123**, 183.

[128] L. S. Li, H. Wang, Y. Liu, S. Lou, Y. Wang and Z. Du, *J. Colloid Interface Sci*., 2007, **308**, 254.

[129] S. Kim, T. Kim, S. H. Im, S. I. Seok, K. W. Kim, S. Kim and S.-W. Kim, *J. Mater. Chem.*, 2011, **21**, 15232.

[130] N. Huo, S. Gupta and G. Konstantatos, *Adv. Mater*., 2017, 29**,** 1606576.

[131] S. Keuleyan, E. Lhuillier and P. Guyot-Sionnest, *J. Am. Chem. Soc.*, 2011, **133**, 16422.

[132] S. Keuleyan, J. Kohler and P. Guyot-Sionnest, *J. Phys. Chem.* C, 2014, **118**, 2749.

[133] E. Lhuillier, S. Keuleyan and P. Guyot-Sionnest, *Nanotechnology*, 2012, **23**, 175705.

[134] P. Geiregat, A. J. Houtepen, L. K. Sagar, I. Infante, F. Zapata, V. Grigel, G. Allan, C. Delerue, D. van Thourhout and Z. Hens, *Nat. Mater*., 2018, **17**, 35.

[135] F. Wise, *Nat*. *Mater*., 2018, 17, 8.

[136] P. K. Santra, A. F. Palmstrom, J. T. Tanskanen, N. Yang and S. F. Bent, *J. Phys. Chem. C*, 2015, **119**, 2996.

[137] D.-K. Ko and C. B. Murray, *ACS Nano*, 2011, **5**, 4810.

[138] M. Chen and P. Guyot-Sionnest, *ACS Nano*, 2017, **11**, 4165.

[139] S. E. Keuleyan, P. Guyot-Sionnest, C. Delerue and G. Allan, *ACS Nano*, 2014, **8**, 8676.

[140] G. Shen, M. Chen and P. Guyot-Sionnest, *J. Phys. Chem. Lett.*, 2017, **8**, 2224.

[141] S. Keuleyan, E. Lhuillier, P. Rekemeyer and P. Guyot- Sionnest*, J. Appl. Phys*., 2011, **110**, 033110.

[142] S. Keuleyan, E. Lhuillier, H. Liu and P. Guyot-Sionnest, *J. Electron. Mater*., 2012, **41**, 2725.

[143] H. Liu, S. Keuleyan and P. Guyot-Sionnest, *J. Phys. Chem. C*, 2012, **116**, 1344.

[144] E. Lhuillier, S. Keuleyan, P. Zolotavin and P. Guyot- Sionnest*, Adv. Mater*., 2013, **25**, 137.

[145] W. Xu, S. Lou, S. Li, H. Wang, H. Shen, J. Z. Niu, Z. Du and L. S. Li, *Colloids Surf.*, *A*, 2009, **341**, 68.

[146] W. Wichiansee, M. N. Nordin, M. Green and R. J. Curry, *J. Mater. Chem.*, 2011, **21**, 7331.

[147] P. Reiss, S. Carayon, J. Bleuse and A. Pron, *Synth. Met.*, 2003, **139**, 649.

[148] K. S. Jeong, Z. Deng, S. Keuleyan, H. Liu and P. Guyot- Sionnest, *J. Phys. Chem. Lett.*, 2014, **5**, 1139.

[149] G. Shen and P. Guyot-Sionnest, *J. Phys. Chem.* C, 2016, **120**, 11744.

[150] B. Yoon, J. Jeong and K. S. Jeong, *J. Phys. Chem.* C, 2016, **120**, 22062.

[151] J. Kim, B. Yoon, J. Kim, Y. Choi, Y.-W. Kwon, S. K. Park and K. S. Jeong, *RSC Adv*., 2017, **7**, 38166.

[152] M. Esmaeili-Zare, M. Salavati-Niasari and A. Sobhani, *Ultrason*. *Sonochem*., 2012, **19**, 1079–1086.

[153] M. Esmaeili-Zare, M. Salavati-Niasari and A. Sobhani, *Micro Nano Lett*., 2012, **7**, 1300–1304.

[154] H. Mirzai, M. N. Nordin, R. J. Curry, J.-S. Bouillard, A. V. Zayats and M. Green, *J. Mater. Chem.* C, 2014, **2**, 2107.

[155] Z. Deng, K. S. Jeong and P. Guyot-Sionnest, *ACS Nano*, 2014, **8**, 11707.

[156] A. Robin, C. Livache, S. Ithurria, E. Lacaze, B. Dubertret and E. Lhuillier, *ACS Appl*. *Mater*. *Interfaces*, 2016, **8**, 27122.

[157] Z. Deng and P. Guyot-Sionnest, *ACS Nano*, 2016, **10**, 2121.

[158] S. Taniguchi, M. Green and T. Lim, *J. Am. Chem. Soc.*, 2011, **133**, 3328.

[159] S. Taniguchi and M. Green, *J. Mater. Chem.*, 2011, **21**, 11592.

[160] A. M. Smith and S. Nie, *J. Am. Chem. Soc.*, 2011, **133**, 24.

[161] A. M. Smith, L. A. Lane and S. Nie, *Nat. Commun*., 2014, **5**, 4506.

[162] S. J. Lim, M. U. Zahid, P. Le, L. Ma, D. Entenberg, A. S. Harney, J. Condeelis and A. M. Smith, *Nat. Commun*., 2015, **6**, 8210.

[163] E. Izqierdo, A. Robin, S. Keuleyan, N. Lequeux, E. Lhuillier and S. Ithurria, *J. Am. Chem. Soc.*, 2016, **138**, 10496.

[164] C. Livache, E. Izqierdo, B. Martinez, M. Dufour, D. Pierucci, S. Keuleyan, H. Cruguel, L. Becerra, J. L. Fave, H. Aubin, A. Ouerghi, E. Lacaze, M. G. Silly, B. Dubertret, S. Ithurria and E. Lhuillier, *Nano Lett.*, 2017, **17**, 4067.

[165] D. Choi, B. Yoon, D.-K. Kim, H. Baik, J.-H. Choi and K. S. Jeong, *Chem. Mater.*, 2017, **29**, 8548.

[166] E. A. Turner, H. Ro¨sner, Y. Huang and J. F. Corrigan, *J. Cluster Sci*., 2007, **18**, 764.

[167] G. Kedarnath, S. Dey, V. K. Jain, G. K. Dey and R. M. Kadam, *J. Nanosci*. *Nanotechnol*., 2008, **6**, 4500.

[168] G. Kedarnath, S. Dey, V. K. Jain and G. K. Dey, *J. Nanosci. Nanotechnol*., 2006, **6**, 1031.

[169] G. Marimuthu, K. Ramalingam, C. Rizzoli and M. Arivanandhan, *J. Nanopart. Res*., 2012, **14**, 710.

[170] S. S. Garje, J. S. Ritch, D. J. Eisler, M. Afzaal, P. O'Brien and T. Chivers, *J. Mater. Chem.*, 2006, **16**, 966.

[171] D. J. Crouch, P. M. Hatton, M. Helliwell, P. O'Brien and J. Raftery, *Dalton Trans*., 2003, 2761.

[172] G. Kedarnath, V. K. Jain, A. Wadawale and G. K. Dey, *Dalton Trans*., 2009, 8378.

[173] N. M. Abdelazim, Q. Zhu, Y. Xiong, Y. Zhu, M. Chen, N. Zhao, S. V. Kershaw and A. L. Rogach, *Chem. Mater.*, 2017, **29**, 7859.

[174] M. Chen, H. Lu, N. M. Abdelazim, Y. Zhu, Z. Wang, W. Ren, S. V. Kershaw, A. L. Rogach and N. Zhao, *ACS Nano*, 2017, **11**, 5614.

[175] A. J. Houtepen, R. Koole, D. Vanmaekelbergh, J. Meeldijk and S. G. Hickey, *J. Am. Chem. Soc.*, 2006, **128**, 6792.

[176] M. M. Moghaddam, M. Baghbanzadeh, A. Keilbach and C. O. Kappe, Nanosc., 2012, **4**, 7435-7442.

[177] C. Bullen, J. Embden, J. Jasieniak, J. E. Cosgriff, R. J. Mulder, E. Rizzardo, M. Gu and C. L. Raston, *Chem. Mater.*, 2010, **22**, 4135-4143.

[178] O. Madelung, U. Rössler and M. Schulz, Eds., in II-VI and I-VII Compounds; Semimagnetic Compounds, *Springer Berlin Heidelberg*, 1999, **41B**, 1-7.

[179] Z. Yang, N. Yang and M.-P. Pileni, *J. Phys. Chem. C*, 2015, **119**, 22249−22260.

[180] M. K. Jana, P. Chithaiah, B. Murali, S. B. Krupanidhi, K. Biswas and C. N. Rao*, J. Chem. C*, 2013, **1**, 6184-6187.

[181] Y. M. Azhniuk, V. M. Dzhagan, A. E. Raevskaya, A. L. Stroyuk, S. Y. Kuchmiy, M. Y. Valakh and D. R. T. Zahn, *J. Phys*.: *Condens*. *Matter*, 2008, **20**, 1-9.

[182] H. Kim, B. Park, K. Cho, J. H. Kim, J. W. Lee, D. W. Kim and S. Kim, *Jap. J. of App*. *Phys*., 2005, **44**, 5703–5706.

[183] B. O. Dabbousi, J. Rodriguez-Viejo, F. V. Mikulec, J. R. Heine, H.Mattoussi, R. Ober, K. F. Jensen and M. G. Bawendi, *J. Phys. Chem.* B, 1997, **101**, 9463-9475.

[184] J. Hao, J. Zhou and C. Zhang, *Chem. Commun*., 2013, **49**, 6346-6348.

[185] S. Sapra, A. L. Rogach and J. Feldmann, *J. Mater. Chem.*, 2006, **16**, 3391–3395.

[186] M. Green, P. Rahmana and D. Smyth-Boyle, *Chem. Commun*., 2007, 574–576.

[187] C. L. Aravinda and W. Freyland, *Chem. Commun*., 2006, 1703.

[188] D. S. Jacobs, L. Bitton, J. Grinblat, I. Felner, Y. Koltypin and A. Gedanken, *Chem. Mater.*, 2006, **18**, 3162..

[189] Y.Wang and H.Yang, *J. Am. Chem. Soc.*, 2005, **127**, 5316.

[190] T. Nakashima and T. Kawai, *Chem. Commun*., 2005, 1643.

[191] H. Lu, G. M. Carroll, N. R. Neale and M. C. Beard, *ACS Nano*, 2019, **13**, 939−953.

[192] A. L. Rogach, M. T. Harrison, S. V. Kershaw, A. Kornowski, M. G. Burt, A. Eychmüller and H. Weller, *Phys. Stat. Sol*. (b), 2001, **224**, 153-158.

[193] A. Jagtap, N. Goubet, C. Livache, A. Chu, B. Martinez, C. Gréboval, J. Qu, E. Dandeu, L. Becerra, N. Witkowski, S. Ithurria, F. Mathevet, M. G. Silly, B. Dubertret and E. Lhuillier, *J. Phys. Chem. C*, 2018, **122**, 14979−14985.

[194] L.S. Li, H. Wang, Y. Liu, S. Lou, Y. Wang and Z. Du, *J. Col. Int. Sci*., 2007, **308**, 254-257.

[195] G. Shen and P. Guyot-Sionnest, *Chem. Mater.*, 2019, **31**, 286-293.

[196] C. T. Dameron, R. N. Reese, R. K. Mehra, A. R. Kortan, P. J. Carroll, M. L. Steigerwald, L. E. Brus and D. R. Winge, *Nature*, 338, 596–597.

[197] S. R. Stürzenbaum, M. Höckner, A. Panneerselvam, J. Levitt, J.-S. Bouillard, S. Taniguchi, L.-A. Dailey, R. A. Khanbeigi, E. V. Rosca, M. Thanou, K. Suhling, A. V. Zayats and M. Green, *Nature Nano*., 2013, **8**, 57-60.

[198] J. Pařízek and I. Ošťádalová, *Experientia*, 1967, **23**, 142-143.

[199] L. A. Cuvin-Aralar and R. W. Furness, *Ecotxicology and Environmental Safety*, 1991, **21**, 348-364.

[200] G. N. George, T. C. MacDonald, M. Korbas, S. P. Singh, G. J. Myers, G. E. Watson, J. L. O'Donoghued and I. J. Pickeringa, *Metallomics*, 2011, **3**, 1232-1237.

[201] P.-S. Ng, H. Li, K. Matsumoto, S. Yamazaki, T. Kogure, T. Tagai and H. Nagasawa, *Proc*. *Japan Acad*., *Ser*. *B*, 2001, **77**, 178-183.

[202] D. H. McNear Jr., S. E. Afton and J. A. Caruso, *Metallomics*, 2012, **4**, 267-276.

[203] S. E. Afton and J. A. Caruso, *J. Anal. At. Spectrom*., 2009, **24**, 759-766.

[204] S. F. Wuister, C. de Mello Donegá and A. Meijerink, *J. Phys. Chem. B*, 2004, 108, 17393–17397.

[205] N. C. Greenham, X. Peng and A. P. Alivisatos, *Phys. Rev. B*., 1996, **54**, 17628–17637.

[206] D.-Y. Chao, Y. Chen, J. Chen, S. Shi, Z. Chen, C. Wang, J. M. Danku, F.-J. Zhao and D. E. Salt, *PLOS Biology*, 2014, **12**, e1002009.

[207] Y. Anan, M. Yoshida, S. Hasegawa, R. Katai, M. Tokumoto, L Ouerdane, R. Łobińskibc and Y. Ogra, *Metallomics*, 2013, **5**, 1215–1224.

[208] L. S. Lichtmann and J. D. Parson, US patent No. **4**, 1989, 828, 938.

[209] J. G. Brennan, T. Siegrist, P. J. Carroll, S. M. Stuczynski, P. Reynders, L. E. Brus and M. L. Steigerwald, *Chem. Mater.*, 1990, **2**, 403–409.

[210] D. F. Shriver, M. A. Drezden, *The manipulation of air sensitive compounds, 2nd ed., Wiley-Interscience*, *New York*, 1986.

[211] P. D. Nellist and S. J. Pennycook, *Adv. in Ima. and Elec. Phy*., 2000, **113**, 147-203.

[212] K. E. MacArthur, *Johnson Matthey Technol. Rev.*, 2016, **60**, 117–131.

[213] E. Lhuillier, A. Robin, S. Ithurria, H. Aubin and B. Dubertret, *Nano Lett*., 2014, **14**, 2715–2719.

[214] Z.-Y. Chen, H. N. Abdelhamid and H.-F. Wu, *Rapid Commun. Mass Spectrom*., 2016, **30**, 1403–1412.

[215] X. Han, J. Leia, K. Chena, Q. Lia, H. Haoa, T. Zhoua, F. L. Jiangb, M. Lia and Y. Liub, *Eco. Env. Safe*., 2019, **174**, 467-474.

[216] A. Sadaf, B. Zeshan, Z. Wang, R. Zhang, S. Xu, C. Wang, and Y. Cui, *J. Nano*. *Nanotech*., 2012, **12**, 8287–8292.

[217] F. S. Soares‡, T. Fernandes, A. L. D.-da-Silva and T. Trindade, *Proc. R. Soc*., 2019, **475**, 1-33.